EPFL

Thèse n° 9881

Delayed Hydride Cracking in Irradiated and Unirradiated Zircaloy-2 Cladding

Aaron William COLLDEWEIH

École
polytechnique
fédérale
de Lausanne

2022

Acknowledgments

Over the last four years, I have gained many skills and scientific knowledge. However, above the scientific knowledge, the most impactful thing that I gained was the experience of a supportive, patient, and encouraging supervisor. Dr. Johannes Bertsch has been a great role model in how he mentors students and how he approaches research. The assets I have gained from Dr. Bertsch are invaluable and I am very thankful. I am also very thankful for the work flexibility and understanding that he has allowed.

I am also thankful for Dr. Manuel Pouchon for the scientific discussions about my project and the approachability. I am grateful for the many opportunities we had at the microscope to conduct analysis and fruitful conversations. I have also been personally inspired for his determination to commute to work by bike every day, regardless of time of day or weather.

I am thankful to have been able work with and gotten to know Dr. Pavel Trtik. We have had many interesting conversations not only about science, but also about politics. I am thankful to have experienced his detailed approach to neutron imaging and his support of all the imaging analysis. Additionally, I am grateful for the support during the several beam times regardless of the time of day. Without his guidance, I would have never been able to explore radiography to the same level.

In the last two years of the project, I jumped spontaneously into a new topic, µXRD. Without the support from Dr. Malgorzata Makowska, the experiments would not have come to fruition. I am thankful for her advocating to get in-house beam time, which supported the majority of the XRD experiments performed in this thesis. I am also grateful for the significant help supervising my first student. I have learned a wide 'spectrum' of things from her ranging from science to proposal writing.

Abstract

Zirconium alloys used in the nuclear industry are exposed to extreme conditions undergoing high levels of irradiation damage and corrosion. Zircaloy-2 is used as nuclear fuel cladding in boiling water reactors and for the encapsulation of the spallation target in the neutron source SINQ at the Paul Scherrer Institute. As a result of oxidation, hydrogen is produced and partially taken up into the zirconium matrix. As the hydrogen reaches the solubility limit, it precipitates in the form of a zirconium hydride. A number of deleterious effects of hydrides have been extensively studied, including the embrittlement of the material and a unique cracking phenomenon, namely delayed hydride cracking (DHC). DHC occurs as hydrogen in solid solution diffuses towards locations of higher tensile stress, where it subsequently precipitates as the local solvus limit is reached. Once the hydride grows to a critical size, it fractures, which can continue to propagate in repeated steps by the same mechanism.

Several studies have been performed in order to understand properties of DHC based on parameters like, alloy type, cracking temperature, hydrogen content, and cracking direction. The most important mechanical properties include the fracture toughness and cracking velocity, which governs the material failure conditions. Crystallographic properties have been investigated in order to understand how complex hydride precipitation develops within the context of DHC conditions.

In this project, radial DHC is explored in irradiated and unirradiated thin-walled Zircaloy-2 nuclear fuel cladding with and without an inner liner, in addition to spallation target rod material. A unique three-point bending test, applicable also for irradiated samples in the hotlab, was developed to induce a consistent radially propagating outside-in crack. Results have provided insight into the effects of the inner liner on cracking velocity, showing correlations with the hydrogen depletion. The combined DHC and creep mechanisms, which cannot be decoupled, is coined as 'creep-delayed hydride cracking'. As the initiating conditions for DHC

are of great technical importance, the threshold stress intensity factor has been investigated, under ideal DHC conditions, where a minimum value occurs around 6 MPa√m.

Quantitative analysis of the hydrogen distribution around the tip of an arrested DHC crack tip has been performed with neutron radiography at the SINQ. Trends show that the hydrogen concentration around the crack tip increases with temperature resulting likely from the larger hydrogen diffusion, and that the liner reduces the hydrogen available for DHC. Crystallographic analysis has provided insight on the hydride phases responsible for DHC with synchrotron micro X-ray diffraction, performed at the Swiss Light Source at PSI. The results directly suggest that the γ-hydride is a stable phase precipitated at low temperatures. Testing of irradiated material provided insight into the crack initiation of DHC as a result of the strongly irregular outer surface generated from the oxidation. The propagation pattern is highly irregular compared to the unirradiated material due to the embrittled nature of the cladding from irradiation damage.

Keywords

Delayed hydride cracking (DHC), Zircaloy-2, zirconium hydride, three-point bending, crack velocity, threshold stress intensity factor, neutron radiography, X-ray diffraction.

Zusammenfassung

Die in der Nuklearindustrie verwendeten Zirkoniumlegierungen sind extremen Einflüssen ausgesetzt, welche zu einem hohen Mass an Bestrahlungs- und Korrosionschäden führen. Zircaloy-2 wird als Hüllrohrmaterial in Siedewasserreaktoren und für die Verkapselung des Spallationstargets in der Neutronenquelle SINQ des Paul Scherrer Instituts eingesetzt. Durch die Korrosion wird Wasserstoff erzeugt und teilweise in die Zirkoniummatrix aufgenommen. Wenn dieser die Löslichkeitsgrenze überschreitet, präzipitiert er als Zirkoniumhydrid. Die Auswirkungen von Hydriden sind ausführlich untersucht, wie die Versprödung des Materials und ein spezielles Rissbildungsphänomen, nämlich die verzögerte Hydridrissbildung (Delayed Hydride Cracking, DHC). DHC tritt auf, wenn gelöster Wasserstoff hin zu Stellen mit höherer Zugspannung, z.B. an feine Risse diffundiert, und dort Hydride bildet, wenn die lokale Löslichkeitsgrenze überschritten ist. Sobald ein Hydrid eine kritische Grösse erreicht hat, bricht dieses, und ein Riss wächst durch den sich wiederholenden Mechanismus .

Es existieren mehrere Studien, um die Eigenschaften von DHC basierend auf Parametern wie Legierung, Temperatur, Wasserstoffgehalt und Rissrichtung zu verstehen. Zu den wichtigsten mechanischen Eigenschaften gehören die Bruchzähigkeit und die Rissgeschwindigkeit, die das Materialversagen bestimmen. Kristallographische Eigenschaften wurden untersucht, um die komplexe Hydridbildung unter DHC Bedingungen zu klären.

In diesem Projekt wird DHC untersucht in bestrahlten und unbestrahlten dünnwandigen Zircaloy-2-Hüllrohren, mit und ohne sogenanntem Liner an der Hüllrohr-Innenseite, sowie anhand von Verkapselungs-Stäben des SINQ Spallationstargets. Ein spezieller Dreipunkt-Biegetest wurde entwickelt, der auch für bestrahlte Proben im Hotlabor genutzt wird, um konsistent einen von aussen nach innen radial wachsenden Riss zu induzieren. Der Liner bewirkt eine Reduzierung der Wasserstoffkonzentration rund um die Rissspitze und eine Verlangsamung des Risses. Die bei höheren Temperaturen auftretende Kombination von DHC und Kriechen wird als „Kriech-DHC" bezeichnet. Da die Minimalbedingungen von DHC

von technischer Relevanz sind, wurde der Spannungsintensitätsfaktor unter idealen DHC-Voraussetzungen untersucht; sein Wert beträgt etwa 6 MPa√m.

Quantitative Analysen der Wasserstoffverteilung rund um die Rissspitzen nach DHC wurden mit Hilfe von Neutronenradiographie an der Spallations-Neutronen Quelle SINQ durchgeführt. Die Neutronenradiographie zeigt unter anderem, inwieweit der Liner den für DHC verfügbaren Wasserstoff reduziert. Kristallographische Analysen an der Swiss Light Source SLS mit Röntgenbeugung legen nahe, dass das γ-Hydrid ebenfalls auftritt und eine bei niedrigen Temperaturen stabile Phase ist. Die Untersuchung von bestrahltem Material zeigt die DHC-Rissinitiierung als Folge der durch die Oxidation erzeugten stark fragmentierten äußeren Oberfläche. Das Ausbreitungsmuster ist im Vergleich zum unbestrahlten Material aufgrund der bestrahlungsinduzierten Versprödung sehr unregelmäßig.

Stichwörter

verzögerte Hydridrissbildung (DHC), Zircaloy-2, Zirkoniumhydrid, Rissgeschwindigkeit, Spannungsintensitätsfaktor, Dreipunkt-Biegetest, Neutronenradiographie, synchrotronbasierte Röntgenbeugung,

Contents

List of abbreviations

BSE	Backscattered electron
BWR	Boiling water reactor
BB	Black bodies
CT	Compact tension
CTO	Crack tip opening
DC	Dark current
DCPD	Direct current potential drop
DFM	Diffusion first model
DHC	Delayed hydride cracking
DHCV	Delayed hydride cracking velocity
EELS	Electron energy loss spectroscopy
EPFM	Elastic plastic fracture mechanics
FCC	face-centered cubic
FCT	face-centered tetragonal
FEM	Finite element modeling
FIB	Focused ion beam
HVE	Hot vacuum extraction
HWR	Heavy water reactor

KKL	Kernkraftwerk Leibstadt (Leibstadt Nuclear Power Plant)
HCP	hexagonal close-packed
LEFM	Linear elastic fracture mechanics
LOCA	Loss of coolant accident
LOM	Light optical microscope
LWR	Light water reactor
NPP	Nuclear power plant
OB	Open beam
PCI	Pellet-cladding nteraction
PI	Projection image
PIE	Post-irradiation examination
PFM	Precipitation first model
PLT	Pin-loading tension
RIA	Reactivity induced accident
ROI	Region of interest
SE	Secondary electron
SEM	Scanning electron microscope
SENT	Single-edge notch tension
SINQ	Swiss spallation neutron source

SLS	Swiss Light Source
SNF	Spent nuclear fuel
SPP	Second phase particle
TEM	Transmission electron microscope
TSSD	terminal solid solubility limit of dissolution
TSSP	terminal solid solubility limit of precipitation
XRD	X-ray diffraction

1. Introduction

1.1. Background

The electricity production from nuclear power in 2020 totaled 5.6 TWh, or nearly 10% of all electricity produced in the world [1]. Of the commercial nuclear power plants (NPP), about 90% of the reactors consist of light and heavy water reactors (LWR and HWR) [2]. The basic process of these reactors is to create heat, which is used to generate steam that turns a steam turbine connected to an electrical generator [2]. The heat is generated within the core of the reactor where either enriched or natural uranium fuel undergoes fission reactions. The heat from fission is then removed from the uranium fuel via the heat transfer through the fuel cladding and then the fuel coolant and moderator medium, water.
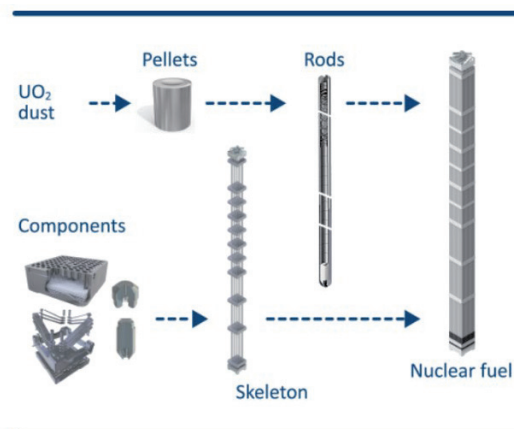
Figure 1.1: A schematic of the components of a fuel assembly, including the fuel pellet, rod, and components. Taken from reference [3]**.**

From Figure 1.1 it can be seen that the uranium fuel is comprised of hundreds of pellets that are sealed inside the fuel cladding. The cladding and pellets comprise the fuel rod, several of which constitute a fuel assembly. Each fuel assembly is used for a number of reactor cycles, in total generally lasting 3-7 years (depending on operation conditions) to subsequently generate electricity [4]. The total lifetime of each fuel assembly is dependent on a number of

variables including operational strategies (economics), and regulatory limitations such as fuel burn-up, cladding oxidation, and subsequent hydrogen uptake [5], [6]. Specifically, the oxidation and hydrogen uptake of the cladding can lead to deleterious effects on the mechanical properties such as embrittlement. After the service lifetime of the nuclear fuel is complete, the fuel cycle continues for a number of years in the spent fuel cooling pool and then intermediate storage [7]. In some countries, the choice to recycle the fuel after it has been discharged from the reactor is selected, while others, such as Switzerland, have chosen to store the fuel in a long-term deep geological repository [8]. Therefore, it can be quickly foreseen that the handling and manipulation of the spent nuclear fuel (SNF) will be considerable during the various transportation and storage stages.

Once more, considering the effects of the hydrogen uptake during the service lifetime and the numerous scenario during the transportation and long-term storage of the fuel, the detailed understanding of the cladding mechanical properties becomes of high importance to ensure the integrity of fuel cladding until the end of its life cycle and beyond.

1.2.   Motivation and goals of the thesis

In the context of transportation and storage of SNF, literature has shown the complicated and numerous mechanical effects of hydrogen on nuclear fuel cladding [9], [10]. Of the vast amount of research performed to investigate effects that hydrogen has on the cladding, delayed hydride cracking (DHC) has been a backdrop and motivation for many of the studies. DHC is a subcritical crack growth mechanism, in which hydrogen in solid solution migrates towards locations of higher tensile stress. As the solvus limit is exceeded, hydrogen will precipitate in the form of hydrides that will fracture upon growing to a critical size [11]. This process will happen in repeated steps by the same mechanism. In the context of transportation and storage of SNF, where internal fuel rod gas pressures exist from fission gases, and possible external stresses from handling incidents can occur, DHC could lead to the catastrophic failure of the fuel rod releasing highly radioactive fission products into the storage

or transport container. Early research conducted on DHC was motivated by the cracking of the pressure tubes in the CANDU reactor in Pickering, Ontario [12]. While extensive research has been conducted on DHC since the Pickering experience, most studies have been conducted on pressure tube material and cracking in an axial direction with respect to tube material [13], [14].

In the frame of this PhD, the motivation is to expand the study of DHC in the context of SNF. The project aims to investigate the validity of assumptions of previous tests considering the geometrical and crystallographic texture differences in pressure tube material and axial cracking, respectively, compared to SNF. Additionally, the effects of irradiation damage on DHC has been studied little compared to unirradiated material. For these reasons, this project focuses on unirradiated and irradiated Zircaloy-2 cladding materials. The irradiated material was taken from target rods from the Swiss spallation neutron source (SINQ) and nuclear fuel cladding from the boiling water reactor (BWR) type NPP Leibstadt (KKL). Given the challenges of testing radioactive material, the Paul Scherrer Institute offered large scale facilities such as the Hot Laboratory, SINQ, and the Swiss Light Source (SLS) to make testing possible.

The main goals of the thesis are summarized as follows:

- Design a novel method for testing DHC in nuclear fuel cladding, which induces a crack in the radial outside-in direction and oriented axially with the fuel rod. The test should be practical enough for testing irradiated cladding material.

- Investigate the mechanical properties of DHC at various temperatures and hydrogen concentrations.

- Investigate the possible effects of the soft hydrogen-absorbing inner liner of Zircaloy-2 type claddings used in BWR's on DHC propagation.

- Observe hydrogen diffusion and precipitation from DHC using high-resolution neutron imaging.

- Explore the hydride phases responsible for DHC at different temperatures using synchrotron based micro-XRD techniques.

The thesis will draw conclusions on the improved understanding of DHC mechanisms and its behavior in nuclear fuel cladding and the impact it has on transportation and dry-storage of SNF. The motivation for the specific points above are given at the beginning of the respective experimental chapter.

2. Literature review

In this chapter, an overview of research and knowledge relevant to this project is presented. First, an overview of zirconium alloys is presented and then followed by the changes it undergoes during in-reactor service. Next, the effects of hydrogen in zirconium alloys are described, specifically delayed hydride cracking (DHC). Current research and tests employed to study DHC are presented with their advantages and disadvantages. Lastly, an overview of relevant fracture mechanics and standards is given with the thesis objectives.

2.1. Zirconium alloys for nuclear applications

Zirconium alloys provide the following functions for nuclear application in the form of fuel cladding [15]:

- The first barrier of defense sealing off fission products from the coolant

- Acts a structural support for the reactor core and fuel elements

- Provides a surface for heat exchange from fuel to coolant

Zirconium alloys are chosen for their sufficient corrosion resistance, strength properties, thermal conductivity, and low thermal neutron capture.

2.1.1. Alloying elements and cladding evolution

The alloying elements that make up a zirconium alloy include tin, iron, chromium, nickel and niobium. When zirconium alloys were being developed in the 1950's and 60's, tin was the first alloying element utilized to create Zircaloy-1 for corrosion resistance and mechanical stability. Tin was later reduced to incorporate other elements to further increase corrosion resistance. Iron was added for enhancement of corrosion resistance as well, but kept to a minimum in order to maintain fabrication limits and cladding neutron transparency. Chromium was also added for corrosion resistance but kept to a minimum so that the alloy would not become too

hard. Nickel also increased the corrosion resistance especially in high temperature steam such as in a BWR. The typical cladding used in a BWR is therefore Zircaloy-2 for its resistance to corrosion in steam environments. However, the nickel also enhances the hydrogen uptake of the alloy, which is an undesired effect. Zircaloy-4 was later developed, which is a "Ni-free Zircaloy-2", typically used in PWRs because it does not have the requirements of a steam environment and has better resistance to hydrogen pick-up. In order to compensate for the lack of nickel in Zircaloy-4, iron is added. In addition, there are specific heat treatments of the alloys which have been shown to slightly enhance the corrosion resistance in water, while significantly enhancing its resistance in high temperature steam [15], [16]. Metallurgical techniques also have a large effect on the corrosion resistance. The reduction of second phase particle (SPP) size, specific to the given alloy, creates a more homogenous distribution of the SPPs. The homogeneity aids in the resistance to nodular corrosion caused by local depletion of alloying elements [6].

As stated more specifically above, zirconium alloys have been developed to resist chemical and subsequent mechanical degradation in service. Such resistance to mechanical degradation incudes the alloy texture leading to a circumferential preference, rather than radial, of brittle hydride phases. The lifetime of nuclear fuel is limited by the amount of cladding degradation sustained during operation. Naturally, fuel cladding development has been pushed in order to improve the economics and safety of the nuclear fuel. In the next sections some of the leading causes for cladding degradation will be described in detail, including irradiation damage, waterside corrosion, and hydrogen uptake. Of these processes, waterside corrosion and hydrogen uptake are the leading degradation factors which limit the fuel lifetime [6], [15], [17].

2.2. Irradiation damage

Through neutron irradiation from a given source, the zirconium alloy cladding undergoes irradiation damage that causes a number of defects [18]–[21]. The result of such irradiation damage is a change in the crystal structure, where defects are introduced. Subsequently, there is a change in mechanical properties that leads to hardening and an increase in yield stress.

Irradiation damage of the material studied in this project was produced through nuclear reactor or spallation target exposure. The two reactions are generated in a commercial nuclear reactor and a neutron spallation source, which are described in the following points.

- Fission: The main objective of commercial reactors is to produce electricity through nuclear fission. In a commercial reactor, the typical fission reaction, which Uranium-235 undergoes, is described in Equation 2.1, where the neutron capture results in the fission leading to roughly 200 MeV being released. The majority of the energy appears as kinetic energy in the two to three daughter nuclei (largely stopped within the fuel pellet), DN, some number, k, of prompt neutrons (fast neutrons cause the majority of irradiation damage), n, (on average 2.5) and prompt gamma rays [21], [22].

Equation 2.1

$$^{235}_{92}U + n \ \rightarrow \ ^{236}_{92}U \ \rightarrow {}^{A}_{Z}DN + \ {}^{A}_{Z}DN' + (k)^{1}_{0}n$$
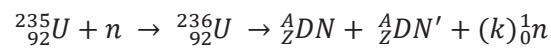
Through the fission reaction, the high-energy neutrons (~2 MeV) interact with the fuel cladding causing damage in the form of point-defects and defect-clusters that eventually form dislocation loops and microstructural change.

- Spallation: The spallation reaction occurs when a target is bombarded with high-energy particles, such as protons, causing the target to disintegrate via inelastic nuclear reactions. The particles emitted include, protons, neutrons, alpha-particles, and other spallation products [23]. Typically, high-Z materials are chosen as the target material. The objective of a spallation target is to create a source of neutrons. The general spallation reaction is seen in Equation 2.2:

Equation 2.2

$$p + ST \rightarrow SF_1 + SF_2 + \cdots + SF_m + (k)n$$

where p is the incident proton, ST is the spallation target, SF are the m spallation fragments, and the number of k neutrons produced from the type of reaction.

In the SINQ, lead targets are encapsulated with Zircaloy-2 cladding, which also experiences the high-energy proton beam (~570 MeV). The resulting irradiation damage in the target rods of the spallation source is similar to that of the nuclear fuel rods described above, but occurs at a much faster rate due to the significantly higher flux and energy level of protons and spallation products in addition to neutron irradiation.

2.3. Corrosion

As mentioned above, zirconium alloys are also degraded through oxidation. It is known that pure zirconium readily oxidizes and forms a 2-5 nm thick oxide layer at room temperature [6]. However, the corrosion of fuel claddings takes place in a much more corrosive environment. During the in-reactor lifetime, the cladding experiences high temperatures in a corrosive environment, i.e. in light (power plant) and heavy water (SINQ). The general equation for zirconium corrosion in water is as follows:

Equation 2.3

$$Zr + 2H_2O \rightarrow ZrO_2 + 2H_2$$
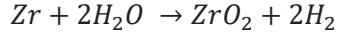
Corrosion leads to a number of effects, like a reduction in heat transfer and reduction of the metal cladding wall thickness itself. When oxide spalling (breakaway) takes place, large gradients in heat transfer coefficients can occur leading to hot and cold spots and to an uneven oxide growth in a non-protective manner [24]. As the oxide layer grows inward, the hydrogen produced from the dissociation of water can either go into the water as gas or recombine with oxygen, or diffuse into the cladding resulting in "hydrogen uptake". The following subchapter discusses further the various mechanisms of hydrogen uptake.

2.4. Hydrogen uptake and diffusion

It has been observed that hydrogen uptake in as fabricated zirconium alloys occurs through four processes; absorption through the normal corrosion process, direct reaction with gaseous hydrogen, diffusion of hydrogen through a metallic bond with a dissimilar metal, and cathodic polarization of zirconium in a electrolytic environment [6]. Of these processes, the most prominent path of hydrogen uptake in reactor conditions is through the waterside corrosion [17]. Once the zirconium has been oxidized, as shown in Equation 2.3, a fraction of the hydrogen can be taken up into the zirconium matrix, and is defined as the hydrogen pick-up fraction, f_H (Equation 2.4)

Equation 2.4

$$f_H = \frac{\Delta_0^t H_{absorbed}}{\Delta_0^t H_{generated}}$$

where $\Delta_0^t H_{absorbed}$ and $\Delta_0^t H_{generated}$ are the amount of hydrogen absorbed and generated by the cladding from the onset of corrosion respectively. The hydrogen pick-up fraction has been

extensively studied. The mechanisms vary between different zirconium alloys, some of which include:

- – Transport mechanisms through the water-side oxide layer [5], [15], [25]
- – The driving force for such transport including operational parameters

Once the hydrogen reaches the zirconium matrix it can diffuse throughout the matter according to various driving forces. The flux of hydrogen can be defined though the combination of various effects including, Fick's law of diffusion, the Soret effect, and stress [26]–[29].

Equation 2.5

$$J_{diffusion} = J_{Fick} + J_{Soret} + J_{Stress} = -D_H \nabla C_{ss} - \frac{D_H C_{ss} Q^*}{RT^2} \nabla T + \frac{D_H C_{ss} V}{RT} \nabla \sigma_H$$

where D_H is the hydrogen diffusion coefficient [9], [30], C_{ss} is the concentration of hydrogen in solid solution in the matrix of zirconium, Q^* represents the heat of transport, V_H is the partial molar volume of hydrogen, σ_H is the hydrostatic stress of the system, R is the ideal gas constant, and T is the temperature.

In the case that hydrogen diffusion leads to a location where the local solubility limit is exceeded, zirconium hydrides can precipitate [31]. The next subchapter discusses zirconium hydrides and their precipitation.

2.5. Zirconium hydrides

As the local limit for solid solubility of hydrogen is reached, various phases of zirconium hydrides can precipitate. The limits at which hydrogen precipitates and dissolves are known as the terminal solid solubility for precipitation and dissolution, (TSSp and TSSd). The studies that are summarized in Figure 2.1 describe results of experiments to determine TSSp and TSSd using differential scanning calorimetry and synchrotron radiation diffraction [9].
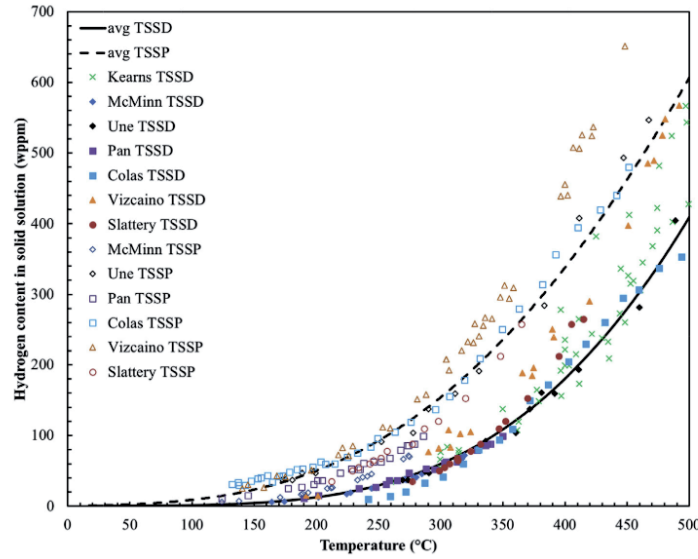
Figure 2.1: A summary of the various data showing TSSD and TSSP curves. From reference [9]**.**

As the hydride formation leads to the embrittlement of claddings, there has been extensive research on understanding the mechanisms of hydride precipitation and mechanical properties [32]–[35]. Hydride embrittlement of cladding generally acts on a macroscopic scale, however, local cladding degradation caused by hydrides can occur though mechanisms known as delayed hydride cracking, (DHC) [36]–[38]. The understanding of precipitation is one way to help ensure the mechanical integrity of the zirconium alloy. In the next section, the hydride phases are discussed in their context.

2.5.1. Zirconium hydride phases and microstructure

Of the various hydride phases that can occur in a stoichiometric range from $ZrH_{0.25-2}$ [39]–[42], the fcc δ- $ZrH_{1.6-1.7}$, and fct γ-ZrH phases have been reported [39], [43]–[50]. Considering past and present literature, it seems that the stability of the γ phase is still unclear. Recent studies have shown a strong temperature dependence of the γ/δ phase fraction within the hydrides of a DHC crack flank [44], as well as cooling/quench rate [43]. Figure 2.2 shows the zirconium and hydrogen phase diagram and at what temperatures the different hydride phases can be formed. Barrow et al. have shown the δ-hydride 'core' precipitates through the growth of the

26

outer γ-hydride 'tip', as the γ-hydride nucleates first due to its lower accommodation energy [45]. In Table 2.1, the phases of hydrides and some crystallographic properties are given. While literature has reported on the ζ- and ε-hydride phases, the context of formation is still unclear [51].
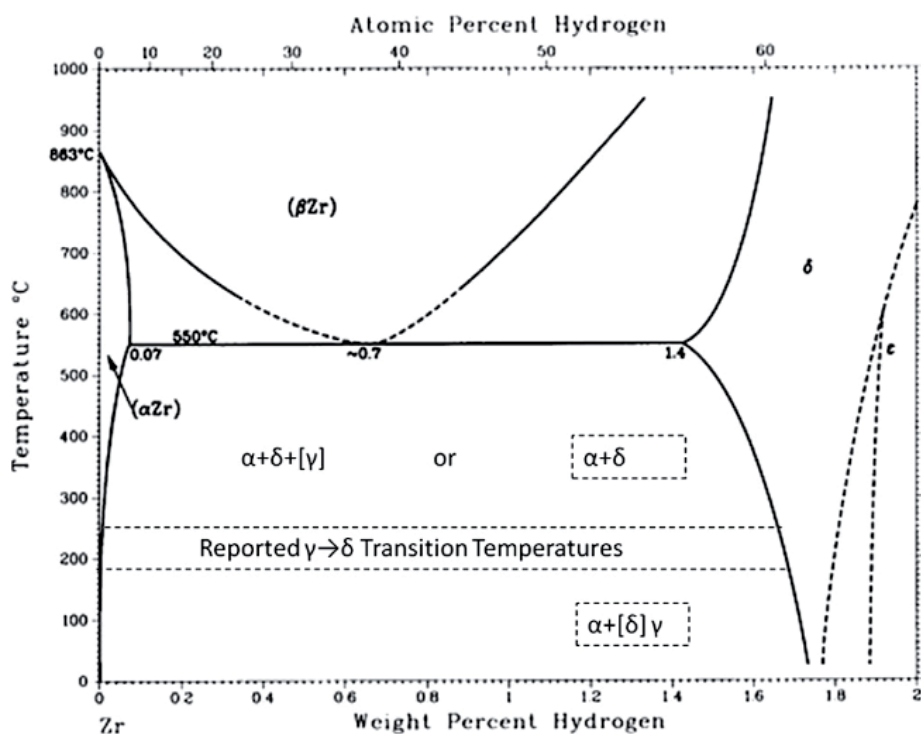
Figure 2.2: Phase diagram of zirconium and hydrogen. Adapted from ref [43].

Table 2.1: Different hydride phases and crystallographic information. [41], [45]

Phase	Powder Diffraction Nos.	Crystal Structure	Vol. expn. in α-Zr	Composition	a_0 (nm)	c_0 (nm)
ζ-hydrides	[41]	hcp	-	$ZrH_{0.25-0.5}$	0.33	1.029
γ-Hydride	00-034-0690	fct (ordered)	12.3%	ZrH	0.4596	0.4969
δ-Hydride	00-034-0649	fcc	17.2%	$ZrH_{1.6-1.7}$	0.4781	
ε-Hydride	00-017-0314	fct	-	ZrH_2	0.3520	0.4450
α-Zr	00-005-0665	hcp	-	-	0.3232	0.5147

27

Because the large temperature range which can occur for fuel claddings encompasses the precipitation temperatures for both δ and γ phases [52], and because the mechanical properties of the hydrides can change with phase and stoichiometry [11], [12], it is important to identify and understand hydride precipitation kinetics at different temperatures. The knowledge of their formation will also help to understand the mechanisms of DHC, which are discussed in the following section.

2.6. Delayed hydride cracking

The phenomenon of DHC was reported as early as the 1970s on CANDU Zr-2.5%wt Nb pressure tubes [53]. DHC can be simply described as a subcritical crack growth phenomenon, in which hydrogen in solid solution diffuses towards a location of higher tensile stress where it precipitates in the form of a hydride as the solvus limit is exceeded. When the hydride reaches a critical size, it fractures under the tensile stress, leading to crack propagation in repeated steps by the same mechanism [11], [52]. A diagram of the steps described can be seen in Figure 2.3.
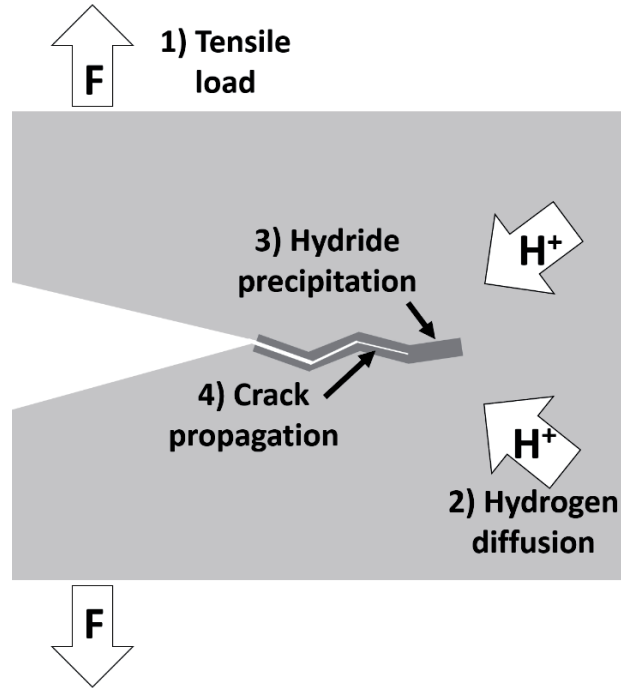
Figure 2.3: A general model of the steps that occurs during DHC.

Today's two models of the DHC process are known as the diffusion first model (DFM) [54] and precipitation first model (PFM) [55]. These models are formed by the leading authors, R. Dutton and M.P. Puls, and Y.S. Kim. Dutton and Puls have formed the DFM while Kim has formed the PFM. Both models attempt to describe the driving force of hydrogen diffusion throughout the matrix during DHC. However, in these models, the theories for the driving force of hydrogen diffusion are not complimentary, but rather, opposing. These two models will be explained in more detail in the following sections. Following a description of the models, a summary of DHC experiments performed is given.

2.6.1.   Diffusion first model

The DFM is formulated around the hypothesis that hydrostatic stress, p, which varies with position, r, changes the chemical potential, μ_H^D, of hydrogen diffusion in the zirconium lattice [11], [56]. In Equation 2.6, the effect of stress is simply written.

Equation 2.6

$$\mu_H^D(r,p) = \mu_H^0 + RTlnc_H^D(r,p) - p(r) * \bar{V}_H$$

where μ_H^0 is the initial chemical potential, R and T, are the ideal gas constant and temperature, respectively, and $\bar{V}_H$, is the molar volume of hydrogen in the alpha phase. This equation simply states that the chemical potential is higher for locations containing diffusible hydrogen compared to the hydrogen-free alpha lattice, and decreases as hydrostatic stress increases positively. Because of the stress-induced chemical potential gradient, hydrogen diffuses towards locations of lower chemical potential (i.e. regions of tensile stress), where it precipitates subsequent to exceeding the local solvus limit. Therefore, the DFM concludes that the effect of the stress-induced chemical potential gradient is the primary driving force for hydrogen diffusion during DHC.

Simpson et al. has suggested an improvement to the original DFM model where hydrogen will dissolve from hydrides located in low stress regions and diffuse to regions of high stress where they reprecipitate [57].

2.6.2. Precipitation first model

The PFM described by Kim shows that the concentration gradient is the primary driving force for hydrogen diffusion [58]–[64]. Unlike the DFM, the PFM is not described with a mathematical formulation or analytical or numerical derivation [56]. It is shown that the solubility of hydrogen decreases because of increased tensile stress. Therefore, increased hydride precipitation is expected near the crack tip where the stress is highest. A concentration gradient is then caused through the precipitation of hydrides causing a depletion in the local solute hydrogen. Thus, hydrogen continues to diffuse towards lower concentration regions according to Fick's law. Kim, the author of the PFM, suggests that the DFM cannot explain why, (i) the delayed hydride cracking velocity (DHCV) becomes constant independently of the stress intensity factor (SIF) (K_{IH}), (ii) why the DHCV is affected by the direction of approach to test

temperature, (iii) and the effect of hydride size on the DHCV. Literature has shown that both authors of the two models have extensively commented on the opposing model [56], [58], [65].

2.6.3. Current DHC experiments

Many different tests have been employed to test the fracture mechanics of DHC. Some of these tests include the use of compact tension, pin-loading tension, and ring-tension fixtures [60], [66], [67]. Various testing parameters have been reported in the context of loading and temperature control, some of which can be seen in Figure 2.4. The loading parameters vary from constant force, constant stress intensity factor K_I, up-loading, and down-loading. The objective of the constant load and K_I tests were to test the DHC velocity, DHCV, while the up- and down-loading aimed to test the DHC threshold stress intensity factor (K_{IH}).
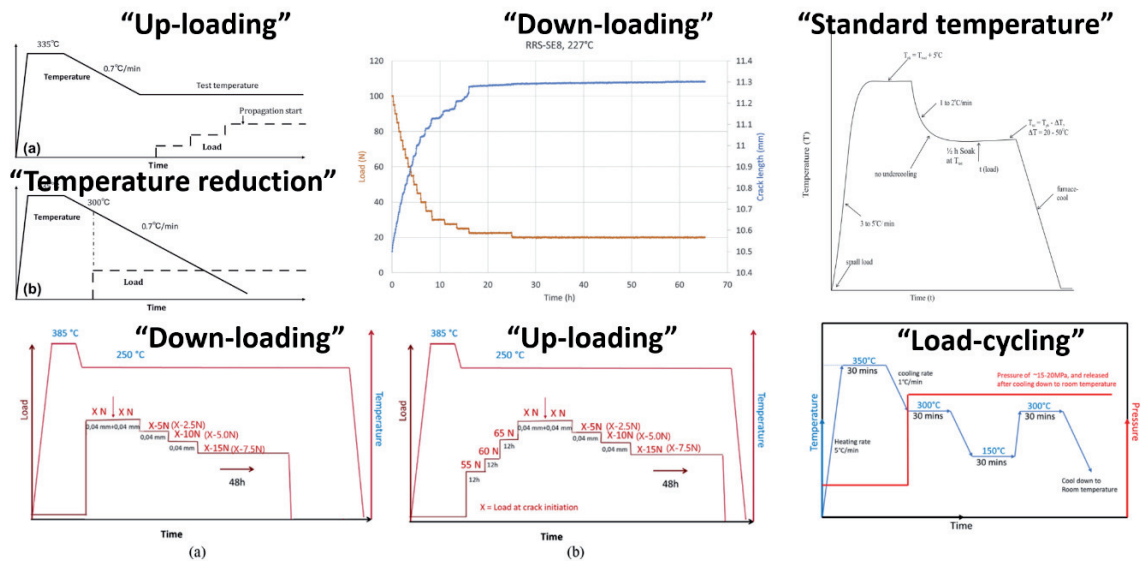
Figure 2.4: An overview of some of the various loading parameters that have been employed to test DHC. From references [13], [66]–[69]**.**

The temperature parameters were also varied depending on the objective of the test. It is most common to test from a higher temperature, which in a practical sense, represents the cooling of the given material from operational temperatures. The temperature was increased above the TSSd limit for a given time to ensure that all hydrogen was in solid solution at the start of

the test. Care was taken not to undercool the samples in such tests, which would lead to excess precipitation prior to the test. Some tests had begun from heating rather than cooling to see possible hydride hysteresis effects, while others reduced the temperature throughout loading to investigate K_{IH} based on temperature. The kinetics of dissolution and nucleation which effect the direction of heating are described in the following references [70], [71].

The majority of DHC experiments reported on in literature have used the standard compact tension tests with modified specimen geometries [66], [72], [73]. Because the samples are cut from pressure tubes of CANDU reactors, the specimen contains a slight curvature along the height, as seen in Figure 2.5.
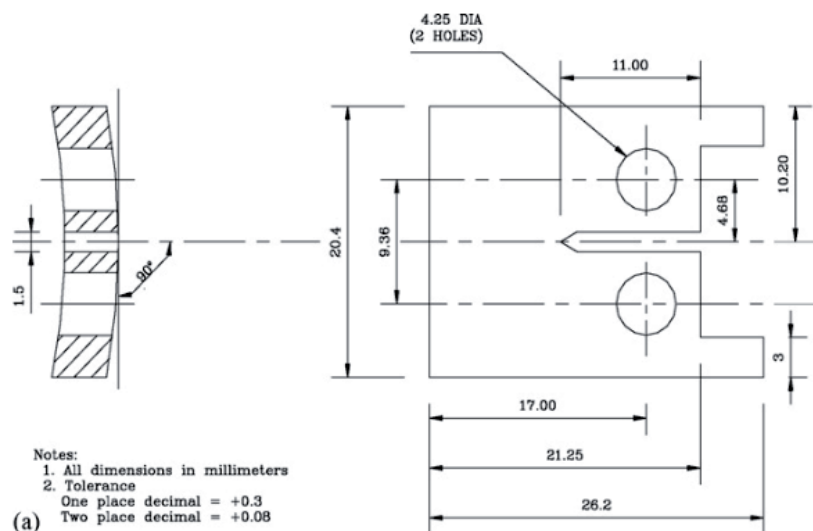
Figure 2.5: A typical compact tension (CT) specimen cut from a CANDU pressure tube with a wall thickness of about 4.0 mm. From reference [14], [74]

Some tests adapted to fuel cladding to test DHC as seen in Figure 2.6 and Figure 2.7. In these figures, the specimen geometry is described along with the test setup. The ring tensile test was performed in-situ that the crack could be observed with a scanning electron microscope (SEM).
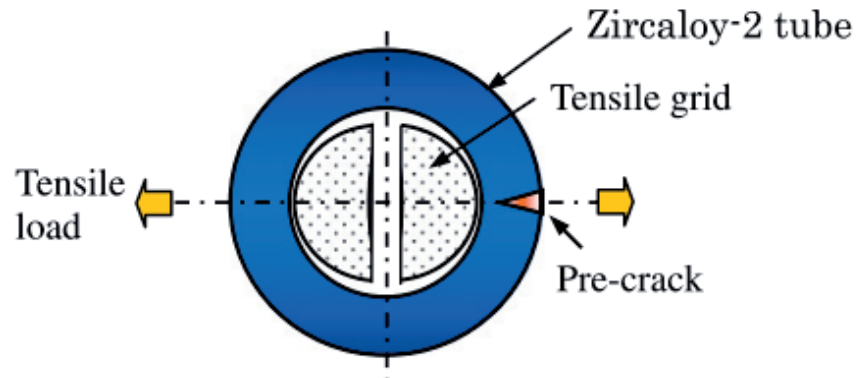
Figure 2.6: A typical in-situ ring tensile test. Taken from [67]**.**

The pin-loading tension test creates two cracking sites at one end of the fuel cladding. The two cracks are symmetric relative to the loading vectors and propagate axially.
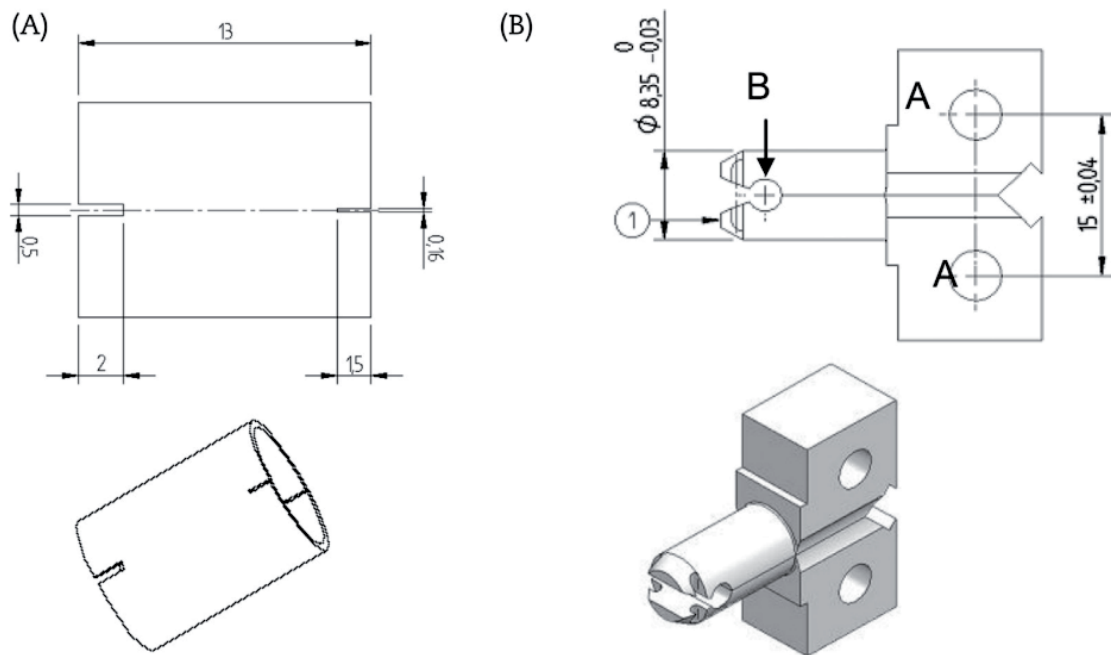
Figure 2.7: A typical pin-loading tension (PLT) experiment. A) shows the PLT specimen and B) the fixture. From reference [66]**.**

In Figure 2.8, a cantilever beam setup is shown describing how pressure tube material has alternatively been tested.

With the PLT and CT geometries, cracking propagates in the axial direction through the tube. Therefore the crack propagates through the entire wall thickness, making it unable to tests effects from variations in the tube material, for example, in the case of inner liner materials. Additionally, as there is strong texturing of the tube material, mechanical properties may be different in other cracking directions due to the anisotropy of the crystal orientation.
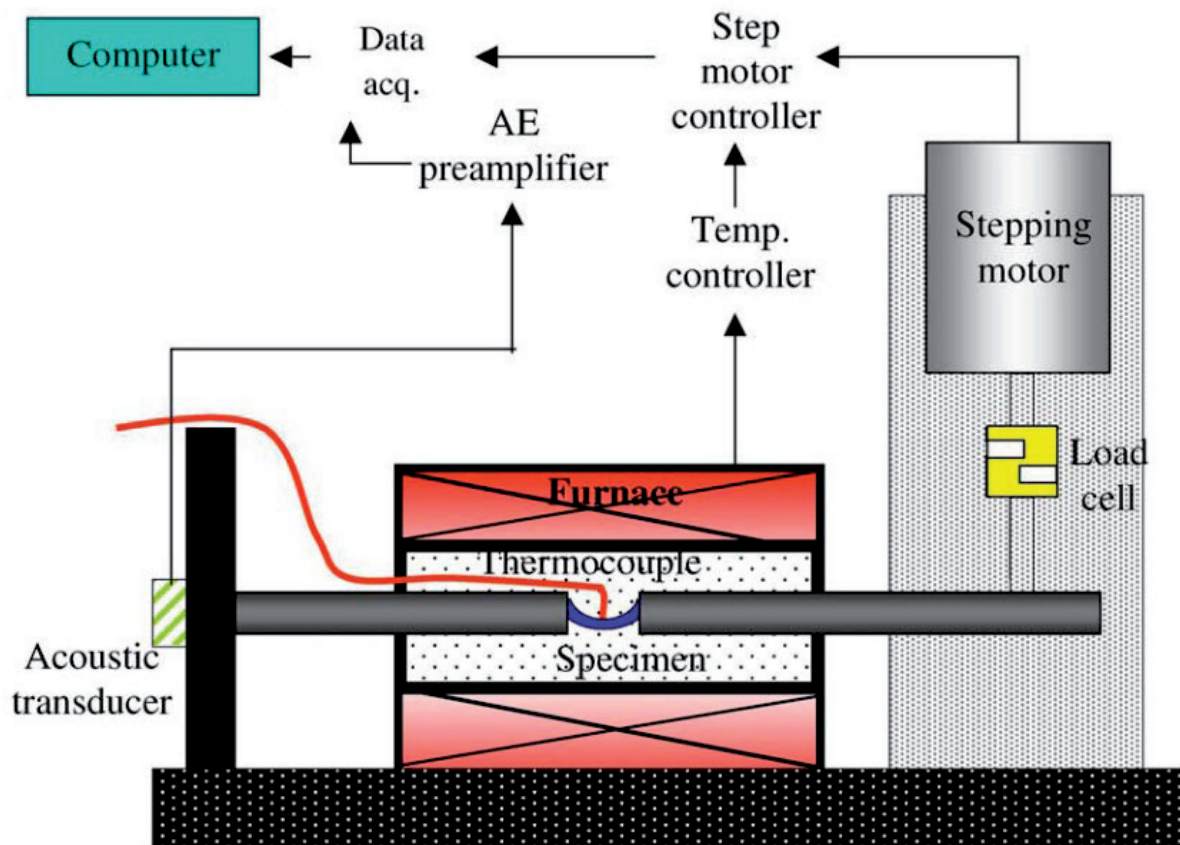
Figure 2.8: A typical cantilever beam test setup. Taken from reference [59].

2.6.4. Results of recent DHC experiments

Typical results from DHC testing in literature include the following observations and properties:

– Fractography: Crack surfaces describing the crack propagation.

– Metallography: Polished cross-sections of the DHC crack providing a view of hydride precipitation

- Crack velocity measurements (DHCV)

- Threshold stress intensity factors (K_{IH})

In the following subsections, each of these points will be addressed in the context of current literature.

1. Fractography:

    In Figure 2.9, an overview of the various observations made from DHC cracking in pressure tubes and fuel cladding can be found. Extensive testing has been done to determine the effects of the striations during DHC, if any at all, and the spacing between each striation. The effects on the extent of tunneling has also been studied, including the temperature of testing and samples geometry. The crack front shape is observed to evolve as the crack propagates farther from the pre-crack due to various factors, namely the symmetry of the loading during DHC onset.
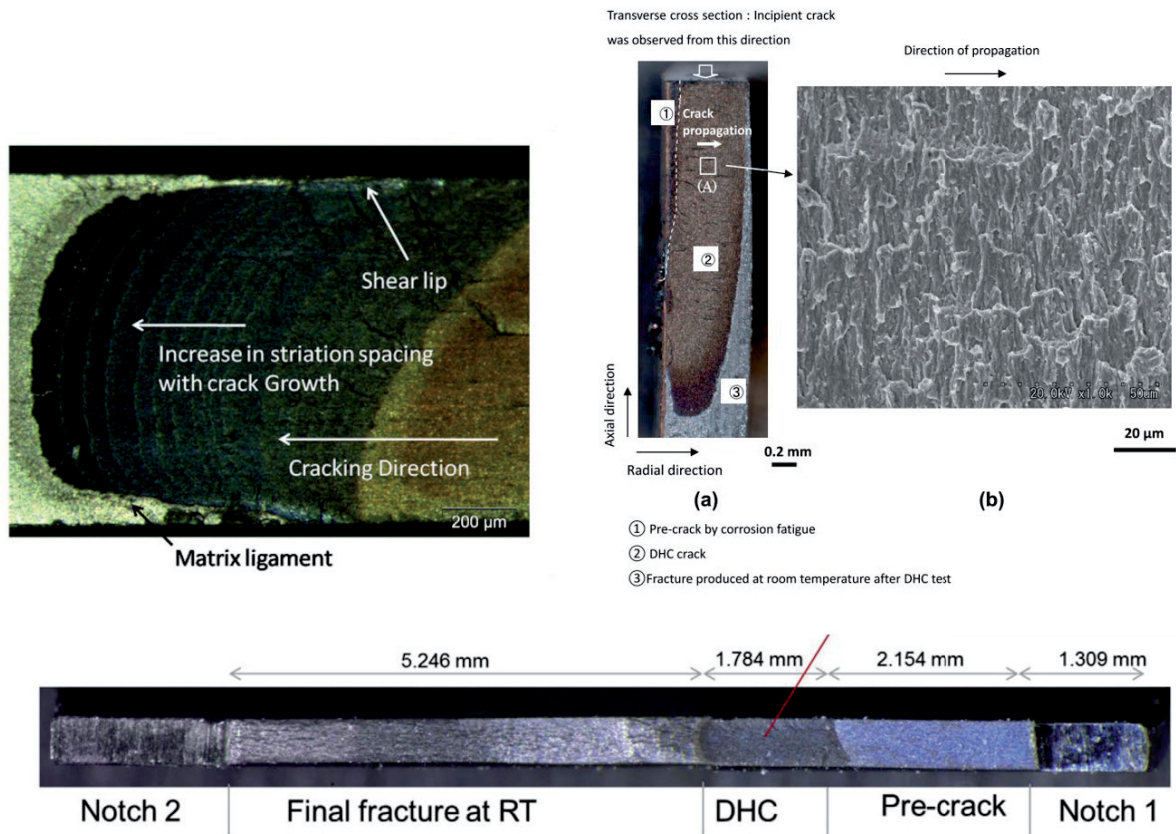
Figure 2.9: A summary of fractographic results from different DHC tests. Taken from reference [66], [67], [74].

More specifically, the striations during DHC have been observed in large specimens, such as CT or single-edge notch tension (SENT) pressure tube samples, to be an iterative process due to the incubation period required for proceeding hydrides to become of critical size [11], [14], [61]. In many studies, the incubation time, among other variables, have been correlated with the striation spacing within the DHC zone, where striations range between 20 and 60μm [73]–[76].

2. Metallography

The metallographic overview seen in Figure 2.10 provides insight on the nature of how hydrides precipitate. It can be seen that the orientation and propagation direction of the crack affects how the hydrides will precipitate. Additionally, tests at different temperatures

lead to changes in the amount of hydride precipitation due to the larger source of hydrogen in solution.
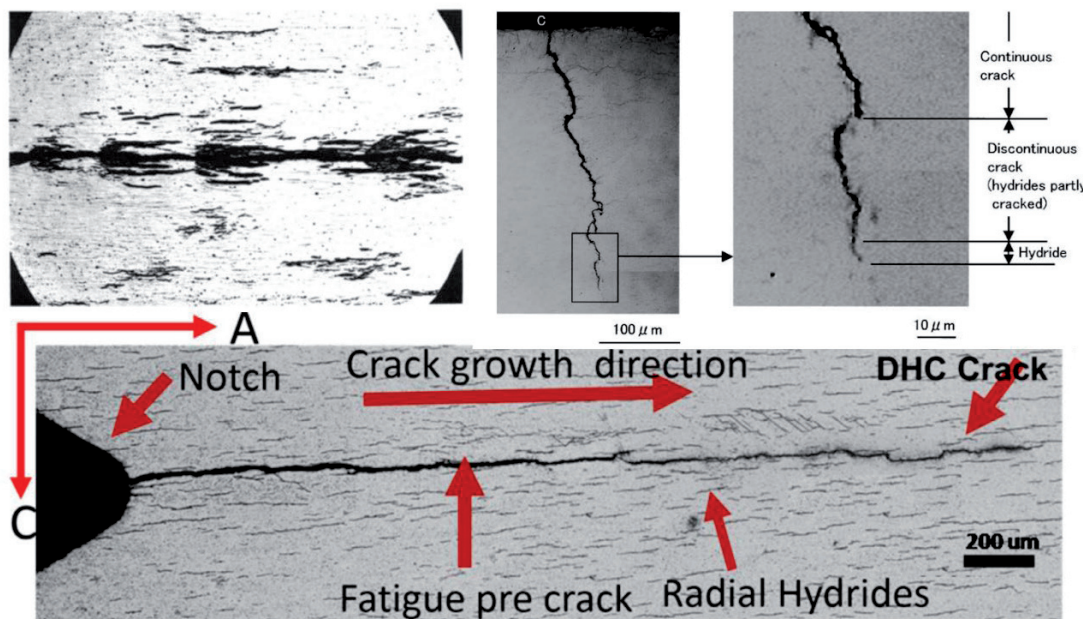
Figure 2.10: An overview of typical metallographic examinations found in literature. Taken from references [11], [68], [77].

3. DHCV:

The velocity has been one of the most extensively measured properties of DHC due to the simplicity of the measurements. Typically, the cracked sample is completely fractured open at room temperature through further fatigue cycling or high loading. The different zones of the crack are then exposed and can be measures and correlated with testing time[13], [14]. Other tests have measured in-situ the DHCV with an SEM [67]. Not considering the cracking direction and orientation, typical velocity values range between $1 \times 10^{-11} - 1 \times 10 m/s$ in a temperature range from 100°C − 300°C [13], [44]. Typical velocity trends can be seen in Figure 2.11, where the lower range of temperatures follows the Arrhenius relationship.

Equation 2.7

$$V = Ae^{\frac{-E_a}{RT}}$$

In Equation 2.7, V, is a rate constant (DHC velocity), A, is the pre-exponential factor, E_a, is the activation energy of reaction, R, is the universal gas constant, and T, is the absolute temperature.
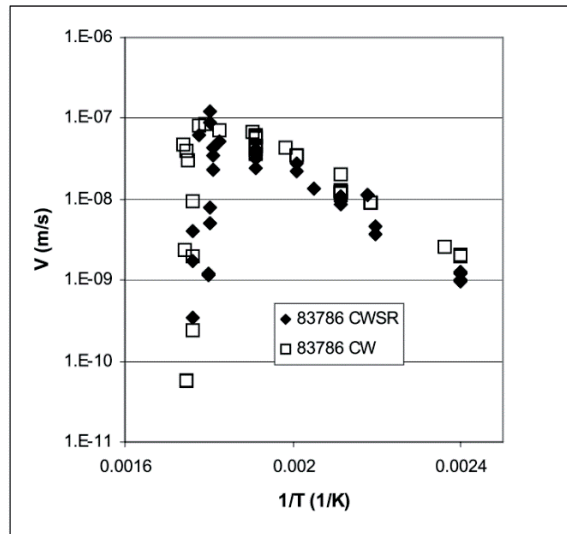
Figure 2.11: A summary of a crack velocities from a benchmark study conducted by IAEA [13].

4. K_{IH}:

Of all properties measured, the fracture toughness, K_{IH} is in a practical sense, the most important. Several studies have reported the K_{IH} for several different alloys of zirconium, as well as test types, parameters, and specimen geometries. Not considering the types of tests, parameters, or geometries, the range of K_{IH} has been reported from 2 to 20 MPa [67], [78]. However, it should be noted that the literature reports an increase in K_{IH} with temperature where creep begins to affect the cracking.

As seen from the recent studies performed, there are a given number of properties of interest in a broad context of materials and testing conditions. Therefore, the standard mechanical

tests and fracture mechanics, which this study is based on, are described in the following subchapter.

2.7. Three-point bending test

Three-point bending testing is a technique which allows for testing various properties of a material that include, while in a flexural mode, the modulus of elasticity, E_f, the flexural stress, σ_f, and the flexural strain, ϵ_f [79]. The testing technique also allows to test the fracture toughness of materials [80]–[82].
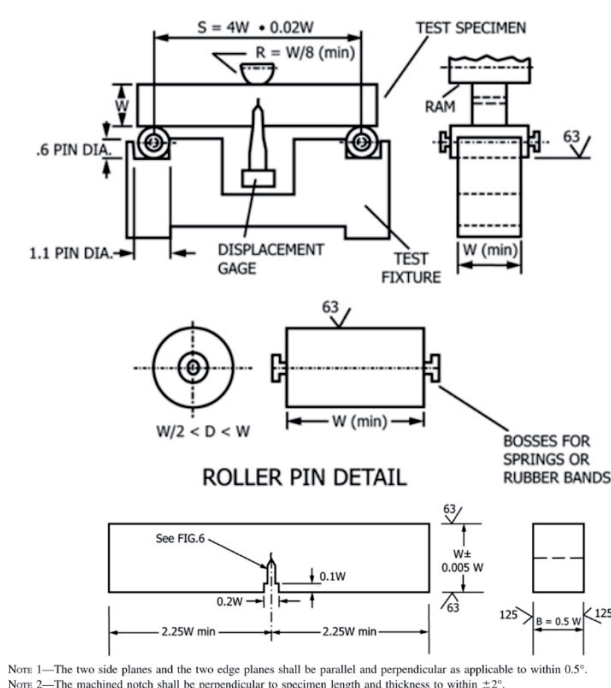
Figure 2.12: The upper diagram describes the ASTM standard for a fixture, which can be used in a fracture toughness test, and below the respective dimensions of the sample. Taken from reference [81].

When tests are adapted to the specifications defined by the ASTM standards, given empirical equations may be used to determine the fracture toughness of the material [80]. The three-point bend test is ideal for testing homogenous materials because of its ability to consistently focus on the loading at the failure point where the average behavior of the material can be captured [83]. In the following subchapter a brief overview of fracture mechanics is given.

2.7.1. Fracture mechanics

Fracture mechanics is subdivided into two areas, linear-elastic fracture mechanics (LEFM), and elastic-plastic fracture mechanics (EPFM). The two areas are differentiated by the amount of plastic deformation that occurs at the crack tip. LEFM can be generally described where the plastic zone at the crack tip, defined with radius, r, is sufficiently small that the small-scale yielding occurs. Small-scale yielding occurs when r is significantly smaller than the crack length, a, i.e., $r \ll a$. The opposite can be defined as large scale yielding where, $r \geq a$. Once large scale yielding occurs the fracture mechanics are defined by EPFM [84].

The fracture criterion or propagation at the crack tip has been defined by the energy balance combined with fracture. Irwin had defined fracture toughness of a material through the stress intensity at the crack tip, i.e. the stress intensity factor, K [85]–[87], with units MPa√m. Generally, K is used to define the crack stress state characterized with LEFM [80], while materials characterized with EPFM, are defined using the J-integral [81]. The J-integral is based on the strain-energy release rate (work energy) per cracked surface of propagation with units (J/m^2).

There are three different modes of failure in fracture mechanics, which are generally described in Figure 2.13 [84]. The most commonly mode tested, and the mode focused on in this project, is mode I.
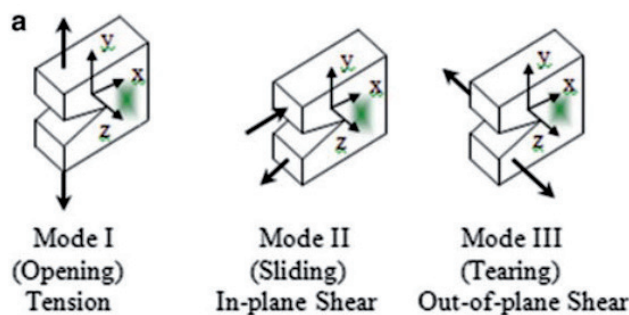
Figure 2.13: A diagram of the three failures modes. Taken from reference [84]**.**

In the context of this project, the fracture mechanics are focused on the tension mode I given that three-point bending tests are used. Additionally, LEFM is considered for modeling purposes as the hydrides, which primarily constitute the cracked matter, are highly brittle. However, it should be noted that the overall fracture mechanics might consist of a LEFM and EPFM part, considering the softer matrix (susceptible to plasticity) in which the hydride is contained.

3. Materials and methodology

This chapter presents the material investigated in this work. Details include the origin of the material, the preparations required for each material, and irradiation histories of the irradiated material. Lastly, the analytical techniques used to investigate the material are discussed.

3.1. Unirradiated Zircaloy-2 (LK3, LK3/L, SINQ Target Rod)

The materials used in this study consisted of irradiated and as-received Zircaloy-2 fuel cladding tubes and spallation target rods. The LK3 and LK3/L material are from Westinghouse without and with an inner liner, respectively. Dimensions of each of the materials studies are shown in Table 3.1. The Zircaloy-2 composition can be found in Table 3.2 that are according to the standards (ASTM B-811) and (ASTM B-353) for LK3 and SINQ target rod material respectively.

Table 3.1: List of inner and outer diameters for materials tested.

Alloys (Zircaloy-2 based)	Inner liner thickness	Nominal Dimension	
		ID (mm)	OD (mm)
LK3	-	9.62	8.76
LK3/L	70±40 µm	9.62	8.38
LK3/L*		10.3	8.94
SINQ Target Rod	-	10.75	9.3
SINQ Target Rod**	-	10.75	9.3

*Irradiated in KKL **Irradiated in SINQ

Table 3.2: ASTM specifications (weight %) of the Zircaloy-2 material and respective liner used in this study.

	Sn	Fe	Cr	Ni	O	Si	Zr
LK3 and SINQ target	1.20-1.70	0.07-0.20	0.05-0.15	0.03-0.08	0.10-0.14	max. 0.009	bal.
Liner	max 0.3	max 0.07	-	-	-	-	bal.

3.1.1. Liner Material

In the case of boiling water reactors (BWR) there is an additional interaction between the fuel pellet and cladding material compared to pressurized water reactors (PWR) due to the nature of a BWR leading to more pellet thermal expansion during power increase. The interaction is known as pellet-cladding interaction (PCI) which can lead to internal stress-corrosion cracking. In the 1980's a multilayer cladding was developed to mitigated PCI through the addition of an inner liner to the standard zirconium alloy cladding [88]. Recently, the effects of a liner on hydrogen diffusion and precipitation kinetics has been explored [10], [89]. It has been shown that the hydrogen is strongly attracted to the liner-matrix interface where it subsequently precipitates after exceeding the local solvus limit. The primary reason for the hydrogen attraction towards the inner liner is the lower chemical potential of the liner as hydrides precipitate. The lower chemical potential results in a driving force for further diffusion of hydrogen towards the liner.

3.2. Irradiated Zircaloy-2 (LK3/L, SINQ Target Rod)

3.2.1. Irradiation history

The irradiation history of the materials used in this study can be found in Table 3.3. The irradiated LK3/L and SINQ target rod material have different primary irradiation sources. The LK3/L material was irradiated as cladding of a fuel rod in the Swiss boiling water reactor of Leibstadt, KKL, while the SINQ target rod was irradiated through proton irradiation and by the created spallation neutrons emerging from the enclosed lead target. In brief, the SINQ target rods are stacked horizontally on top of one another ('cannelloni' structure) with space for the heavy-water coolant to flow in between as seen in Figure 3.1.
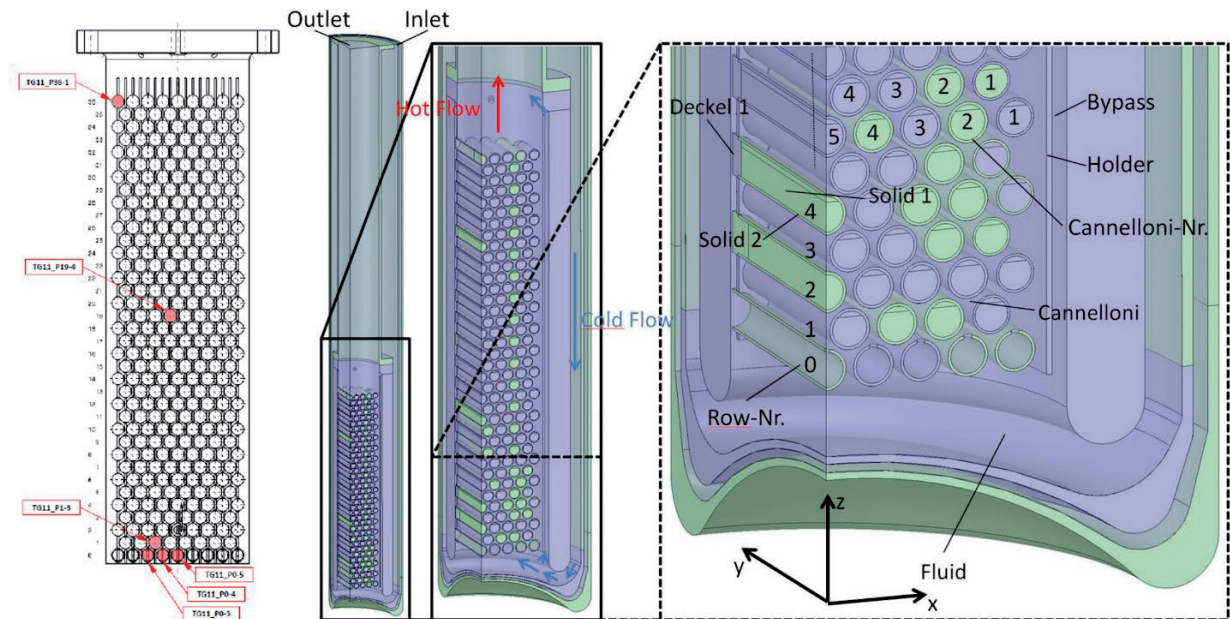
Figure 3.1: A two-dimensional overview of the SINQ target (left), with a CAD overview of one-quarter symmetric of the target (right). Taken from reference [90].

The target is irradiated by a vertical proton beam (~570 MeV) from the bottom-up. Material from the 0th, 1st, and 19th row, was used for DHC testing. The 0th row was the bottom-most stack of rods, which was filled with coolant, while the 1st and 19th rows correspond to the first and middle lead filled stacks respectively. More details on the SINQ target rod locations,

dimensions, irradiation history, and results of post-irradiation examination (PIE) can be found in the following references [91], [92].

Table 3.3: Irradiation history of the irradiated LK3/L and SINQ target rod material.

Assembly Nomenclature (Type)	Rod Av. / Peak Burn-up or dpa	Annual cycles	Elevation (mm)	Filling Material	Material Purpose
AIA003-H6 (LK3/L)	57.5 / 65.7 [MWd/kgU]	7	1877-1967.5	UO_2	Nuclear Fuel Cladding
TG11-P0-3-2 (Zircaloy-2)	~25 dpa		0th Row	D_2O	Spallation Target Rod
TG11-P1-3-3 (Zircaloy-2)	~18 dpa	0.75*	1st Row	Pb	
TG11-P19-4-3 (Zircaloy-2)	~9.5 dpa		19th Row		

*2-year cycle length

The details of the burnup and location of the irradiated fuel cladding can be found in the following reference [93]. The specific details of the irradiation damage calculations of the SINQ target rod samples can be retrieved in the following reference [94]. In general, the irradiation damage is calculated based on the following equation with flux information based on the MCNPX model.

Equation 3.1

$$R = \sum \Phi(E) * X(E)$$

where, R, is the radiation damage, $\Phi(E)$, is the neutron and proton fluence for the respective energy bin, and $X(E)$, is the respective cross section at the given energy, E.

3.3. Sample preparation

The sample preparation for the materials largely depended on whether it was unirradiated material or irradiated. The unirradiated material was simpler to prepare with far less safety concerns. Therefore, all unirradiated material was self-prepared with the tools described in the following sub-chapters. The irradiated material was all prepared for examination within the Hot Lab of PSI with the help of several technicians.

3.3.1. Unirradiated material

The procedure for sample preparation of unirradiated material included hydrogen charging, heat treatment, and subsequent notching and cutting.

3.3.1.1. Hydrogen charging and homogenization

Sections of the as-received material were charged with hydrogen using a Sievert's type apparatus. The process comprised the material being held in a high vacuum at 400°C and the ingression of high purity hydrogen. The hydrogen uptake was controlled via a pressure drop, which correlated to the amount of hydrogen absorbed by the material. A detailed description can be found in the references [10], [95]. The choice of hydrogen concentration for the LK3 and LK3/L cladding material was based on the optimization for neutron imaging while remaining in an industrially practical range. In other words, the hydrogen content was as high as possible for optimized attenuation with neutrons while staying low enough to represent SNF conditions. The choice of unirradiated SINQ target rod material hydrogen concentration was based on assumptions from metallographic images of irradiated material [91] and preliminary neutron radiography. All samples were heat treated at temperatures above the respective TSSd for 10 minutes and quenched to achieve a hydrogen distribution as homogeneous as possible [96]. This was repeated around three times. The hydrogen content was validated

through Hot Vacuum Extraction (HVE) measurements as discussed in chapter 4. A brief description of HVE is found in a later subchapter.
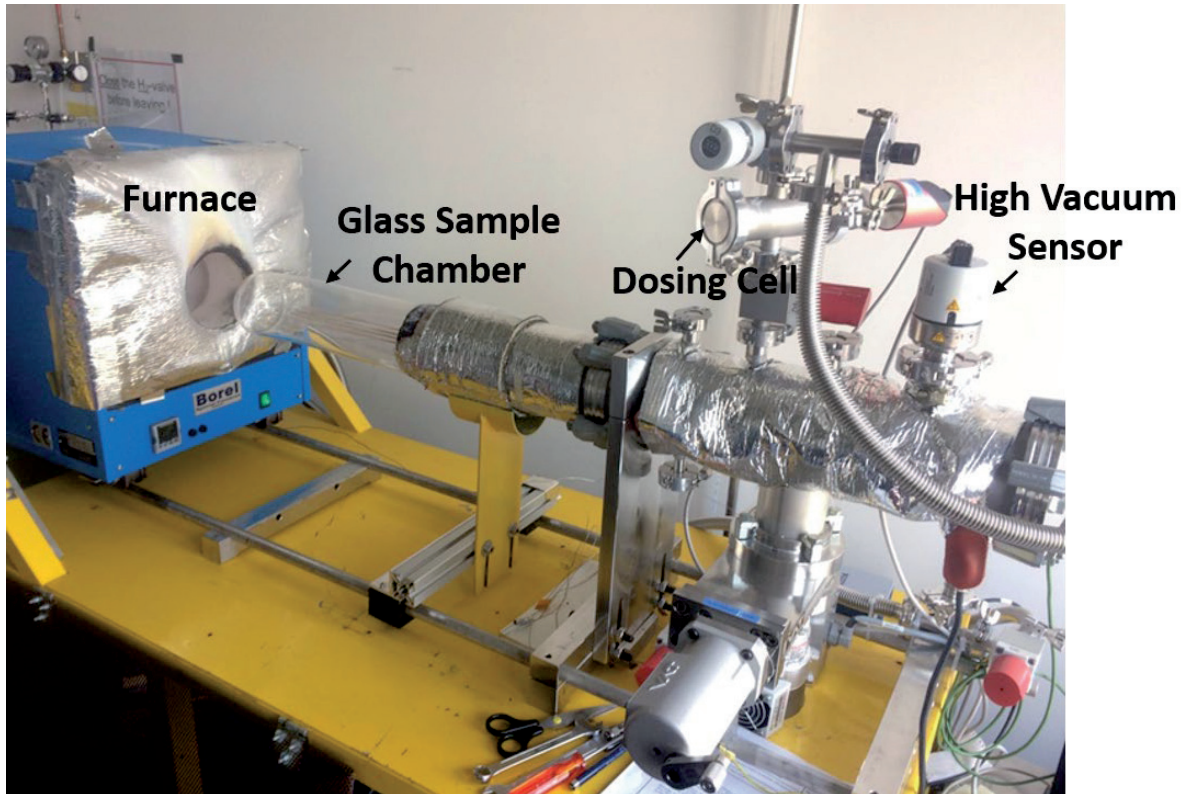
Figure 3.2: Device used to charge Zircaloy cladding tubes with hydrogen.

3.3.1.2.   Notching and cutting

Prior to fatigue pre-cracking a notch was cut into the sample in order to create a stress-concentrator. The notch allows the stress to be focused along a certain region during the pre-cracking phase to determine the crack location. For standard testing shapes there are common standards for the notch [80]. However due to the dimensions of the cladding, it was not possible to create a test sample in conformity with any standard. Typically, the notch length is half of the specimen thickness [80], [97]. In the case of the cladding material in this project, the thickness was between 0.4-0.7 mm making notching impossible with any standardized tool. Especially in the case of the liner material (~70 µm liner thickness), the notch depth should be strongly considered in order to study the effects of the liner. For this project, a unique

notching device was designed and developed (see Figure 3.4). The device consists of two parts. First, the sample holder (mini-vise), which was mounted to the base platform with a right angle bracket and two linear tables for accurate positioning. Opposite to the clamped tube was a liner table that oscillated along the vertical axis, as the cladding tube was positioned, via a rack-and-pinion drive. The sample was then driven into the razor until contact whereupon the razor oscillated up and down. As the razor began to oscillate freely, indicating the removal of material, or the start of a notch, the sample was driven closer. The process was continued iteratively driving the samples closer until around 0.5 mm total travel. The resulting notches were between 50 and 80 μm deep and had a root radius of approximately 30 μm. The tube material was sectioned into 4.0 mm rings that were subsequently cut in half resulting in the final arc-shaped specimen. The final specimen dimensions were a 4.0 mm specimen thickness, B, and width, W, respective of the cladding wall thickness described above. The specimen thickness, B, dimension is defined according to ASTM nomenclature, and should not be confused with the cladding wall thickness. In the context of fuel cladding, the cladding wall thickness refers to the specimen width, W, in a 3-point bending test [81]. An overview of the process from charging to notching and cutting can be found in Figure 3.3.
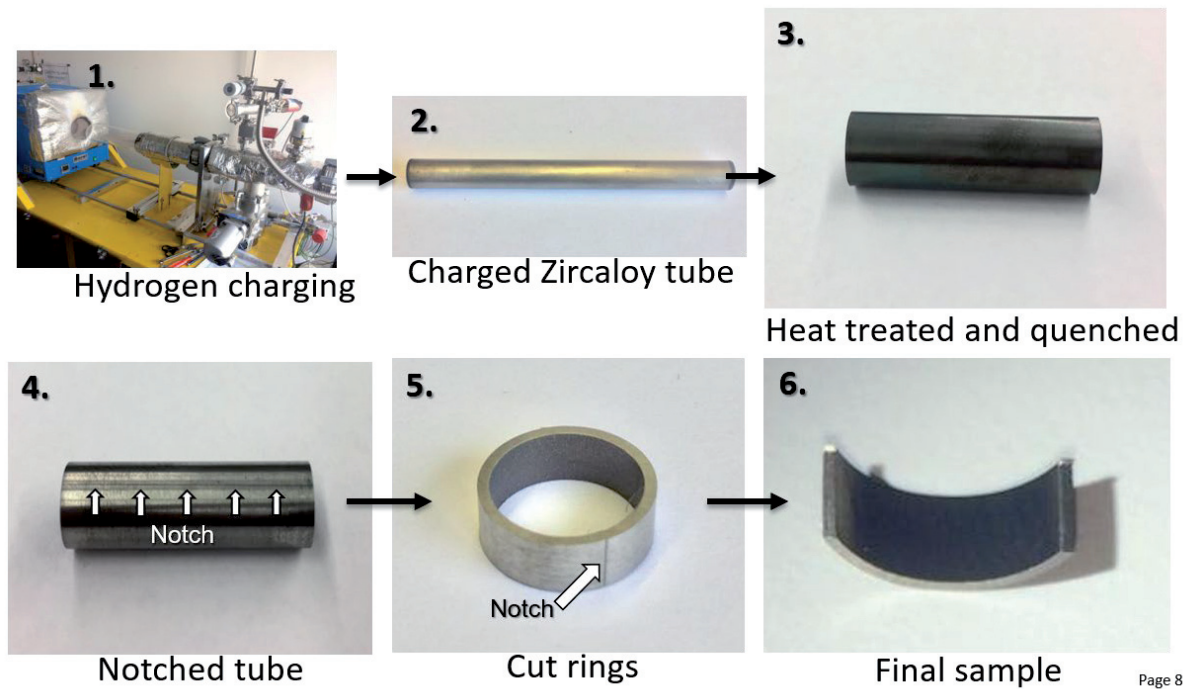
Figure 3.3: An overview of the sample preparation process from hydrogen charging, notching and cutting. The numbers indicate the process step order.

An important observation during the notching was the effect of the oxide layer. After heat treatment, the sample would be significantly oxidized (caused by the lack of inert atmosphere and water quenching) making it difficult to initiate the notch. Therefore, after such heat treatment, a quick polishing step was required in order to reduce the oxide layer and allow notch initiation.
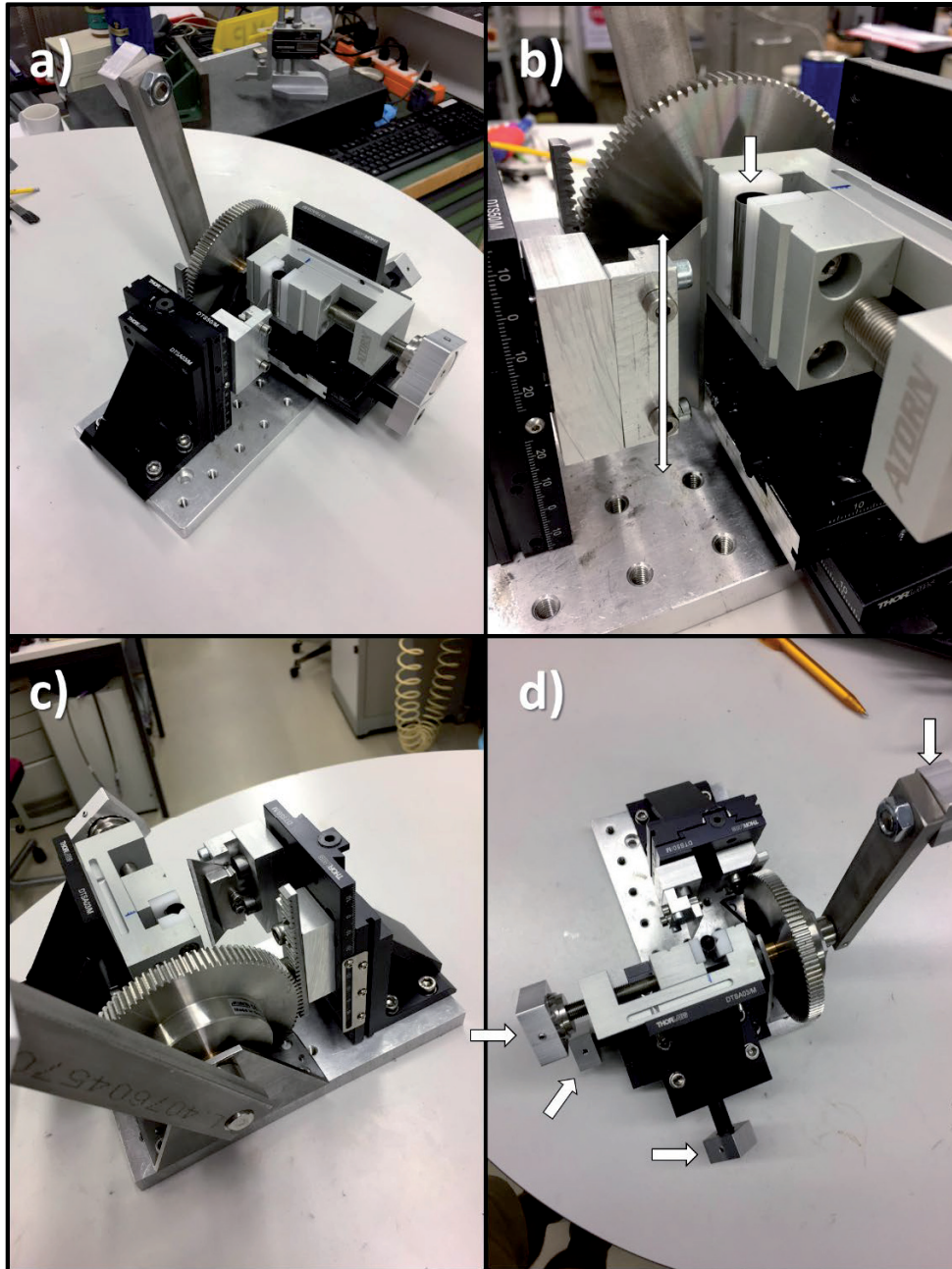
Figure 3.4: Device created for notching cladding tubes. a) projected view. b) The arrow indicates the cladding tube being held by the mini-vice where the double arrow indicates direction of razor blade oscillation. c) backside projected view d) The arrows indicate square grip for manipulation in a hot cell.

3.3.2. Irradiated material

The following subsection describes the notching and cutting as it differs from the unirradiated material. The irradiated material was not charged with hydrogen as it already contained hydrogen from the uptake during its operation in the nuclear plant or as target rod material SINQ.

3.3.2.1.   Notching and cutting

The irradiated material was prepared in the Hot Lab of Paul Scherrer Institut (PSI). The cutting and notching was done with the same tools, however in the opposite order for practicality (first cutting rings and then notching). Figure 3.5 describes the process showing the sample next to the holder (a), and the SINQ target rod sample being cut (b). The holder was designed to fix the sample with uniform force, specifically for the active samples to prevent undesired deformation in the saw clamp and ability to cut small sections from already small pieces. In the Figure 3.5 (c-e), the longer LK3/L material was held and cut sequentially so that the samples were accurately cut with minimum cutting loss. After cutting, the notching locations were marked Figure 3.5 (g). The following steps included notching using the device seen in Figure 3.4. . Considering the unknown oxide thickness and cutting difficulty, the irradiated samples were notched with little knowledge about the sufficiency of depth.
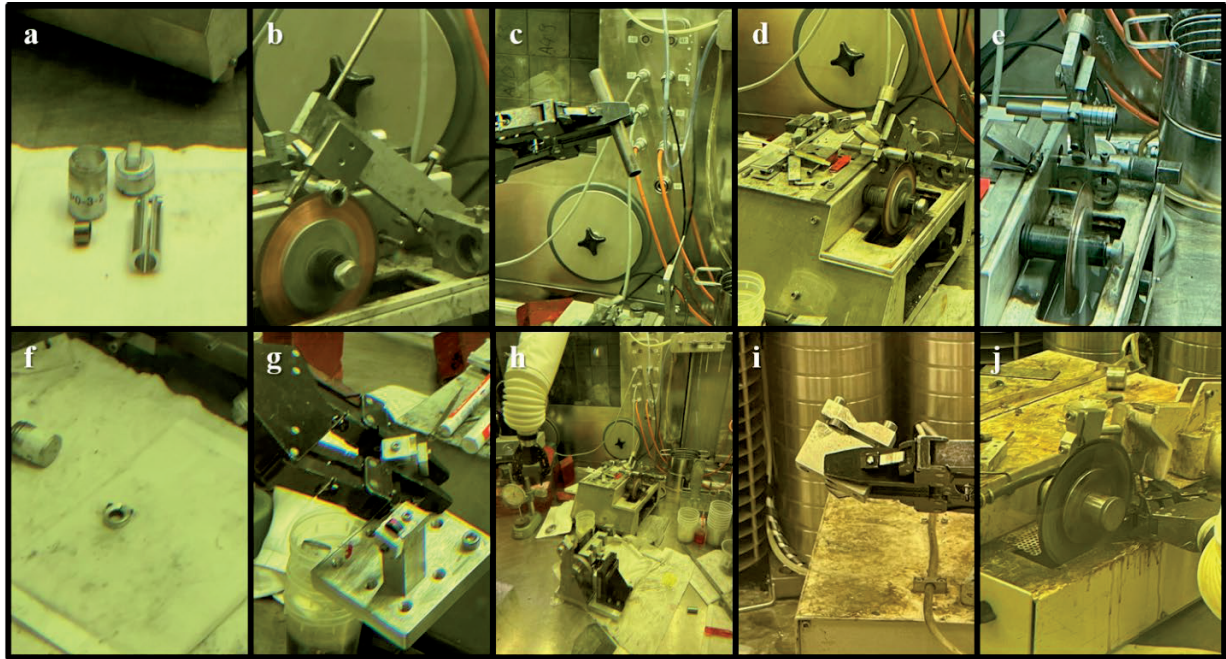
Figure 3.5: Overview of the cutting and notching of LK3/L and SINQ target rod material. a) 8 mm section of SINQ target material and holder, b) cutting of SINQ target rod, c) 90 mm section of LK3/L d) LK3/L material first cut, e) LK3/L sections of rings cut in holder f) cut ring of SINQ target material g) marking 90° sections for notching and cutting, h) notching device in hot cell, i) notched sample mounted for j) cutting in half ring as final specimen shape.

3.4. Characterization methods

The following subchapters describe the analytical methods used to investigate the DHC cracks including the various microscopy techniques and finite element modeling.

3.4.1. Light optical microscopy

Light optical microscopy (LOM) was utilized for imaging the fracture surface of the samples (fractography) and the polished cross section (metallography). The microscope was a Leica upright type microscope.

3.4.2. Scanning electron microscopy (SEM) and focused ion beam (FIB)

Scanning electron microscopy (SEM) and the focused ion beam (FIB) are combined techniques that have been used for imaging with high resolution and polishing very small regions with high precision. Generally, the intended use is for the preparations of samples used in TEM, other micromechanical test samples, and small cross sectional analysis. The SEM utilizes an electron beam to image a sample through various electron interactions with matter. Some of the interactions result in backscattering of electrons or secondary electron emission. These two interactions are the most important for this work, while the other interactions are briefly described in Figure 3.6.
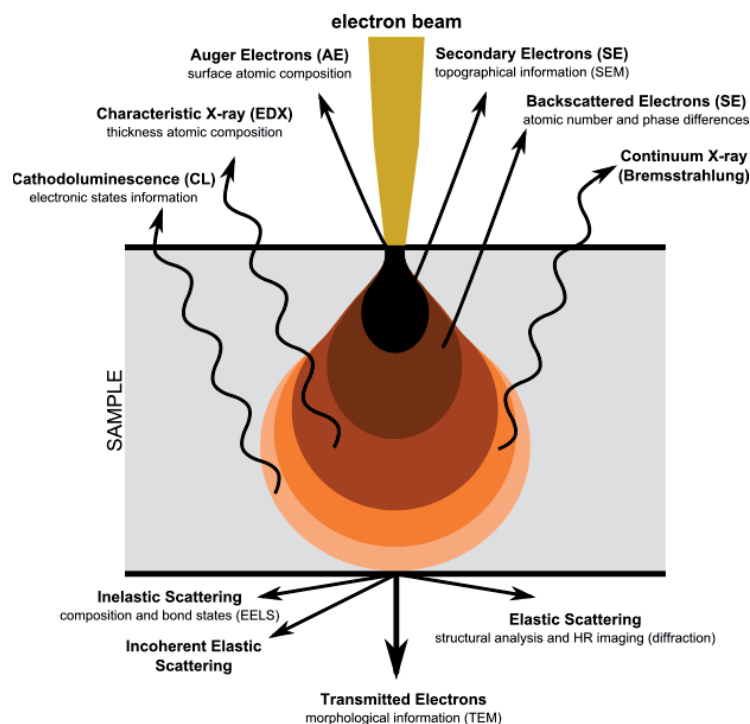
Figure 3.6: Summary of the interaction, which can occur from an incident electron beam with matter.

The back-scattered electrons (BSE) are primary electrons from the incident beam, which have been elastically scattered from the electrons of the target atoms. The energy that the electron

53

is scattered back is inversely proportional to the atomic number size of the target atom. The secondary electron (SE) is emitted from the inelastic interaction of the primary electron with the target atoms in which the energy absorbed by the atoms results in the emission of an electron from the target atom. As the energy of the secondary electron is much lower, the mean free path is smaller, leading to self-shielding of secondary electrons deep with the matter. The secondary electrons from the surface can however escape, leading to high topographic information. In combination with the Bragg law, secondary electrons can give some qualitative information about the crystal orientation, leading to distinction between the individual grains, otherwise understood as an effect of the electron diffraction. As the crystal orientation determines the depth at which the primary electron will penetrate, the secondary electrons will also originate at different depths of the same material in different grains. More specifically, a lattice structure aligned parallel with the beam will result in deeper beam penetration, while the beam will penetrate shallower for the less aligned lattice structure. The resulting image will show lighter grains where the incident electron originated at a shallow depth and visa-versa.

In this work, a BSE detector, and SE detector have been used to determine the location of hydrides in the zirconium matrix with respect to the crack. As the hydrides contain hydrogen, which has a small atomic number, the backscattered electron contains less energy and leads to a contrast that is darker than the surrounding matrix when using a BSE detector. When using the SE detector, the grains become visible along with the hydrides as the difference in crystal structure affects the SE emission.

The FIB uses a Ga^+ beam for milling and polishing very specific positions within the sample. The ion beam can view the sample through similar interactions as described for the SEM, however with a given amount of destruction. As the Ga^+ ions carry a much higher kinetic energy than the electrons of an electron beam, the target atoms are sputtered from the surface. Specific shapes and areas can be selected for milling allowing for very small sample preparation, as required by the synchrotron μXRD experiments due to very small transmission

depths of X-rays. In this work, the FIB was utilized to create a thin lamella of an intact DHC crack.

3.4.3. Finite element modeling (FEM)

Finite element modeling (FEM) is a technique used to numerically solve a system of equations that describes the system physics [98]. Given a complex or non-standard geometry, FEM can be implemented to determine the stress state by subdividing the system into less complex and smaller parts. The discretization is done by creating a mesh of the model with a finite number of points. Given the boundary conditions and system of equations describing the physics of the model, a solution can then be solved.

In this work, FEM is employed for solving the stress intensity factor of a representative crack within a model identical to the test setup. The model incorporates material properties of Zircaloy-2 and structural steel for the sample and fixture, respectively. The contacts are defined realistically with friction as described in the FEM results chapter.

3.4.4. Neutron radiography

Neutron radiography is a non-destructive radiographic testing method, which takes advantage of the neutron interaction with matter. Other radiographic methods employ X-rays that attenuate with matter primarily through the interaction with the electron shell. In neutron radiography, however, neutrons are primarily attenuated with matter through interactions with the nucleus of the incident atom. In general, for the energy spectrum used in neutron radiography, scattering interactions are the likeliest interaction. Scattering interactions can occur elastically, where the kinetic energy of the neutron/target system is conserved, and inelastically, where the kinetic energy of the neutron/target system is reduced via target excitation and ensuing gamma emission. In general, the probability that a neutron will interact with a target atom is described by the "neutron cross section" which is denoted by, σ, and has

units of 1×10^{-24} cm^2 or barns (b). The total interaction with matter can then be described with the macroscopic cross section, Σ, in Equation 3.2.

Equation 3.2

$$\Sigma = \sigma N \; [cm^{-1}]$$

where N is the number density of a given substance,

Equation 3.3

$$N = \frac{\rho}{A} N_A \; [cm^{-3}]$$

where, $\rho \; [gcm^{-3}]$ is the material density, $A \; [gmol^{-1}]$ is the atomic weight, and $N_A \; 6.0221^{23} \; [mol^{-1}]$ is Avogadro's number. With the macroscopic cross section, the beam intensity transmitted through matter can be described as a function of thickness as shown in Equation 3.4.

Equation 3.4

$$I = I_o \exp(-\Sigma \times d)$$

where I is the transmitted neutron beam, I_o is the incident neutron beam, and d is the thickness or length of matter the neutrons must pass through.

With respect to neutron detectors, the transmitted beam intensity is reported as neutron transmission, T.

As the neutron scattering cross-sections of hydrogen and zirconium differ greatly, neutron imaging is a well-suited analytical technique for hydrogenated zirconium alloys especially when hydrogen concentration gradients occur. It has been shown that the variation in contrast of the neutron transmission of flat zirconium material containing homogeneously distributed hydrogen and a homogenous microstructure is due to the total hydrogen content [10], [99],

[100]. In the following equation $T(x,y)$ is the intensity image obtained through pixel-wise referencing described by Gong et al. [10], [101] in x and y coordinates:

Equation 3.5

$$T(x,y) = \exp(-\Sigma_{as-received}(x,y) \times s(x,y) - \sigma_H N_H(x,y) \times s(x,y))$$

where $\Sigma_{as-received}$ is the total cross-section of the as-received material and $s(x,y)$ is the pixel-wise path length of neutrons through the sample. The effect of hydrogen is defined by the microscopic cross-section σ_H, which is primarily neutron scattering, multiplied by the hydrogen atomic number density N_H. As the samples in this study have nearly identical factors that could affect the neutron cross section, including length, microstructure, it is assumed that the neutron transmission value is only affected by the hydrogen concentration, thus simplifying Equation 3.5 to the following:

Equation 3.6

$$T(x,y) = a \times \exp(-b \times c_H(x,y))$$

where the variable a represents the neutron transmission in H-free material, while b represents the neutron sensitivity to the hydrogen concentration, c_H, in wppm H.

Given the large differences in the neutron scattering cross sections of hydrogen and zirconium, locations within the sample containing higher levels of hydrogen will scatter more neutrons, resulting in less neutrons reaching the detector at that location. For regions of higher hydrogen content, the image contrast will appear darker relative to regions of less hydrogen content.

3.4.5. μ-XRD phase mapping

At the μ-XAS beamline at the Swiss Light Source (SLS) of PSI synchrotron X-ray diffraction (XRD) experiments were performed with high-spatial resolution. The objective of the technique is to identify the hydride phases around the DHC, which might have been responsible for cracking. Various hydride phases can precipitate including the most common delta (δ) phase

ZrH$_{1.6}$, and the metastable gamma (γ) ZrH depending on temperature [43] [46]. Because the temperature range at which DHC can occur encompasses a range where various phases can exist, and the mechanical properties of the hydrides can change with phase and stoichiometry [35], [39], [102], [103], it is important to identify which hydride phases result from DHC at certain temperatures. Without phase verification, hydrogen diffusion and precipitation modelling would fall short of their ability to accurately model in a large spectrum of temperatures and cladding materials. With improved hydrogen modeling, the conditions of SNF can be better predicted.

Latest X-ray diffraction studies have been performed to determine the various phases of hydrides within zirconium alloys [43], [44], [104], and the strain within the oxide of irradiated zirconium alloy [105].

For this work, possible diffraction methods like transmission electron microscopy (TEM) or XRD could be used to identify the hydride phases. However, large areas of up to several hundreds of square microns are required. Desired hydrides within the sample can be very thin at the crack flanks and randomly dispersed throughout the sample matrix. Due to the mechanical instability, the samples could not be produced thinner than several microns. Thus, it was not possible to apply TEM diffraction techniques as such due to the limited observable region (tens of square microns) and risky sample preparation of a TEM lamella as it would necessarily include a relatively large flaw, namely the DHC crack. Therefore, the XRD-phase mapping technique available at the micro-XAS beamline was deemed as the best-suited technique for hydride phase identification.

3.4.5.1.   Diffraction

The unique crystral structre of each phase of material have unique 'fingerprints' that can be observed when analyed with XRD. The phsical law describing the diffraction of X-rays with a crystal lattice is Bragg's law. The wavelength of the beam is defined as, λ, and, n, is a given

integer. As described by Equation 3.7 and seen in Figure 3.7, the spacing of the lattice is given by, d, and the angle of scattering is represented as, θ.

$$n\lambda = 2dsin\theta$$

In an XRD experiment, given multiple crystals for a specific material, Debye-Scherrer rings, or diffraction pattern, can be observed as a result of diffraction [107]. Many types of information about the material can be observed through these rings including crystal structure, grains size, and residual stress. In this work the focus is solely on the crystal structure of the hydrides responsible for DHC. The diameters of the rings are representive of the 2θ angle in Figure 3.7. They imply the d spacing, or the Miller indices, {h,k,l}. The Miller indices represent the integers of the respective lattice vectors and are most commonly used to define diffraction peaks. The Miller indicies are helpful in defining peaks of diffraction patterns whenparameters of the different experiments (i.e wavelengths) might vary and result in different angles of diffraction.

3.4.5.2.   K-edge

With high energy X-rays, various attenuation lengths can be taken advantage of for a given material. The energy for the particular experiment must be optimized for the given material and available X-ray energy. In the context of this project, the target X-ray energy corresponded to the K-absorption edge as it corresponded to the largest attenuation length, ϵ, of the material within an available energy range. The larger attenuation length results in a smaller attenuation coefficient, μ, (Equation 3.8) and in turn a higher transmission of X-rays which can be diffracted through the crystal lattice of the material (Equation 3.9). The following equation describes the attenuation coefficient.

Equation 3.8

$$\mu = \frac{1}{\epsilon}$$

The following equation is a the Beer-Lambert law describing the ratio of transmitted X-rays, $I(x)$, to incident X-rays, I_0, as a relation to the material thickness, x, and attenuation coefficient. While similar to Equation 3.4, the attenuation coefficient can be written

Equation 3.9

$$\frac{I(x)}{I_0} = e^{-\mu x}$$

The K- absorption edge refers to the increase of photoelectric absorption of X-ray photons when energy levels exceed the binding energy of the Kshell electrons. Once the incident X-ray exceeds the binding energy, it is then capable of further interactions, hence photoelectric absorption of the X-ray and emission of the photoelectron. For zirconium the Kedge lies around 17.99 keV, above which fewer X-ray transmissions will occur compared to as below the edge [108].

3.4.6. Hot vacuum extraction

The hydrogen analysis is performed through HVE using both ELTRA at the University of Manchester, LECO-ONH836 at ETHZ, and LECO-3955 at PSI devices. Subsequent to charging the zirconium material, validation of the concentration was done by destructively extracting the hydrogen. This is done by rapidly heating the samples to a high temperature such that the hydrogen leaves the metal and flows with the inert gases. The physical properties measured with the devices were either infrared absorption or thermal conductivity. The calibration of the machine used to perform hydrogen analysis is critical for accurate measurements. It has been recommended to use calibration standards of similar hydrogen quantities that are to be expected in the subsequent samples measured.

4. Primary experiment

This chapter discusses the primary experiment of this project in which DHC cracking was produced. The following subchapters discuss the objectives of the test with a brief background justifying the tests. Subsequently, the set-up of the two devices for unirradiated and irradiated testing is described along with the loading schemes used for the various tests.

4.1. Three-point bending tests

The primary experiment revolved around the three-point bending test where cladding was tested as seen in Figure 4.1. A three-point bend made it possible to crack the cladding in a radial outside-in direction with an axial orientation of the cladding. The three-point fixture was designed with a span of 4.0 mm and fixed-rollers with a diameter of 1.0 mm. The bottom fixture was designed with stops to guide the sample placement towards the middle of the fixture. Displacement during the tests were measured through the extensometer displacement. The extensometer made contact with the side of the fixtures and the tips of the ceramic extensions.
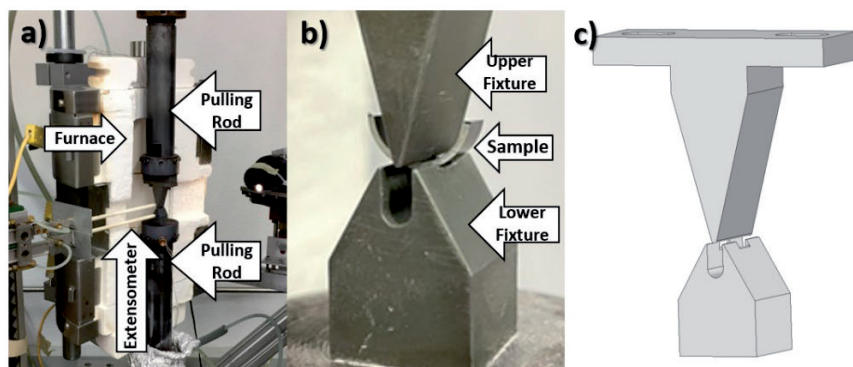
Figure 4.1: a) - the three-point bending test setup, displaying pulling rods, extensometer, and the open heating element. b) enlarged image of the three-point bending fixture displaying the fixed rollers and specimen in between. c) CAD image of the three-point bend fixture.

4.1.1. Objective of three-point bending

The following subchapters describe the conditions and assumptions of previous studies as well as the improvements that had been made in this work.

4.1.1.1. Previous DHC Testing

Previous studies on DHC contained certain assumptions in testing methods and conditions of which IAEA has suggested to improve upon in future tests [109]. Some shortcomings of the reported experiments include using standards for non-standard specimens and not exploring the more realistic radial crack direction, rather in the axial direction [66], [109]. It has been reported that the preferred crack propagation is axially oriented in the radial direction of the tube as in ramp, burst, and ring-compression tests performed to examine different scenarios which could include reactivity-induced accident (RIA) and loss-of-coolant accident (LOCA) conditions [110], [111]. In such scenarios, the crack generally propagates in a radial outside-in direction through the cladding as the internal pressure creates a tensile stress on the outer diameter of the tube.

4.1.1.2. Three-point Bending Advantages

Initial tests were aimed at achieving a radial crack through compression tests on C-shaped samples [32]; however, the large elastic deformation caused by the span inhibited precise control and cracking of the sample. The tests were then optimized and changed to three-point bending tests where the span was significantly reduced. An additional advantage of three-point bending is the high stress localization allowing for consistent testing on singular flawed regions, namely a single crack. These together ensure a rather straight crack in the radial direction. Additionally, with this method, it is possible to study the effect of an inner liner as the crack propagates towards the liner. Thus, the heart of this study is the three-point bending testing approach of fuel cladding and target rod material.

4.2. Test monitoring and control

The following subchapters describe the monitoring and control of the experiments including the differences in the testing devices for unirradiated and irradiated samples. Finally, the test setup and loading schemes are described.

4.2.1. Unirradiated material testing

The machine used to test the unirradiated material was an MTS Insight with a 1 kN low profile load cell, an encapsulating furnace, microscope camera, and extensometer. In this setup, the furnace encapsulated a significant length of the pulling rods and had two side openings for viewing the sample or inserting extensometer fingers. The temperature of the sample was monitored through a smaller auxiliary sample of the same material. The auxiliary sample was affixed to thermocouple leads via spot welding that were then connected to the control unit of the furnace. In doing so, the temperature could be controlled at the same time as it was monitored. For accurate control and monitoring of the test sample, the auxiliary sample was placed as close as possible and in a similar manner to the test sample. In the following Figure 4.2 it can be seen that the auxiliary sample is placed between the lower stage 'rollers' and just below the test sample.
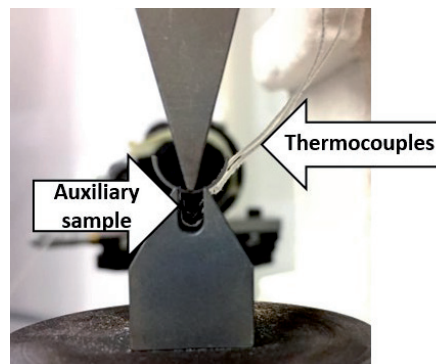
Figure 4.2: The three-point bending setup showing the position of the auxiliary sample and thermocouples. The resistive heating elements were monitored and controlled through the temperature measurement of the auxiliary sample.

4.2.2.   Irradiated material testing

The machine used to test the irradiated material was an MTS Alliance with a 1 kN s-type load cell. The pulling rods and furnace were located within a glove box behind lead shielding. Due to the more complicated set up, an extensometer could not be implemented. Therefore, the crosshead was used to monitor the deformation of the sample. As monitoring such small deformations with the crosshead is not ideal, care was taken to allow for temperature stabilization of the entire setup as well as to avoid driving the pulling rods in multiple directions. An external microscope camera was used for sample placement and in-situ monitoring. The temperature of the sample was monitored through an auxiliary sample of the same material, which had a dual-purpose, and was used as a clip for the thermocouple. This setup was an improvement designed for this test and future experiments. In other words, the Zircaloy-2 auxiliary sample was used to clip a single thermocouple lead to the side of the bottom stage. The thermocouple was then fed through a sealed stainless steel tube to the outside of the shielded and enclosed testing box, which was then connected to the control unit of the furnace. In doing so, the temperature could be controlled at the same time as it was monitored. Previously, temperatures were monitored and controlled via a similar thermocouple in a closed-end stainless steel tube which effectively created a significant barrier between the sample envirnoment and thermocouple envronment. It was observed that previous temperature measurements were inaccurately high by about 30-40°C. For accurate control and monitoring of the test sample, the auxiliary sample was placed as close as possible and in a similar manner to the test sample. In the following Figure 4.3 it can be seen how the thermocouple is clipped to the stage.
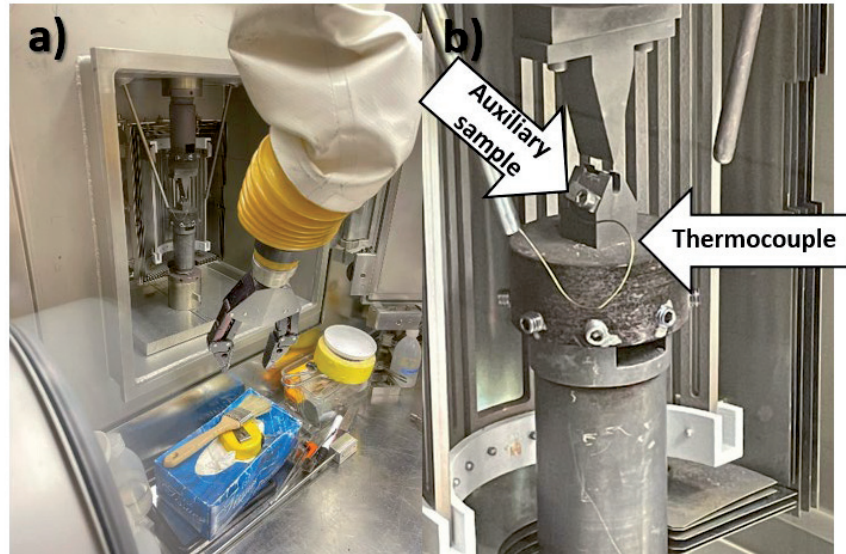
4.2.3.   Sample set-up and testing

Each prepared sample, as described in chapter 3, was placed in the three-point bending fixture and positioned with an external microscope camera such that the notch was aligned under the middle roller. Prior to the DHC test, a fatigue precrack was produced with cyclic loading and stopped at a specific extensometer displacement. A series of preliminary tests had shown that with a given displacement from load-controlled fatigue precracking, a relatively consistent precrack depth was achievable. The fatigue loading cycle had an R-factor (minimum load divided by maximum load) of 0.1. The extensometer displacement limit of fatigue was set based on a value that correlated to a crack length that has just entered stage 3 fatigue crack propagation. In other words, as the displacement increments for the cyclic loading scheme begin to increase, the crack length begins to enter stage 3 fatigue crack propagation as seen in Figure 4.4
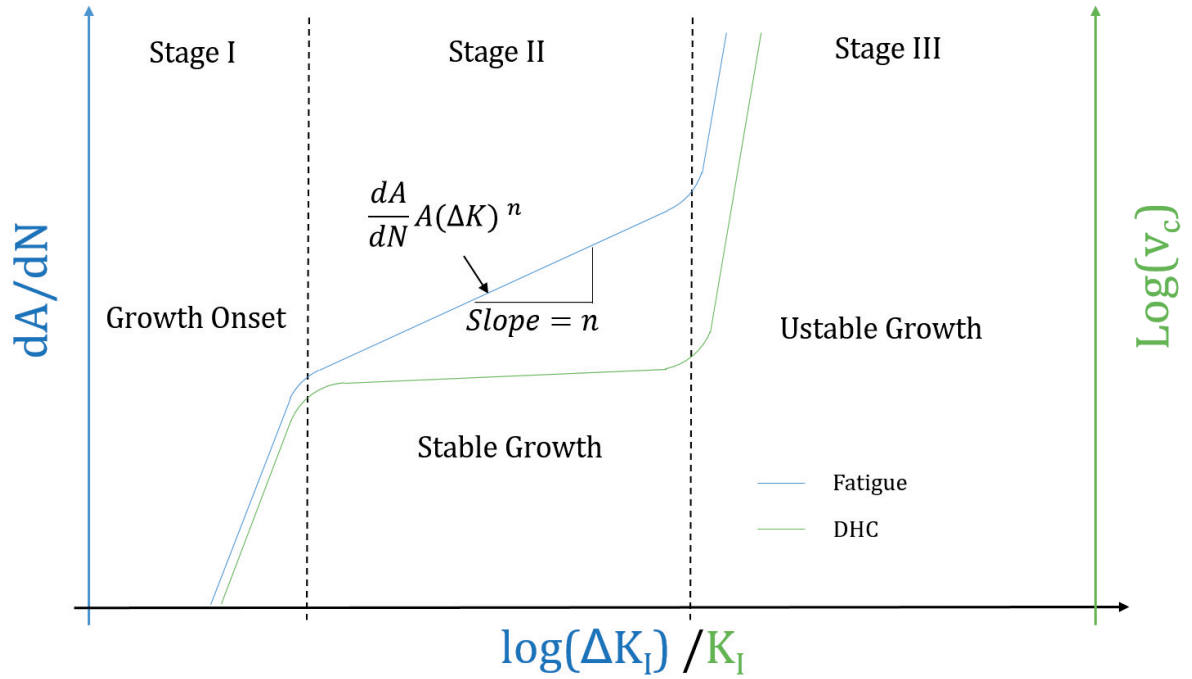
Figure 4.4: The three stages of fatigue (blue) crack and DHC (green) propagation are shown. Fatigue crack propagation is described per cycle (da/dN) vs. change in stress intensity factor log(ΔK) adapted from. [84] DHC is described with growth rate vs. stress intensity factor [11]. Note: The DHC growth rate in stage II is considered constant regardless of the stress intensity factor unlike stage II of fatigue crack growth.

Although the ideal fatigue precracking should end close to stage one fatigue crack propagation, however, due to the specimen geometry and test setup, methodology such as strain gauges and direct current potential drop (DCPD) measurements could not be employed. Fatigue precracking should end in stage one in order to have a crack tip radius as small as possible and to ensure a small plastic zone in front of the crack tip. Despite the fact that fatigue precracking ends in the beginning of stage three in this study, the crack tip is sufficiently sharp for consistent DHC onset. Additionally, according to the von Mises yield criterion (Equation 4.1), the more conservative Irwin approximation (Equation 4.2), and the given test conditions, the affected plastic zone is less than 8 μm immediately ahead of the crack tip which is significantly less than the total DHC propagation [112], [113].

Equation 4.1

$$r_y = \frac{1}{2\pi}\left(\frac{K_I}{\sigma_{ys}}\right)^2 (1-2v)^2$$

Equation 4.2

$$r_y = \frac{1}{6\pi}\left(\frac{K_I}{\sigma_{ys}}\right)^2$$

where the yield stress, σ_{ys} is 241 MPa, Poisson's ratio, v is 0.37 and the assumed K_I, was not larger than 3 MPa√m at the last cycle of fatigue. Typically, several hundreds of cycles to several thousands of cycles were required to meet the displacement limit for all the samples. The final stress intensity factor, K_I, of fatigue was generally double that of the DHC onset value as the maximum fatigue loading was usually double the initial DHC load. Specific details of the fatigue and DHC loading and limit details can be found in the Table 4.1.

The DHC test began by heating the sample to a temperature well above the TSSD, for 60 minutes to completely dissolve the hydrides present [96]. The sample was then cooled at a rate of 0.5°C/minute to the given test temperature, allowing the hydrogen to diffuse on a close-to-realistic time scale while arriving to the test temperature without undercooling. This test approach represents a DHC test temperature "upon cooling" [36]. After at least 15 minutes, ensuring the stability of the test temperature, the mechanical load was applied. The starting mechanical load during the DHC segment was determined through several preliminary samples where the crack velocity was subsequently measured, fitting well within the expected values of literature [114]–[116]. Through fractography of the antecedent cracked samples, the crack front dimensions were measured and implemented into the finite element modeling (FEM) model to calculate the K_I. The loading was reduced during the test as a function of extensometer or crosshead displacement. The reasoning for the load reduction was to ensure the stress intensity factor would remain within the stage 2 zone of DHC, as seen in Figure 4.4, providing a stable and constant crack propagation. Once a given displacement was measured

by the extensometer, correlating to a certain observable crack depth, the mechanical load was removed, thus arresting the crack and ending the DHC test. Specific details of the test, including displacement thresholds, can be found in Table 4.1. In Figure 4.5, typical load, and temperature trends after fatigue precracking are described for a general DHC velocity test.
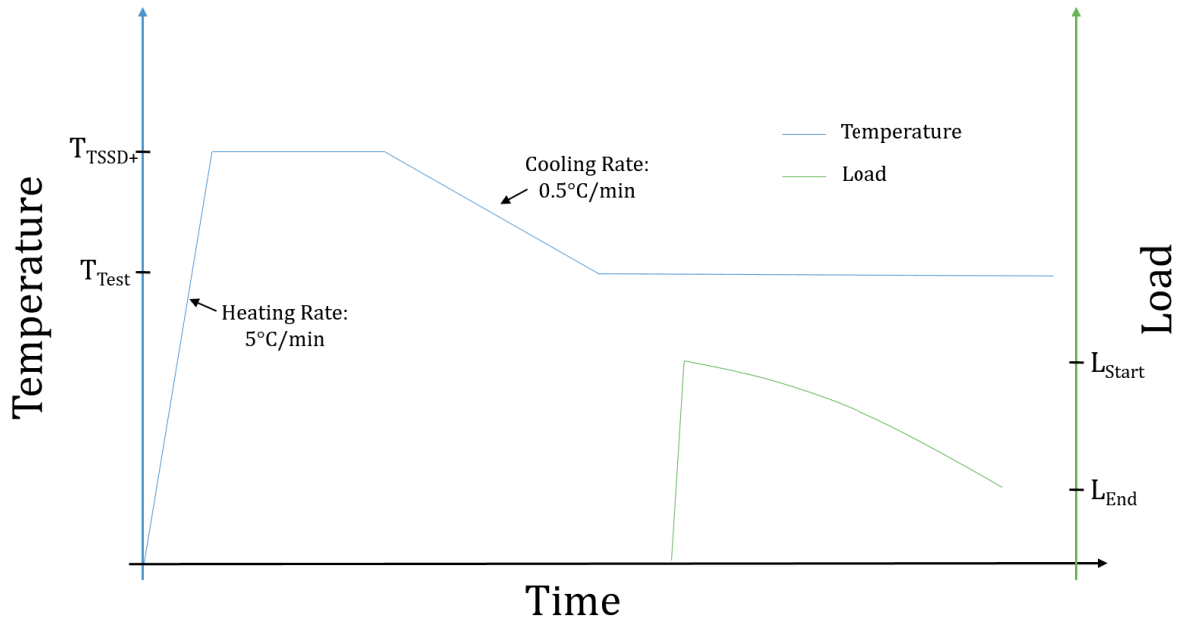
Figure 4.5: Typical DHC velocity test procedure subsequent to fatigue precracking. The temperature (blue) and loading sequence (green) are described with respect to significant temperature and load parameters.

4.2.4.   DHC loading schemes

Throughout this work, various loading schemes were implemented not only based on the type of test or material thickness but also the evolutionary stage of the work. In the beginning stages of the work, a constant load was applied to achieve DHC crack propagation. However, it was quickly recognized that K_I increased too quickly leading to premature failure. Therefore, a degressive loading scheme was implemented for all succeeding tests in order to maintain relatively constant K_I, and stable DHC crack propagation. The progression loading was

dependent on the extensometer displacement, where upon arrival at the initial load, the extensometer displacement was tared, and subsequent loading was redefined based on the current extensometer displacement. The iteration time steps for redefining the load were based on the expected time of the test and allowable computer storage. The following equation describes how the new load was calculated throughout the iteration:

Equation 4.3

$$l_n = l_o - r \times d$$

where l_n, is the newly calculated load, l_o, is the initial load, r, is the unload rate with units (N/mm), and d, is the extensometer displacement with units (mm). The initial values for l_o were dependent on the cladding wall-thickness and fatigue depth. The value for r was also dependent on the cladding wall-thickness, as well as the type of test performed. While K_I is sensitive to the crack growth, given dependence of K_I on the a/W ratio, it was necessary for thinner cladding specimens to have a larger r compared to thicker cladding samples. In addition, r was dependent on the type of test performed. Two tests variations were conducted, including crack velocity and the threshold K_I tests. For crack velocity tests, a moderate r was sufficient for crack growth stability, while a large r was required for threshold K_I tests in order to arrest a propagating DHC crack. Upon completion of each DHC test, each sample was water quenched from the test temperature and prepared for subsequent analysis. The post-test quench procedure would ensure that the hydrogen in solid solution was frozen into place rather than diffusing down the concentration gradient and naturally homogenizing itself.

Table 4.1: Loading parameters for the various materials tested.

Material	Fatigue Load (N)	Fatigue Extensometer / Crosshead Limit (µm)	Fatigue Cycles	DHC Start Load (N)	DHC Extensometer / Crosshead Limit (µm)	Unload Rate (N/mm)
LK3	10-100	100		50	40-120	50-300
LK3/L	20-200	80		90-100	40-120	60
SINQ Target Rod	30-300	80	1,000-10,000***	150	120	60
LK3/L*	30-300	145		100-240	140	53
SINQ Target Rod**	30-300	145		120-220	135	53

*irradiated in KKL **irradiated in SINQ (TG-11) ***notch depth dependent

5. DHC Velocity

In this chapter, the details of DHC velocity tests are listed. In the first subchapters, testing parameters and material details are compiled. The main results of the tests, including average crack length and velocity are then given. Lastly, the implications of the results are discussed, providing a comparison between the different sample sets.

5.1.   Motivation

Nearly all of reported DHC velocity measurements employed the use of pin loading tension (PLT) or compact tension (CT) techniques to induce DHC in fuel cladding or pressure tube materials [14], [66], [76], [117]. With these two techniques, axial cracking is induced through the wall thickness of the material. While axial cracking can occur in real cases, the most realistic orientation of DHC in fuel cladding is in the radial direction. This part of the study aims to compare the velocity of radially oriented DHC to the many axial velocity measurements reported in literature. It is important to investigate the radial orientation because there are distinct differences in the crystallographic orientation of the zirconium alloy due to pilgering (drawing and hammering) during fabrication and geometric effects. The orientation of the basal plane of zirconium hexagonal crystal lattice is then defined by the Kearns factors [118]. Therefore, a radially oriented crack will propagate in a direction normal to the basal plane, and parallel to the c-axis of the zirconium lattice. In axial cracking, the crack propagates in a direction parallel to the basal plane and normal to the c-axis of zirconium. Additionally, the geometry of the tests can have a large effect on the stress distribution at the crack tip. For example, the PLT tests apply internal loading to the cladding, which can lead to asymmetric loading as the internal surface bears more tensile load [76]. This is also the case for the CT tests on pressure tubes. However, the curvature of CT pressure tube samples is less than as fuel claddings, making the effect less prominent. Because of the asymmetric loading, cracking will begin at the inner surface causing the crack front to propagate to a preferred side until

72

stresses are symmetrically distributed along the crack front profile. With the radial cracks in tube samples, the crack front is symmetrically loaded. Therefore, considering the potential effects that the crystallographic orientation and sample geometry can have, it is important to investigate the velocity properties of DHC.

5.2.   Test parameters

The sample preparation regarding hydrogen charging, homogenization and final specimen cutting follows the procedure described in chapter 4. As described in chapter 4, each sample underwent fatigue pre-cracking, heat-up above the respective hydrogen dissolution temperature, and cool down to the defined test temperature.

5.2.1.   Loading parameters

The loading was defined based on the measured extensometer displacement.

Equation 5.1

$$l_n = l_o - r \times d$$

where l_n, is the newly calculated load, l_o, is the initial load, r, is the reduction rate with units (N/mm), and d, is the live extensometer displacement with units (mm). The tests were aborted once the extensometer displacement reached the defined limit, ext_{lim} (μm). In Table 5.1, the specific values for the parameters can be found.

5.2.2.   Temperature parameters

The temperatures for hydrogen dissolution and testing can be found in Table 5.1.

Table 5.1: Material details including dimensions, hydrogen concentrations, and test temperatures.

Materials	Test Parameters			Average (wppm H)	Uncertainty/st.dv. (wppm H)	Test Dissolution Temperature °C	Test Temperature Range °C
	l_o(N)	r (N/mm)	ext_{lim} (µm)				
LK3	50	150	80	98	5	350	220-265
LK3	50	150	80	200*	-	450	220-360
LK3	50	100**/150***	120	328	20	500	160-410
LK3/L	90	100	80	139	7	380	220-340
LK3/L	100	60	120	380	40	500	160-410
SINQ Target Rod	150	60	120	401	50	550	270-330

* no HVE possible, ** 'slow load reduction', *** 'fast load reduction'

74

5.3.   Measurement technique

From fractographic results, the average crack propagation was measured for the DHC region. The distance of propagation was divided be the total time of cracking, i.e. the thermomechanical loading segment. The uncertainty was propagated through the standard deviation of the DHC crack length measurements as well as the ramp-up time to the starting load of the thermomechanical segment. The ramp-up time was used for the uncertainty of time because DHC may have started during this segment prior to taking the test time.

5.4.   Results

The following subchapters present the observations and measurements of DHC crack lengths and velocities. The fractographic and metallographic results are described in chapter 7 with respective neutron radiographs.

5.4.1.   Crack length

In Figure 5.1, the average crack lengths trend within each set, show a decreasing length with increasing temperature. It should be noted that the final extensometer limits varied between the alloys and sometimes between test sets of the same alloy. Therefore, the testing parameters make it complicated to compare the total length between sets. However, the trend within each set is clear, where the crack length decreases as the test temperature increases. As the compliance of the test fixture and device is accounted for by using the extensometer, it can be assured that a systematic error from a test temperature effect, i.e. variation in compliance with temperature, can be dismissed. Therefore, it is expected that between the lowest temperatures and 300°C the effect of the changing yield stress likely affect the sample displacement. Above 300°C it can be seen in metallography (chapter 7) that, in addition to the change in yield strength, creep becomes a significant factor leading to creep-induced crack

tip blunting. The result of creep is a combined sample displacement due to plasticity and DHC, rather than solely DHC propagation. This is apparent in Figure 5.1, where the crack length at high temperature are significantly shorter for the same extensometer displacement limits.
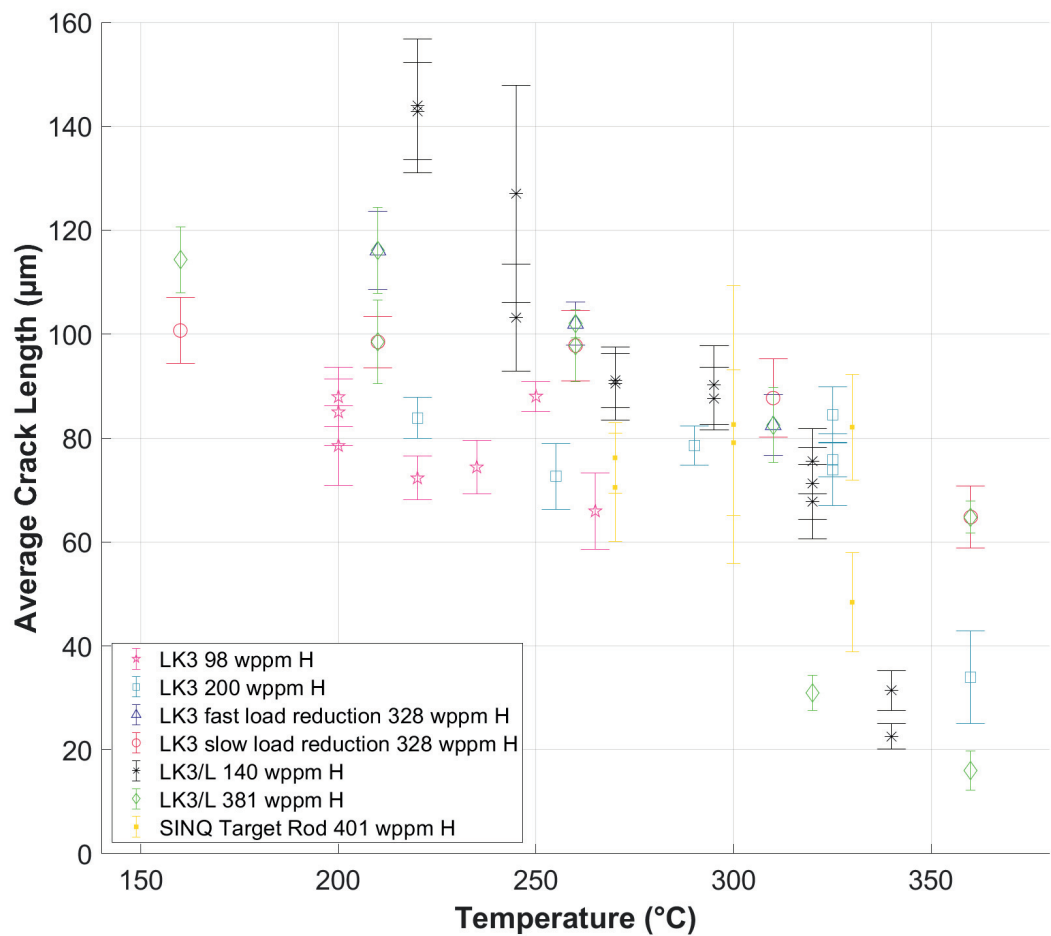
Figure 5.1: Summary of the average crack lengths, which were used to calculate the DHC velocity, found in Figure 5.2.

5.4.2.   Crack velocity

In Figure 5.2, a strong trend of crack velocities can be found were the velocity follows the Arrhenius law up to 300°C, thereafter the velocity quickly decreases. When comparing the

velocities of the different sample sets, the SINQ target rod material generally cracks faster. While there are limited data points for the SINQ target rod material, the comparison between other Zircaloy-2 materials should be considered loosely based. Of the LK3 samples, the test parameters remain mostly consistent, with the exception of the load reduction for a small number of samples. With the load reduction parameters considered, in general the velocities are very similar following the Arrhenius law up to 300°C. However, two samples of the 98 wppm H set showed a decrease in velocity from 250°C and higher. At temperatures higher than 300°C there was a larger scatter of results in general as creep becomes a prominent factor. The LK3/L material also follows the Arrhenius law for velocity up to 300°C. Again, after 300°C the velocity slows for the LK3/L material. In general, the LK3/L material follows the same trend as the LK3 material. However, when closely analyzed, as the logarithmic scale can be deceiving, the velocities of the LK3/L material are significantly lower, up to 2-3 times slower than that of the LK3 material below 300°C. Above 300°C the LK3/L material appears up to one magnitude slower, however, there are limited direct comparison points along with high scatter.
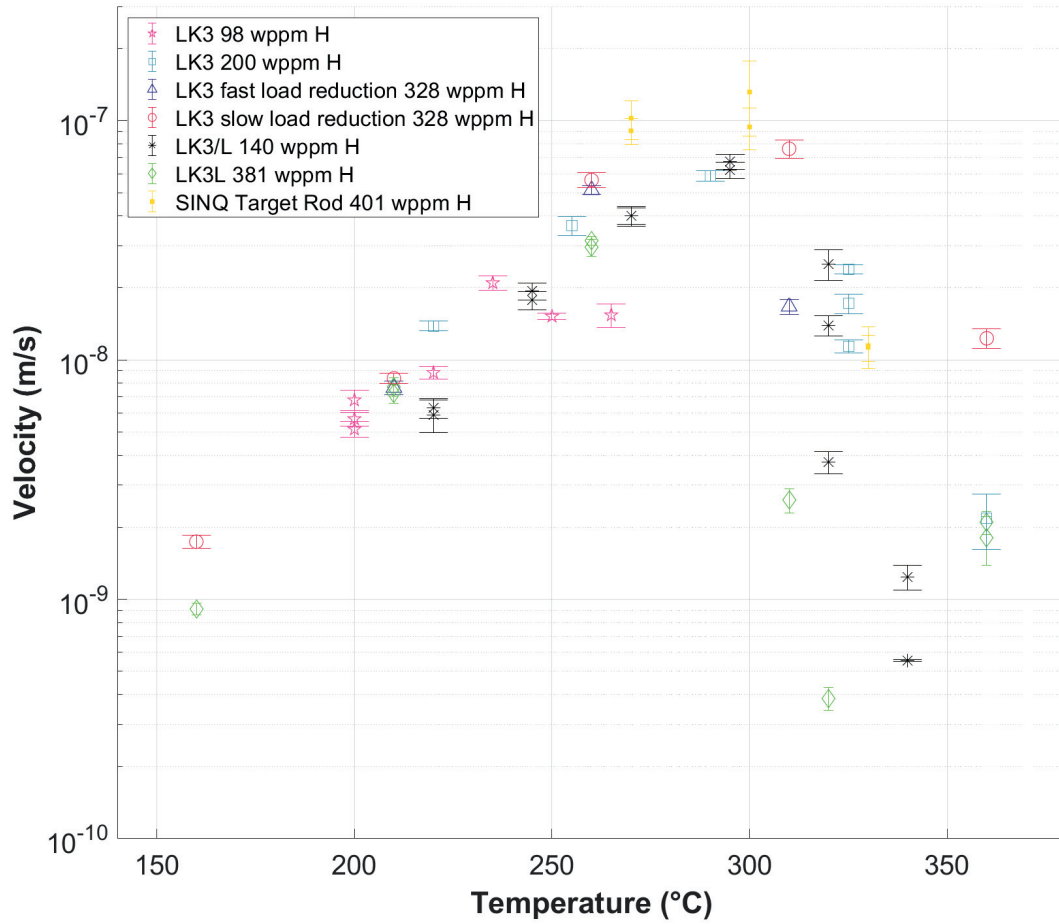
Figure 5.2: A summary of the velocity tests conducted. Sample materials include LK3, LK3/L, and SINQ target rod material including a spectrum of hydrogen concentrations.

5.4.3. Activation Energy

The Arrhenius relationship is described in Equation 5.2. This relationship shows the dependence of the rate constant, k, of a chemical reaction with respect to the absolute temperature, T.

Equation 5.2

$$k = Ae^{\frac{-E_a}{RT}}$$

78

where A, is a pre-exponential factor, E_a, is the activation energy, and R is the universal gas constant.

Taking the natural log of Equation 5.2 provides a way to solve for E_a. The resulting Equation 5.3 can be related to the linear progression of the rate constant, in this case DHC velocities, v.

Equation 5.3

$$\ln v = \ln A - \frac{E_a}{RT}$$

The activation energy can then be fit for various sets of experiments, i.e. the various sets of LK3 and LK3/L differentiated by their hydrogen concentration. Specific data points from Figure 5.2 have been selected for curve fitting. Criteria simply included temperatures below 300°C and sufficient points to fit. After fitting the selected points, E_a can be determined. In the values are summarized.

Table 5.2: Summary of activations energies.

Sample Set	E_a (kj/mol)
LK3 328 wppm H	67.2
LK3/L 140 wppm H	73.6
LK3/L 381 wppm H	66.7
Literature summary [67]	43-68

5.5.   Discussion

Although the dependence of DHC velocities on temperature of all alloys below 300°C seem to be very similar, the LK3/L liner material consistently exhibits slower crack velocities throughout the temperature range. Considering the reduced hydrogen in the matrix of the LK3/L material, it appears that the smaller source of dissolved hydrogen in the matrix reduces the total hydrogen diffusion rate and limits the DHC cracking velocity. The cracks in the SINQ target material appear to propagate slightly faster than the other cladding materials. However, there are no direct comparisons available at temperatures and hydrogen concentrations. Considering the various samples sets collectively, there is an apparent Arrhenius relationship of velocity for samples cracked below 300°C. For three of the sample sets, which had sufficient data points for curve fitting, the activation energy was determined. The values show very good relationship with literature however are insufficient in data to compare the differences between sets.

In Figure 5.2, the maximum velocity appears to occur between 260 and 310°C. While this is a large temperature range, it is in agreement with values seen in literature using different testing approaches [67]. Additionally, the load reduction (r of Equation 5.1) of the LK3 material appears not to play a large role at lower temperatures which is also in agreement with literature [57]. However, at 310°C the two unloading schemes result in a variation in the crack velocity measured. It could be postulated that creep begins to play a role in sample deformation resulting in a variation of the total test time. Assuming creep is the underlying factor, the slower (smaller r) load reduction leads to faster deformation and therefore an artificially faster calculated crack velocity between the LK3 samples at 310°C. The results also show that the samples at 360°C cracked at an equal rate or faster than many samples at 310°C. This may be because the velocity measurements were most sensitive to the testing time than the crack length. This is evident through the short crack length of the samples at 360°C shown in Figure 5.1, which should have theoretically further reduced the velocity. However, the increased rate

in deformation due to creep, was the main reason in the test reaching the extensometer limit faster thus reducing testing time, giving the illusion that DHC propagated farther.

While the samples are all very comparable, it should be noted that scatter is likely introduced through the variation of test parameters between alloys, including the 'starter', pre-crack length, initial loading, and pre-defined final displacement limits. The results of the initial crack length and loading can lead to a variation in K_I, which theoretically should not affect the velocity, but inevitably can by changing the stress field and in turn the hydrogen diffusion. Additionally, if K_I, exceeds stage 2 of crack propagation, the velocity will inherently accelerate, increasing the deviation of the average velocity. In this work, the uncertainty due to loading parameters has not been quantified and assumed that DHC propagation remains within stage 2 of crack propagation.

Lastly, the velocity has been reported as a function of 0.2% offset yield stress in [67], which can be seen in the respective velocity trends as the temperature increases from a minimum to a point when creep becomes a prominent factor. It is unclear whether the effective offset yield stress could be used for the integral specimen or the local material properties, i.e. at the crack tip. In the case where integral specimen properties are considered, the velocity will be greatly affected by the softer inner liner, and the amount of hydride precipitation throughout the matrix. It should be noted there is significantly more hydrogen, and thus hydrides in the SINQ target rod material compared to the other Zircaloy-2 materials that would increase the integral yield strength. While there are limited data points, this could be one possibility for higher cracking velocity in the SINQ target rod material.

5.6.   Conclusion

The velocity of radial DHC in cladding tubes has been investigated over a spectrum of temperatures and hydrogen concentrations using three types of Zircaloy-2 cladding. The results show the strong influence of the liner in reducing the DHC crack velocity, which is likely

due to the reduction in available hydrogen for diffusion because a fraction of hydrogen is trapped in the liner). In general, the velocities of all materials followed the Arrhenius law up to 300°C. Above 300°C, the effects of creep begin to affect the velocity. It has been postulated that the potential effect of high amounts of hydrides in the SINQ target material increased the integral yield strength, due the brittle nature of the hydride, and therefore influenced the cracking velocity.

6. Threshold stress intensity factor tests

This chapter describes the investigation of the threshold stress intensity factor for delayed hydride cracking based on temperature and hydrogen concentration on LK3 (without an inner liner) material only. In the first subchapter, the specific parameters of the tests are given as introduced in chapter 4. In the second subchapter, the test results and analysis techniques are described including details supplementary to the threshold stress intensity factor investigation. Following the experimental results, FEM models are described including the validation process of the general boundary conditions. Finally, the conclusions about the resulting threshold stress intensity factors are reported.

6.1.   Motivation

From a risk assessment point of view, more important than all other parameters is the threshold for the onset of DHC, the threshold stress intensity factor, K_{IH}. Without adequate stress to initiate DHC propagation, all other conditions for DHC are insufficient [119]. Because of the importance of K_{IH}, several studies specifically on the K_{IH} have been performed, however with some deficiencies and significant assumptions in testing methods and conditions that have been suggested, for instance, by IAEA as future test improvements [109]. Some of these include assumptions about the similarity of axial and radial crack propagation direction [66], [109]. Furthermore, some literature has reported values which are based on experiments with step-wise or discontinuous unloading to arrive upon final loading to an increased uncertainty [66]. Lastly, the geometric effects of thin walled fuel cladding on DHC are not captured within the more common pressure tube tests [74].

Nevertheless, there are important points from previous studies on K_{IH}. They include a slight overall decrease in K_{IH} and increase the threshold temperature of DHC with irradiation damage [66], [69]. Additionally, it has been shown that the effect of creep on crack tip blunting is a

primary factor in the upper threshold temperature limit. As the crack tip blunts with creep at elevated temperatures, the stress concentration will be reduced and therefore reduce the effective stress intensity K_I. Because of creep-induced blunting, the K_{IH} could be misinterpreted when considering the crack length without blunting. The effective K_I might actually be higher when considering blunting of the crack tip and the effective crack length [86]. The kinetics of hydrogen precipitation should also be considered when determining the threshold temperature. As the temperature exceeds that of the TSSp for the integral hydrogen concentration, the driving force or total diffusion maybe greater to achieve a local concentration high enough to cause precipitation.

The main motivation of experiments in this chapter was to explore DHC K_{IH} testing where previous studies had required assumptions in cracking direction and orientation, or lacked geometrical context. FEM is implemented to uniquely model each sample and respective crack front to back-calculate K_{IH} values. Particular interest is put on the exploration of a minimum K_{IH} within a range of temperatures where the kinetics of diffusion and precipitation may be optimized for DHC.

6.2.   Test parameters

The sample preparation regarding hydrogen charging, homogenization and final specimen cutting follows the procedure described in chapter 3. As described in chapter 4, each sample underwent fatigue pre-cracking, heat-up above the respective hydrogen dissolution temperature, and cool down to the defined test temperature. However, the tests described in this chapter utilized a unique loading scheme in which a propagating crack would be arrested. A temperature and load process overview can be found in Figure 6.1.
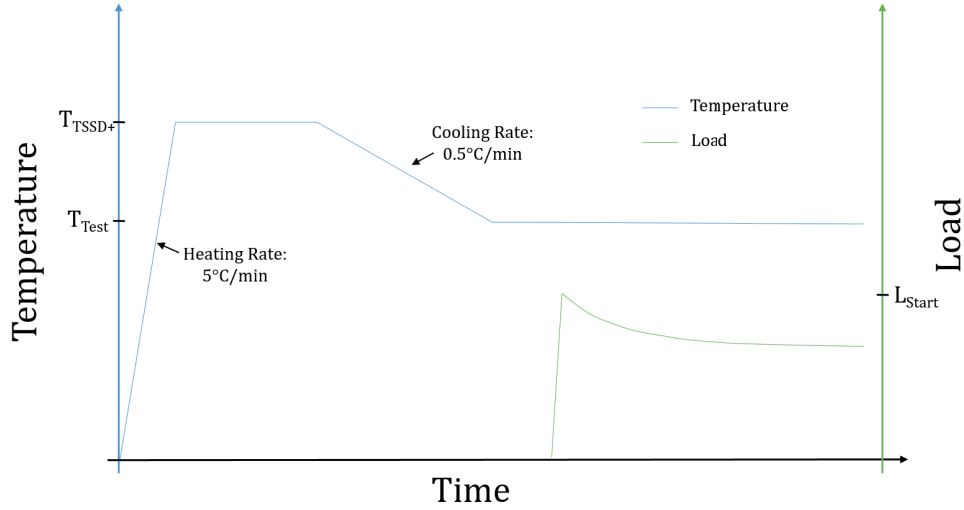
Figure 6.1: Temperature and load curves of DHC testing segment with respect to time.

6.2.1.   Loading parameters

As previously described in chapter 4 the loading was defined based on the measured extensometer displacement. Again, the following equation shows how the loading was defined:

$$l_n = l_o - r \times d$$

where l_n, is the newly calculated load, l_o, is the initial load, r, is the reduction rate with units (N/mm), and d, is the extensometer displacement with units (mm). The initial values for l_o was 50 N, while r was either 180 or 300 N/mm. The initial loads ensured a sufficient K_I for DHC, which had been previously tested and confirmed, while the unloading rate values ensure that the force resulted in a reduced stress intensity factor. In this way, the load would converge to a final load leading to the respective K_{IH}. Two unloading rates were required as the initially chosen value of 300 N/mm for r was too large for high temperature tests where the K_{IH} was achieved with little DHC propagation. Therefore, a smaller value of 180 N/mm was chosen for certain tests to ensure a pure DHC arrest in which the DHC crack had sufficiently propagated

away from the pre-crack. After DHC testing, the samples were water quenched and completely fractured.

6.2.2. Temperature parameters

The temperatures for hydrogen dissolution and testing can be found in Table 6.1

Set # (average wppm H)	Test Dissolution Temperature (°C)	Test Temperature Range °C
1(155)	370	210-290
2 (305)	480	210-330

6.3. Test results

The test trends of load and displacement curves during DHC propagation are described along with the fractographic and metallographic analyses. A summary of the final loads and total crack growth is also provided.

6.3.1. DHC testing results

In Figure 6.2 and Figure 6.3, a number of samples have been selected to show the extensometer displacement and the load progression versus time, respectively. The displacement change indicates the increasing sample compliance, i.e. a reduction of the load bearing cross section of the sample, and thus crack propagation. Each of the 155 wppm H samples present a small incubation period, defined as an initial phase of slow growth, in the first thousands of seconds prior to primary deformation, which represents the second phase of growth with a significantly increased displacement rate. After some time the displacement reaches saturation where DHC can no longer occur due to insufficient loading. In this work, the saturation of displacement is defined as DHC crack arrest. When comparing the primary

displacement phase, a temperature dependent deformation rate trend is most apparent when the slopes of the curves are compared. At lower temperatures the extensometer displacement represents a slower crack growth, as seen in the slope of the displacement as well as the longer time required to reach the maximum displacement. At the mid-range test temperatures (230-270°C), there is an increase in primary displacement rate, which can be seen in the decreased time required to reach near-maximum displacement. Interestingly, as the primary displacement rate increases with temperature, the incubation period prior to the primary growth of the crack becomes shorter and the transition between the two becomes more noticeable due to the difference in slope.

The 305 wppm H sample set showed similar behavior compared to the 155 wppm H sample set in incubation time and total time of primary crack growth. Figure 6.4 shows explicitly that the extensometer displacement rates, also interpreted as crack propagation rates, increase with temperature while the incubation time decreases with increasing test temperatures (up to 290°C). However, at the highest temperatures, the samples appear to skip any incubation period and reach the respective K_{IH} much sooner. At this temperature, a clear creep effect can be expected.

Figure 6.2: Selected experimental data of 155 wppm H set showing the extensometer displacement (indicator for crack propagation) as a function of time. A nested zoom of the dashed in gray region of interest (ROI) showing the first 6000 seconds. The unloading rate for the set was 0.3N/µm. Note: entire test length is not shown for scaling purposes of DHC growth.
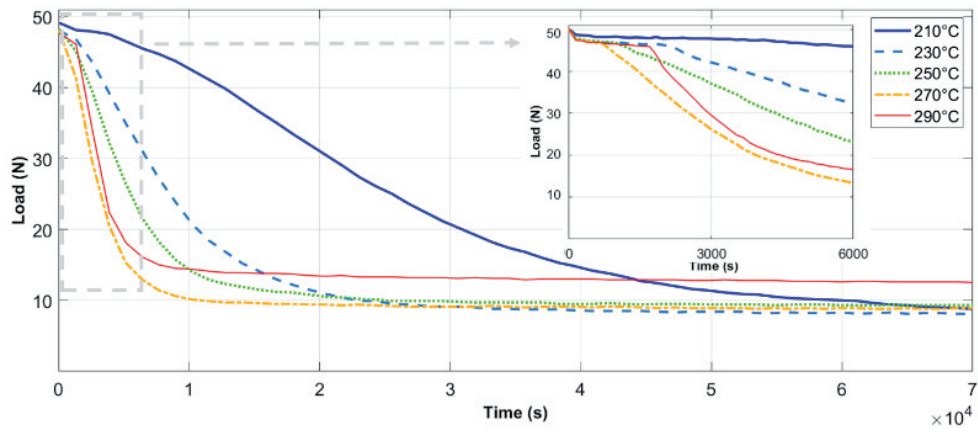
Figure 6.3: Selected experimental data of the 155 wppm H set showing the sample load reduction versus time. A nested zoom of the ROI showing the first 6000 seconds. The unloading rate for the set was 0.3N/µm. Note: entire test length is not shown for scaling purposes of DHC growth.
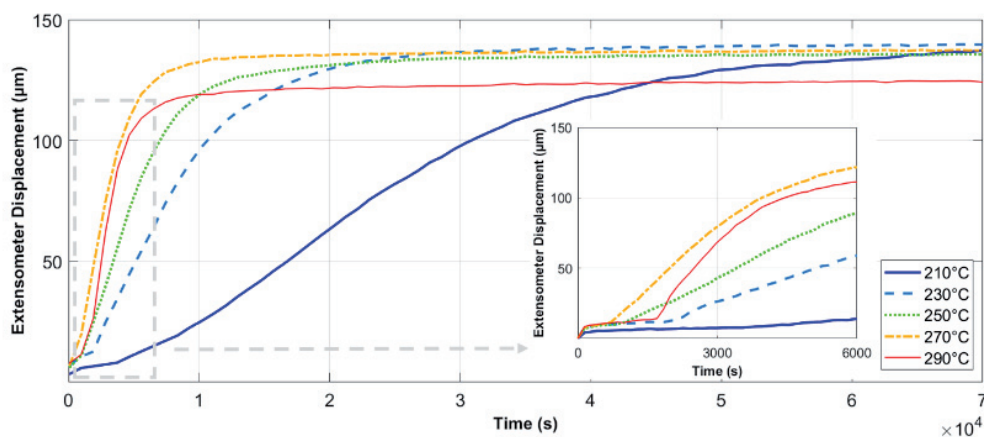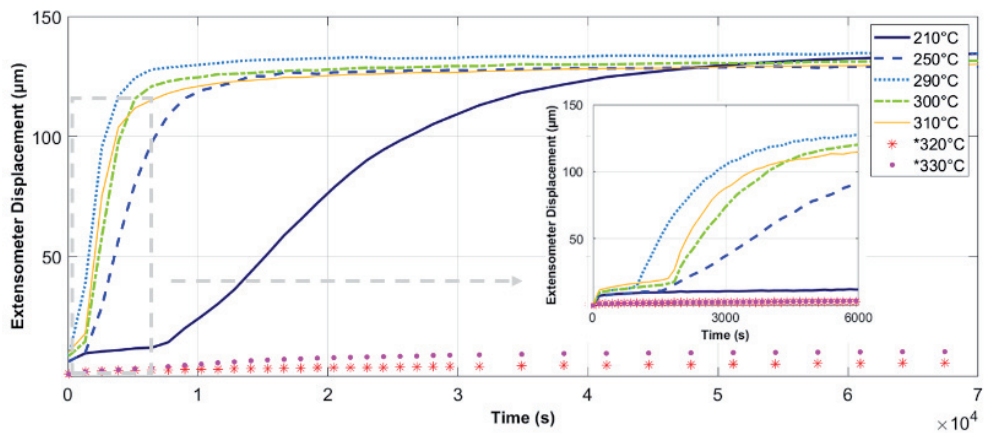

Figure 6.4: Selected experimental data of 305 wppm H set showing the extensometer displacement (indicator for crack propagation) as a function of time. A nested zoom of the ROI showing the first 6000 seconds. The unloading rate for the set was 0.3N/µm. Exceptional loading (0.18N/µm) is indicated with a star*. Note: entire test length is not shown for scaling purposes of DHC growth.
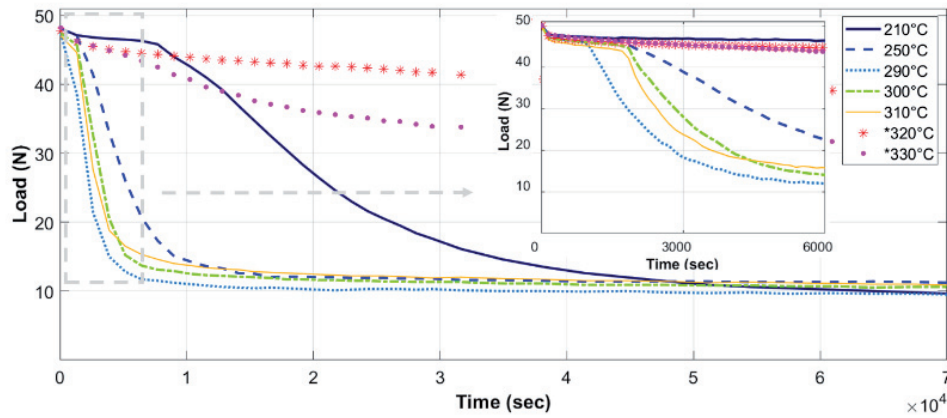
Figure 6.5: Selected experimental data of the 305 wppm H set showing the sample load reduction versus time. A nested zoom of the ROI showing the first 6000 seconds. The unloading rate for the set was 0.3N/μm. Exceptional loading (0.18N/μm) is indicated with a star*.Note: entire test length is not shown for scaling purposes of DHC growth.

In Figure 6.6 and Figure 6.7, the evolution of the crack propagation throughout the various testing steps can be observed for both sample sets. Starting from the notched region, the crack propagates first via fatigue pre-cracking and then transitions to the DHC zone. The color of the fatigue zones is very similar between each of the samples, respective of the hydrogen concentration, because of the oxidation during the heat-up phase for the given set, i.e. 370°C for the 155 wppm H set, and 480°C for the 305 wppm H set. The DHC zone in each sample is tinted differently because of the zirconium hydrides being oxidized at different temperatures, i.e. at the given test temperature when it is first exposed to the surrounding air environment.

The primary focus of fractography was to measure the average depth of the crack front through nine equidistant points along the front. The resulting measurements can be seen in Figure 6.8. The dimensions are then directly implemented with final loads (Figure 6.9) into a FEM model where the stress intensity factor is back calculated.

Additionally, it is observed that the crack propagates less with higher test temperatures, indicating an earlier crack arrest. The earlier crack arrest implies that the inherent K_{IH} is different, and was reached earlier in the test. The shallower crack depth can also be inferred

89

from the total displacement of the extensometer, which is assumed representative of the total

crack propagation.
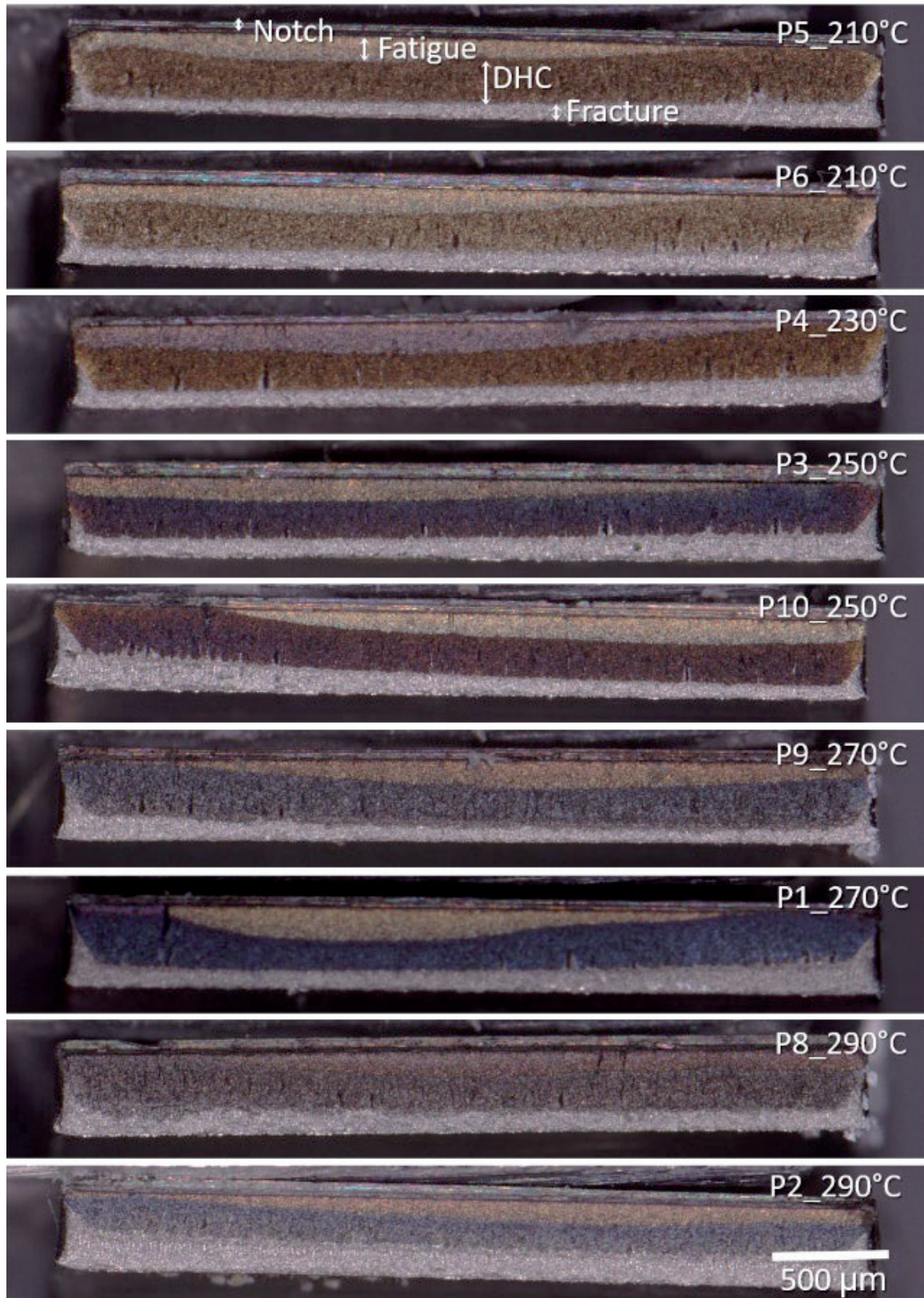
Figure 6.6: Fractographic overview of the sample set containing 155 wppm H. The displayed 'P' number represents the sample number while temperature corresponds to the DHC test temperature.
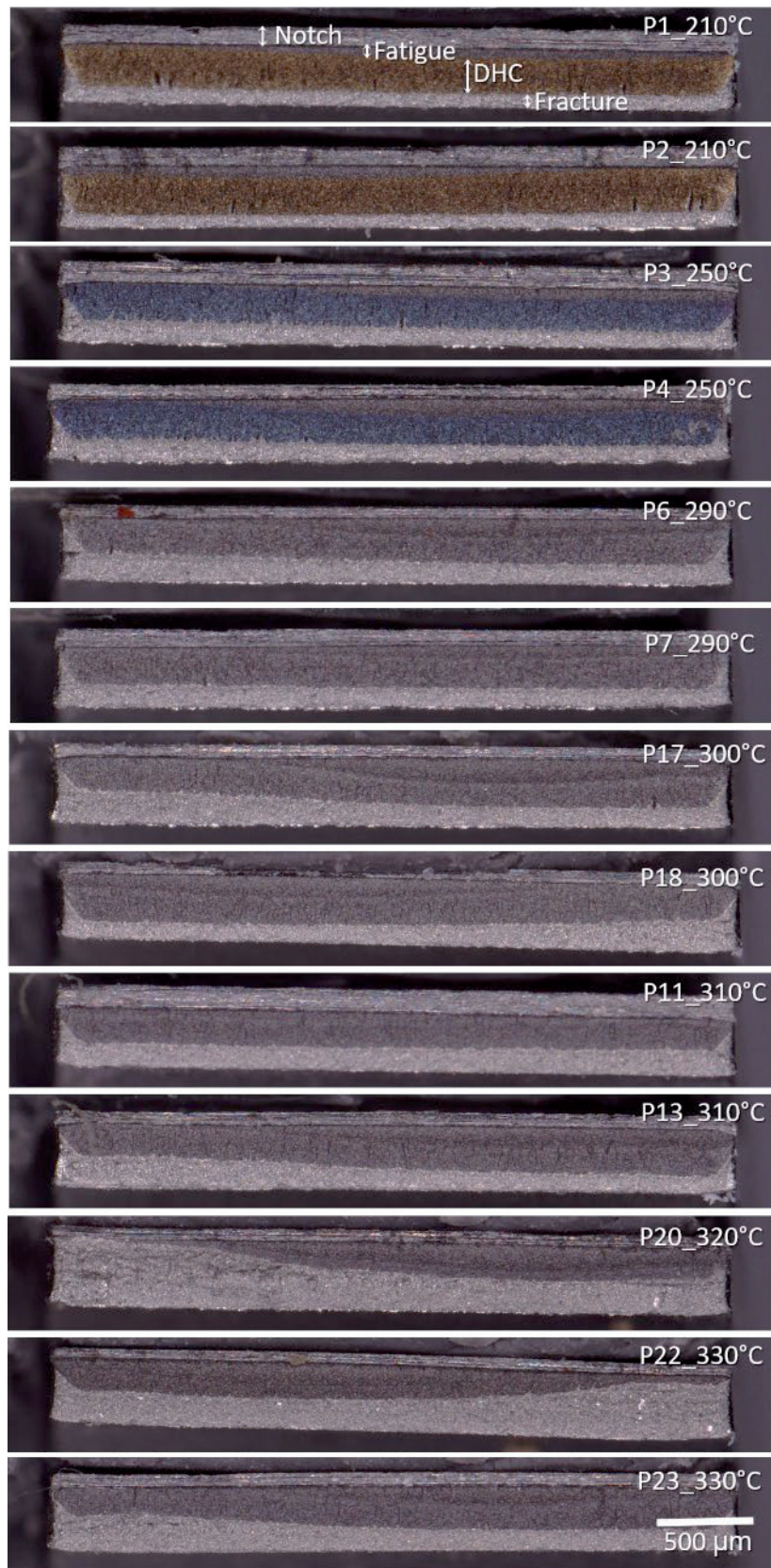
Figure 6.7: Fractographic overview of the sample set containing 305 wppm H. The displayed 'P' number represents the sample number while temperature corresponds to the DHC test temperature.
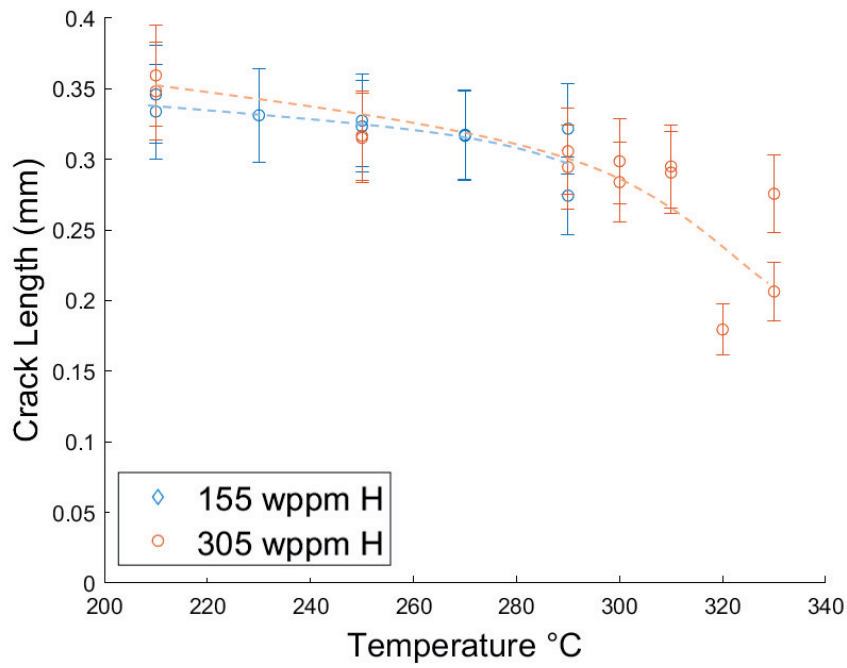
Figure 6.8: Average crack length from fractography as function of DHC test temperature. The standard deviation was not more than 10% and captures the total uncertainty. The dotted lines are only intended for guiding the eye and are not fit with a function.
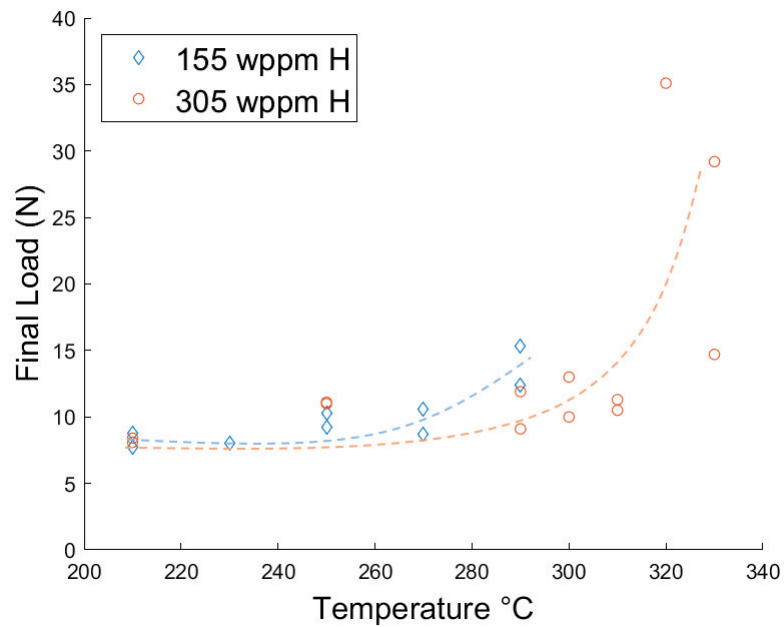
Figure 6.9: Chart detailing the final load with respect to DHC test temperature. The uncertainty for each data point is ±0.1N and not implemented in the graph for visual reasons. The dotted lines are only intended for guiding the eye and are not fit with a function.

6.3.2.   Metallography

In addition to the sample shown in the previous subchapters, further tests were performed at higher temperatures. The samples in Figure 6.10 were originally used for velocity tests with a lower unloading rate. It should be mentioned that while the test spectrum for K_{IH} does not extend to the very high test temperatures shown in Figure 6.10, DHC is clearly possible at high temperatures. The metallography images intend to highlight the effect of creep on the crack tip radius, leading to blunting. While blunting before the DHC crack initiation (failure of the first hydride in front of the fatigue crack tip) can already be seen at 310°C and 360°C, creep can be observed most significantly at 410°C, where no DHC has occurred. As DHC is clear at high temperatures, these K_{IH} tests could be extended above 360°C with the knowledge that the measured K_I is an integral phenomenon of creep and DHC, which cannot be decoupled. In this project, a new term has been defined, describing this phenomenon as creep delayed hydride cracking (C-DHC).
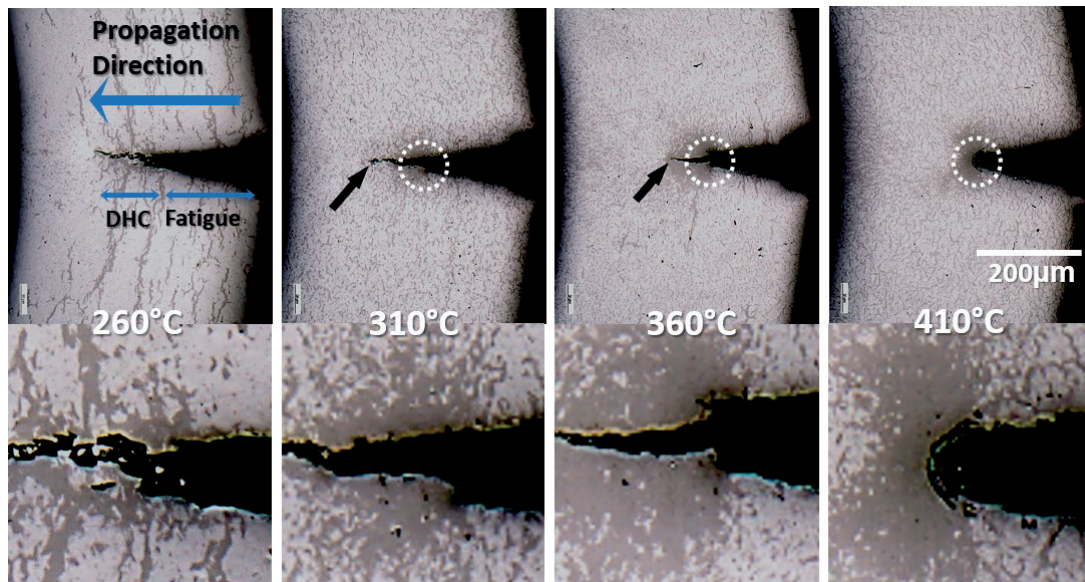
Figure 6.10: Samples tested for crack velocity tests showing the development of creep-induced blunting. The test temperature is indicated in each of the images. The dotted white circle indicates the DHC initiation and blunting which occurred at DHC onset. The black arrow indicates the point of crack arrest. The material tested was Zircaloy-2 (LK3) containing 300 wppm H.

6.4.   FEM

With Ansys, finite element analysis was used for the back-calculation of the stress intensity factor upon fracture arrest. Convergence studies were performed in order to optimize mesh sizes for crack fronts and contact points. General boundary conditions of the model were validated through a comparison with standards [120], [121], where the FEM model calculated a K_I within 1% of the standards when using the standard dimensions as shown in Figure 6.11. The model was then adapted to the experiment by changing only the dimensions. The model seen in Figure 6.12 represents the three-point fixture and sample with a given crack front. The bottom surface of the two lower 'rollers' are supported with a fixed displacement. The load was defined from the given experiment and was applied to the upper surface of the upper 'roller'. The contact definitions were tested and varied from frictionless, frictional (friction coefficients of 0.1, 0.2, and 0.3), and bonded. The stress intensity factor was most realistic with the frictional definition. The results from the varied friction coefficients showed less than a 0.1% difference in the resulting stress intensity factor. The frictionless resulted in slipping to one side, while the bonded definition restricted the bending of the sample, which led to an unrealistically small stress intensity factor. For these reasons contacts were defined with a frictional coefficient of 0.2 for reasons described above as well as in literature [67]. The sensitivities of the FE model were meshing density and contact definitions. Both variables have been tested in order to converge on an accurate calculation. The model was first optimized with a mesh density that had converged on a solution.

The fracture was modeled with a rectangular plane surface resulting in a flat crack front, which penetrated the cladding to a specified depth and corresponded to the average crack depth of the given experiment. This technique is known as an "arbitrary crack" within the Ansys workbench. The model results in a geometry with a sharp crack tip which is realistic for LEFM with small plastic zones. The geometry does not incorporate dimensions of a notch as it is completely irrelevant for the stress distribution at the crack tip, which is far from the notch.

More specifically, the model is ideal for cracks at lower temperatures where creep does not cause significant blunting. Therefore, it should be noted that tests at higher temperatures which resulted in blunted crack tips cannot be directly modeled. Blunting of the crack tip results in an extended effective crack tip caused by plasticity [86], [122] and can be assumed to extend the K_I in the positive direction proportional to the amount of blunting. In this study, the extension is not calculated but assumed to strongly affect models representing tests above 300°C.

The loads used in the FEM models correspond to the loads during the various 3-point bending experiments. In Figure 6.9, the trend shows that the final load on the sample at crack arrest increases slowly with an increase in test temperature until a given transition point where the final load increases quickly. The transition point for the two sample sets occurs at different temperatures where the 155 wppm H sample set occurs earlier than the 305 wppm H. Given the scatter of the data and limited number of samples, the transition of the 155 wppm H sample set is around 270°C, while the 305 wppm H sample set transition occurs around 290°C.

It can be assumed that the starting stress intensity factor is also similar and consistent within both sample sets. This is justified as the pre-cracking phase in each sample is rather consistent, leading to a consistent pre-crack depth, and the starting mechanical load is always the same.

6.4.1.   Model validation with standards

The model in Figure 6.11 is dimensioned such that it could be validated with the standards commonly used for three-point bending [120], [121]. Once the FEM results were validated (Table 6.2), the dimensions were adapted to the main experiment. Specifically, the span was increased, sample curvature was implemented, and the 'thickness,' B, was increased.
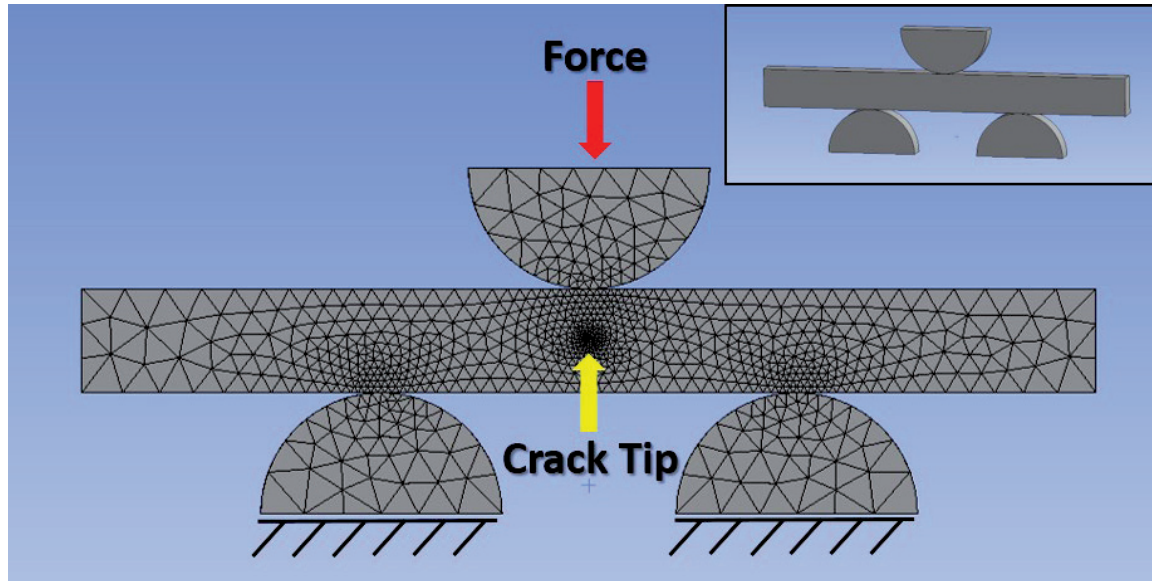
Figure 6.11: FEM model used in the verification of general boundary conditions. The dimensions were in compliance with the standards references in the text.

Table 6.2: Validation with given standards.

K_I (MPa√m)		
Bower	ASTM D5045-14 E1290-08	FEM
23.47	23.89	23.68

6.4.2.　　　Three-point bend model
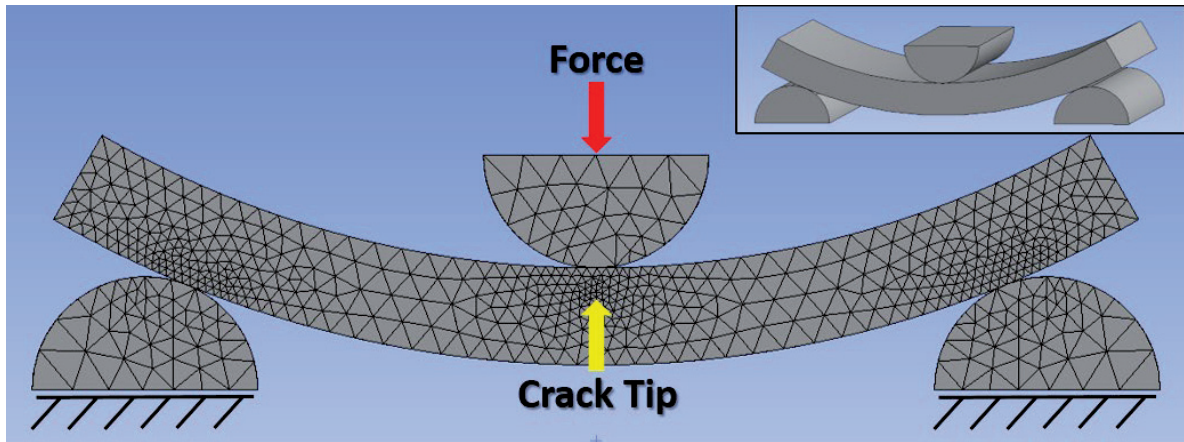
Figure 6.12: Mesh of the model describing the crack tip location and the boundary conditions. In the upper right is the projected view of the 3D model.

While it is obvious that the crack fronts are slightly curved as in typical semi-elliptical crack front shape, calculations of K_{IH} with FEM utilize just an average crack depth. This is a simplification when considering the crack front shapes as illustrated in Figure 6.6 and Figure 6.7. Nonetheless, this viable procedure eventually leads to conservative results, because the average crack depth is shorter than at the locations with highest depths. A shorter crack under a given stress leads to lower, rather conservative K_I. Additionally, the number of uncertainties rises when modeling the exact crack front shape (as seen in Figure 6.13), with the number of dimensions that need to be measured. In other words, the measurement of the ellipse radii, along with depth and offset incorporate three more uncertainties in the model, compared to just the average crack depth, creating large sensitivities in the K_I profile. Such uncertainties can lead to measurements that are either drastically over- or under-estimated. Therefore, the average crack length is chosen for this project.

Due to the thin walled sample geometry and materials properties, the loading results in a FEM-calculated stress distribution that varies axially. For instance, at the free surfaces in axial direction, the stress is zero (Figure 6.13), inwards the sample it quickly increases, and in the middle, it slightly relaxes. It is the same for the stress intensity factor. It was decided to use

the highest calculated stress intensity for the threshold stress intensity factor. Its location in the sample corresponds with that of largest DHC depth. One could argue that lower K_I-values, e.g. from the middle of the sample, should be used. However, we take into account that the DHC crack does not develop evenly, and can occur at different times in different locations, so that the DHC stops earlier in the middle than at the locations where the DHC crack has the largest extent. A stress intensity factor for the part of the crack which does not propagate anymore would be meaningless.
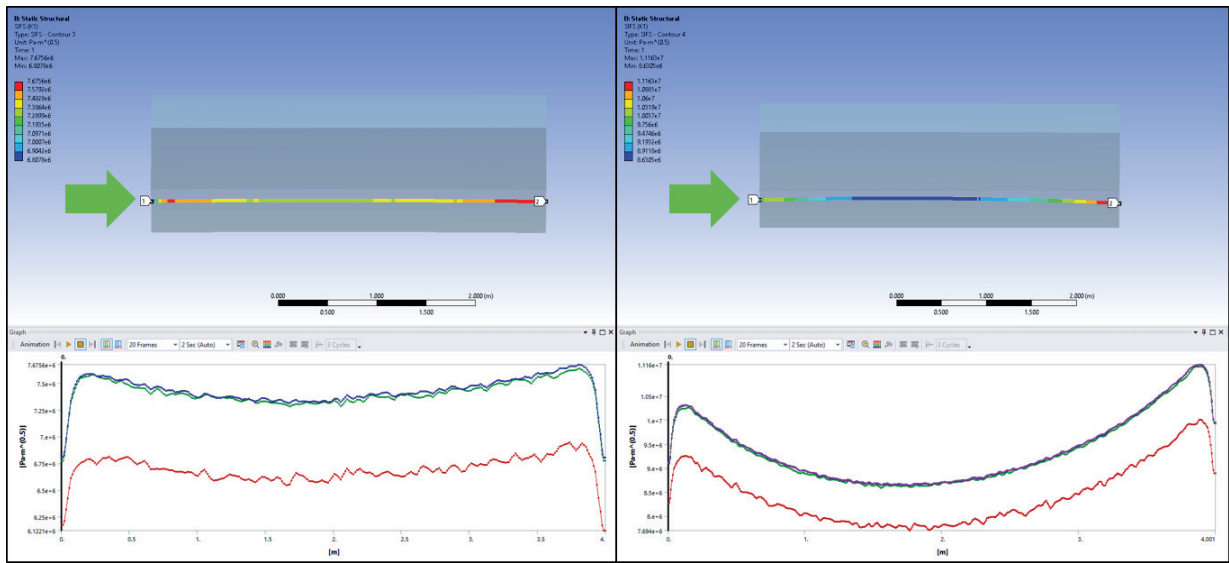
Figure 6.13: The figure describes two sample models with a flat (left) crack front and semi-elliptical (right) crack front shape.

6.4.3. FEM results

A comparison of the two sample sets can be found in Figure 6.14. The plot shows a minimum value for K_{IH} around 6 MPa√m for both sets at the midpoint of the respective test spectrum, and an increase in K_{IH} with temperature until creep inhibits modeling of high temperature tests (above 300°C). In Figure 6.14, arrows indicate that creep plays a significant role on K_{IH} after 300°C as has been reported in literature [66]. Therefore, it can be assumed that for samples above 300°C, the effective crack length is longer due to the crack tip plasticity. However, FEM calculations use the as-measured length from fractography rather than an effective crack

length leading to conservative K_I values. The creep-effect is expected to increase K_{IH} as it causes an increase in the effective crack length. The models had shown the calculated K_I had extreme sensitivity to the increase in crack growth at high a/W (crack length/sample width according to ASTM [80]) ratios compared to the load sensitivity. Therefore, the uncertainty could be larger for calculations representing lower temperatures tests where the crack length is largest.
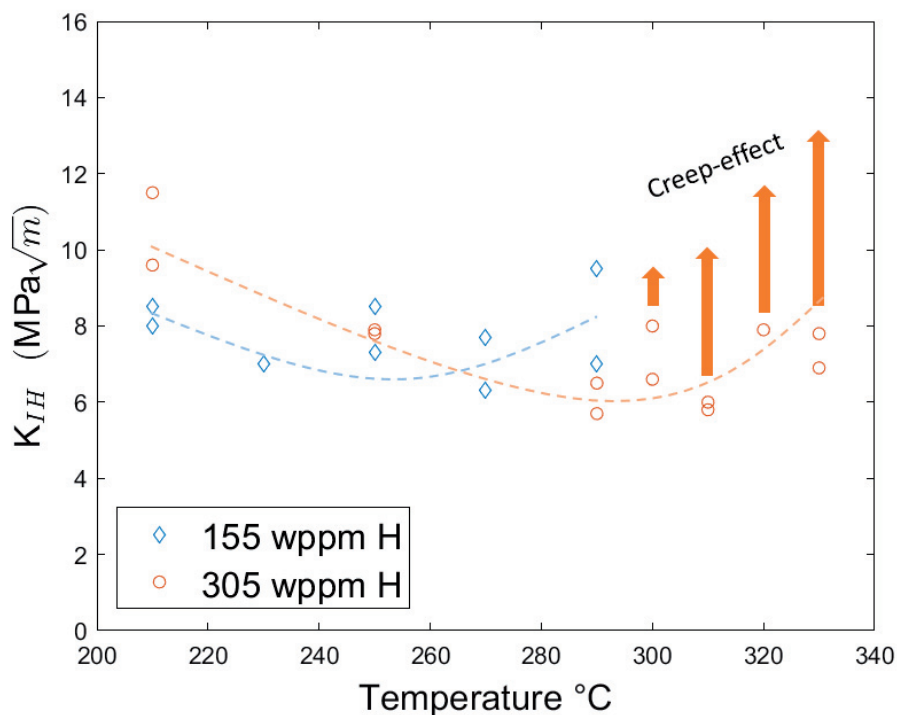
Figure 6.14: An overview of the FEM back-calculated K_{IH} for both 155 and 305 wppm H sample sets. The dotted lines are intended for guiding the eye. The arrows are set to show the expected K_{IH} if the effective crack length was considered.

6.5. Analysis and discussion

The following subchapters discuss the test trends seen in load and displacement curves, the fractography and metallography results, and lastly the resulting K_{IH} values from FEM.

6.5.1.   Test trends

From the displacement trends observed in the Figure 6.2 and Figure 6.4, one can infer that although incubation times differ, the crack velocity of the set increases with increasing test temperature, excluding 320° and 330°C tests. At first glance, it seems counter-intuitive that velocity would continuously increase as the resulting K_{IH} also begins to increase. However, the threshold when DHC starts and the initial crack velocity are different things. For K_{IH}, also the local stress plays a role. Further, there is less hydrogen in solid solution at lower temperatures and, thus, the total diffusion is slower and requires more time to precipitate a critically sized hydride. Alternatively, as the temperature increases, the amount of hydrogen in solid solution is greater, i.e. an increase source of hydrogen for DHC, requiring less time for sufficient hydrogen diffusion to create a critically sized hydride. The incubation times prior to primary DHC propagation also generally depend on temperature. In the 305 wppm H set, the effect is consistent displaying shorter incubation times prior to cracking as the test temperature increases. This dependence can also be roughly seen in the 155 wppm H set.

In addition to cracking, creep begins to supplement the measured extensometer displacement, giving the illusion that the crack is very fast at high temperatures.

6.5.2.   Fractography and metallography

The profile of the crack front evolves as the crack progresses implying that the stress intensity factor is also evolving. The flattening of the DHC crack front profile, in comparison to the fatigue crack front profile, shows that the stress intensity is higher away from the centerline. This is explicitly seen when comparing samples that have propagated the farthest and the least. For example, in the 305 wppm H set, the samples tested at 210°C have a much flatter crack front compared to that of the 330°C samples because the 210°C samples have propagated farther where the K_I remained sufficient for DHC growth.

Based on the metallography, this work considers DHC plausible at high temperatures including 360°C and possibly higher. In addition, this work considers creep to begin playing a significant role on DHC after 300°C as depicted in Figure 6.10.

6.5.3.   Threshold stress intensity factor

In Figure 6.14, the minimum K_{IH} appears to be around 6 MPa√m for both sets when ignoring any crack tip blunting. This value is consistent with those, which can be found in literature, e.g. [33] where the tests were performed on Zircaloy-2 in a comparable temperature range. The source of scatter in K_{IH} is likely the crack depth measurement uncertainty and FEM limitations. Specifically, the measurements from the edges of the sample (in crack propagation direction) could be erroneously defined by an extended surface caused by the final fracture, but would result in a systematic error for all samples equally. Another limitation which could not directly be accounted for was the creep-induced blunting of the crack tip at higher temperatures. As mentioned previously, the effective crack length was not considered and FEM could not model blunting, likely resulting in underestimated K_{IH} values above 300°C as indicated by arrows in Figure 6.14. Lastly, the concentrations from one sample to another is relatively consistent considering the HVE measurements, however, any slight variation in hydrogen concentration could affect the kinetics of diffusion and precipitation, especially when approaching the upper temperature limits of DHC. The altered diffusion and precipitation kinetics could have a significant impact on the K_{IH}.

It has been reported in the literature that the possible reasons for an increased K_{IH} at elevated temperatures could be the higher hydrogen solubility limits, as well as the reduction in zirconium's yield stress leading to creep-induced crack tip blunting, and in turn reducing the stress concentration [66], [69]. In this study, it is seen that DHC is also dependent on the hydrogen kinetics, i.e. the diffusion and precipitation of hydrogen. The increasing temperature has two DHC-related and opposing effects: at higher temperatures, diffusion increases while

precipitation limits are shifted to higher local concentrations. Based on this, it can be hypothesized that there is an optimal temperature for DHC, at which K_{IH} is minimized, for a given hydrogen concentration. This can be seen in the shift of the K_{IH} curves in Figure 6.14. It is also seen that at high temperatures creep plays a significant role. This means at high temperatures and high hydrogen concentrations there is an overlap of creep and hydrogen kinetics effects on DHC. Therefore, the increase of K_{IH} is more dependent on hydrogen kinetics for low hydrogen concentrations, while high hydrogen concentrations are dependent on a combination of creep and hydrogen kinetics.

This study shows that the transition from a minimum K_{IH}, occurs at a temperature around 270°C for 155 wppm H. It should also be noted that the temperature of TSSP is 264°C for 155 wppm H [123]. Thereafter, the hydrogen kinetics become less ideal for precipitation. For 305 wppm H, the K_{IH} transition appears to occur at 290°C, as hydrogen kinetics are still favorable. However, after 300°C creep begins to blunt the crack tip, strongly reducing the ability to concentrate stresses on the hydrides at the crack tip. Again noting the TSSP temperature is 369°C for 305 wppm H. Considering the strong effect of creep, it is unclear where ideal hydrogen kinetics would be if creep effects could be neglected.

6.6.   Conclusion

The effect of hydrogen concentration and temperature on K_{IH} for radial DHC has been investigated using novel 3-point bending tests with radial outside-in cracking with an axial orientation and FEM back-calculations. The test represents realistic cracking conditions, in which the minimum K_{IH} occurs at an optimal temperature for hydrogen kinetics. It has been shown that the conditions, which result in the highest rate of DHC in the sample sets of 155 and 305 wppm hydrogen, are around 270 and 290°C respectively where the K_{IH} is roughly 6 MPa√m. This value is in agreement with the range of K_{IH} for Zircaloy-2 that can be found in literature. A possible explanation for the higher temperature for optimal DHC with higher

hydrogen content is that there exists a broader range of a low precipitation potential caused by the overall higher integral hydrogen content and, at the higher temperatures, a greater amount of hydrogen diffusion. As the temperature reaches the respective temperature for TSSP, the local hydrogen concentration required to precipitate must correspond to, or exceed the integral concentration prior to precipitation. Significant tensile stress may be required to create enough hydrogen diffusion that the local concentration would reach such high levels relative to the integral concentration. Additionally, the effect of creep on DHC has been shown to be less prominent at lower concentrations where kinetics play a greater role, however to have a strong influence at high temperatures above 300°C. The trends reported may be important for the discussion about relevant conditions of and precautions required for spent fuel handling.

7. Neutron radiography, metallography, fractography

The following subchapters describe the motivation and methodology of high-resolution neutron imaging performed in this PhD project. Neutron radiographs are presented with the respective hydrogen quantification, metallography and fractography. Finally, a discussion of the diffusion and precipitation patterns are given with connection to the hydrogen quantification. This chapter includes direct quotations from the article, "Delayed hydride cracking in Zircaloy-2 with and without liner at various temperatures investigated by high-resolution neutron radiography," that was published during the time of this PhD project by Colldeweih et al. [124].

7.1.   Motivation

Non-destructive analysis methods such as neutron radiography have great benefits compared to standard destructive methods like metallography and fractography. Especially in the case of complicated features, or highly radioactive material, non-destructive methods are preferred. The following subchapters will show the complex features unveiled through radiography, which remain hidden in subsequent destructive methods. The radioactive material used in the radiography study was examined with relative ease compared to the metallography.

Recent studies have simulated the hydride volume fraction in relation to the hydrostatic stress at the crack tip using a multi-physics model [125]. However, there have not been any validation studies of the hydrogen volume fractions within the given conditions. Additionally, current hydrogen volume fractions, or in other words hydrogen concentrations, have not yet been determined without destructive analysis, let alone with high precision. The main motivation of this study was to nondestructively determine local concentrations of hydrogen, specifically around the DHC crack tip in order to help validate DHC models.

7.2. Test parameters

The sample preparation regarding hydrogen charging, homogenization and final specimen cutting follows the procedure described in chapter 3. As described in chapter 4, each sample underwent fatigue pre-cracking, heat-up above the respective hydrogen dissolution temperature, and cool down to the defined test temperature.

7.2.1. Loading parameters

As previous described in chapter 4 the loading was defined based on the measured extensometer displacement. Again, the following equation shows how the loading was defined:

$$l_n = l_o - r \times d$$

where l_n, is the newly calculated load, l_o, is the initial load, r, is the reduction rate with units (N/mm), and d, is the extensometer displacement with units (mm). In Table 7.1, the specific values for the parameters can be found.
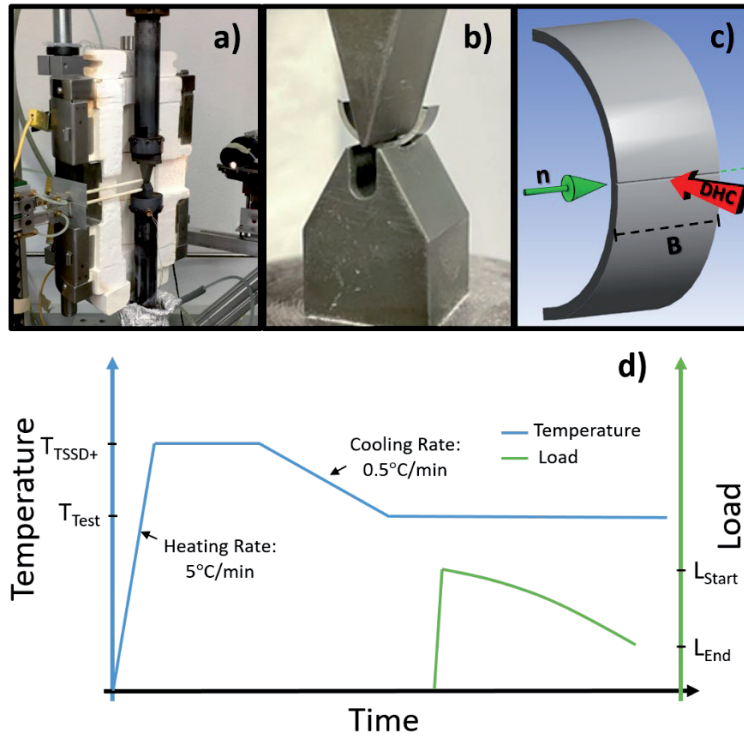
Figure 7.1: a) The 3-point bending test setup, displaying pulling rods, extensometer, and the open heating element. b) An enlarged image of the 3-point bending. c) The sample positioning with respect to oncoming neutron beam (green arrow and dashed line). The propagation direction of the DHC crack (red arrow) was oriented perpendicular to the neutron beam. The dimension, B, represents the specimen thickness. d) A typical test procedure after fatigue pre-cracking.

7.2.2.   Temperature parameters

The temperatures for hydrogen dissolution and testing can be found in Table 7.1.

Table 7.1: Material details including dimensions, hydrogen concentrations, and test temperatures.

Materials	Loading Parameters		Average	Uncertainty/stdv.	Test Dissolution Temperature	Test Temperature Range
	l_o	r	(wppm H)		°C	
LK3	50	50	328	20	500	160-410
LK3/L	100	60	381	40	500	160-410
LK3/L*	120-240	53	116	4	400	185-285
SINQ Target Rod	150	60	401	50	550	270-330
SINQ Target Rod (P0/P1/P19)**	120-220	53	70 / 113 / 143	4 / 10 / 59	550	270-330

*Irradiated in KKL **Irradiated in SINQ

7.3. POLDI beamline and neutron microscope setup

The neutron imaging of this work is based on experiments performed at the Pulse OverLap Diffractometer (POLDI) beamline of the Swiss spallation neutron source SINQ, located at the Paul Scherrer Institute, Villigen, Switzerland [126]. The PSI Neutron Microscope [127] equipped with a $^{157}Gd_2O_2S$:Tb scintillator [128], [129] and an Andor iKon-L CCD camera was employed for this study resulting in a pixel size of 2.7 μm. The spatial resolution of the neutron radiography images is, considering the sample extension in beam direction, between 8.1 and 9.3 μm [124].

Given the large differences in the neutron scattering cross sections of hydrogen and zirconium, hydrogenated zirconium samples are ideal candidates for neutron imaging. As the neutron scattering cross section is much higher for hydrogen, locations within the sample containing higher levels of hydrogen will scatter more neutrons, resulting in less neutrons reaching the detector. For regions of higher hydrogen content, the image contrast will appear darker, and for regions of less hydrogen content, brighter.

The cracked samples were positioned with the axial axis parallel to the neutron beam as seen in Figure 7.1 c) and imaged ex-situ at room temperature. The image processing followed as described by Gong et al. [10] in which acquisitions were taken with the sample (projection image - PI), without the sample (open beam - OB) and without neutron flux (dark current - DC) in order to remove the background noise read by the camera. Additional projections incorporating 'black bodies' (BB) were taken. The purpose of the BB projections is to correct for the undesired sample and background scattering contributions [130]–[132]. Active samples were placed inside of a so called 'active box' which is a sealed thin walled aluminum capsule to prevent any contamination [133].

7.4. Data analysis

The data was collected in the form of intensity image (.fits) stacks. The most basic processing followed the first image analysis described in the following subchapter, while the more accurate, BB-corrected, image analysis is described thereafter.

7.4.1. Standard image analysis

The first step required taking the pixel-wise median intensity of the stack of DC images. The respective median DC image was then pixel-wise subtracted from each image of the PI and OB stacks in order to remove camera noise. With the stack of PI and OB images (minus the median DC), the pixel-wise average intensity was taken for each stack. With the average intensity of the PI and OB, the PI was normalized with the OB through division resulting in the final image. The following equation summarizes the process.

$$\frac{(PI_{img.stck.} - DC_{stck.med.})_{ave.}}{(OB_{img.stck.} - DC_{stck.med.})_{ave.}} = Resulting\ Radiograph$$

7.4.2. BB-corrected image analysis

In order to correct for the undesired scattering contributions, kiptool was used to process the images [134]. Minor pre-processing was required to fit the toolbox, which included removing noise (DC) as described above. The guide for processing is found in the reference above.

7.5. Hydrogen quantification calibration

The neutron transmission of uniformly thick zirconium material containing homogeneously distributed hydrogen and a homogenous microstructure is affected by the total hydrogen content [10], [99], [100]. In the following equation $T(x,y)$ is the intensity image obtained through pixel-wise referencing described by Gong et al.[10] in x and y coordinates:

Equation 7.1

$$T(x,y) = \exp(-\sum_{as-received}(x,y) \times s(x,y) - \sigma_H N_H(x,y) \times s(x,y))$$

where $\sum_{as-received}(x,y)$ is the total cross-section of the as-received material and $s(x,y)$ is the pixel-wise path length of neutrons through the sample. In this experiment $s(x,y)$ is equivalent to the specimen thickness, s, as shown in Figure 7.1. The effect of hydrogen is defined by the microscopic cross-section σ_H multiplied by the atomic number density, N_H. As the samples have nearly identical lengths and the same microstructure, the neutron transmission value is only affected by the hydrogen concentration, thus simplifying Equation 3.5 to the following:

Equation 7.2

$$T(x,y) = a \times \exp(-b \times c_H(x,y))$$

where the variable a represents the neutron transmission in H-free material, while b represents the neutron sensitivity to hydrogen concentration, c_H, in wppm.

A thorough calibration study was performed with standards ranging from 10 to more than 2700 wppm H using the same methodology as described in the following reference [124]. Calibration studies using both alloys were performed to understand potential differences in the materials.

7.5.1.   Standards preparation

The standards used in the calibration process were created from alloys identical to those, which would be tested. As described in chapter 3, the samples were charged in iterative steps though gaseous charging. After each charge, the sample was heat treated and quenched in order to homogenize the hydrogen distribution. After each homogenization, a precise 2.0 or 4.0 mm sample was cut off. This process was continued in repeated steps in order to have increasingly charged samples as calibration standards. The hydrogen concentration of each standard used in the calibration process was measured through HVE after imaging, and can be found in Table 7.2.

Table 7.2: Hydrogen concentration overview of the calibration standards

Material	Hydrogen concentration (wppm)										
LK3 (2.0 mm)	12	89	239	400	745	962					
LK3 (4.0 mm)	39	38	118	224	185	390	814	1260	1360	1980	2830
SINQ (4.0 mm)	20	401	919	1740	1970	2710					

7.5.2.　HVE and transmission correlation

A quantitative analysis of the hydrogen concentration is possible through the correlation of the average transmission value with the hydrogen concentration of the respective reference sample. The transmission area used for calibration was at least 50,000 pixels from the samples seen in Figure 7.2 with a typical standard deviation of 0.01 by pixel. The area selected avoided any incorporation of the sample edge such that the edge effect or sample artifact would be excluded from the calibration process. According to equation 2 a curve was fitted to correlate the neutron transmission to hydrogen concentration for 2.0 mm samples (Figure 7.2). The grey scale found in the figure provides information about the relative intensity where the value, 1.0, is equivalent to transmission through air.
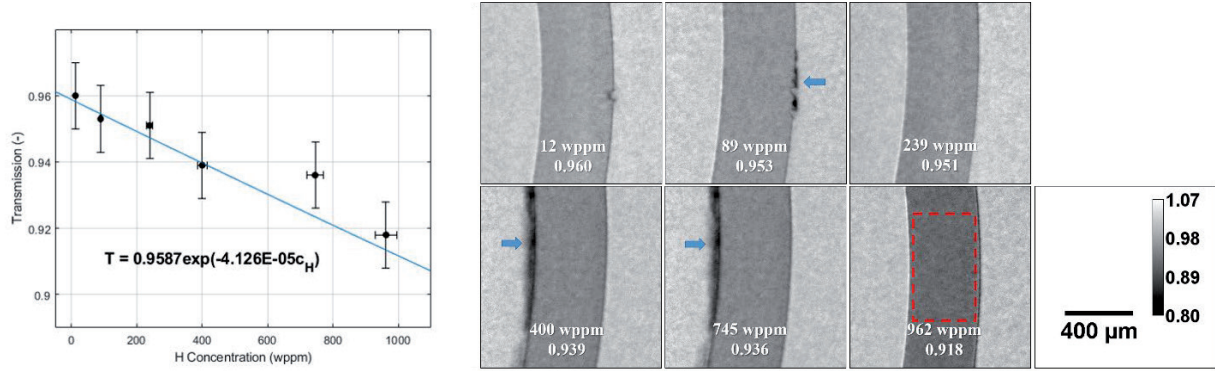
Figure 7.2: Left - Transmission results for the given reference samples with 2 mm length. An exponential curve is fit to measured transmissions and hydrogen concentrations. Right - Calibration radiographs used to calibrate transmission and hydrogen concentration. The 'as received' sample contains a fatigue pre-crack, and the 89 wppm sample contains a notch, both of which are not incorporated in the transmission measurement. The red dotted line encompasses the ROI for average transmission measurements. The blue arrows point out artifacts in the radiograph caused by sample contamination, which did not affect the transmission of the ROI. The material used for reference samples is the same as for DHC testing (LK3).

For this 2.0 mm sample study, the following equation was used for final hydrogen concentration quantification of LK3 matrix material:

Equation 7.3

$$T(x, y) = 0.9587 \exp(-4.126 \times 10^{-5} c_H(x, y))$$

The 95 percent confidence bounds resulted in uncertainties of ± 0.078 and $\pm 1.559 \times 10^{-5}$ for the coefficients a and b respectively.
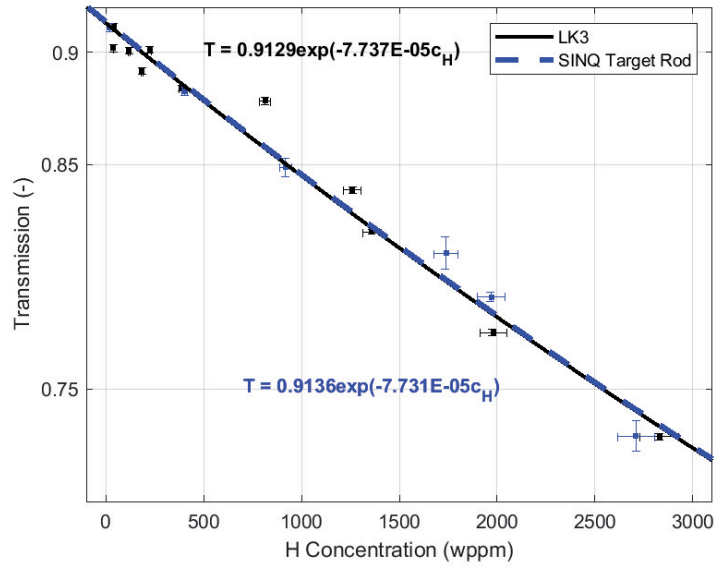
Figure 7.3 Transmission results for the given reference samples with 4 mm length. An exponential curve is fit to measured transmissions and hydrogen concentrations. Calibration radiographs used to calibrate transmission and hydrogen concentration.

For the 4.0 mm sample study, the following equation was used for final hydrogen concentration quantification of LK3 (Equation 7.4) and SINQ target rod material (Equation 7.5).

Equation 7.4

$$T(x, y) = 0.9129 \exp(-7.737 \times 10^{-5} c_H(x, y))$$

The 95 percent confidence bounds resulted in uncertainties of ± 0.0092 and $\pm 9.28 \times 10^{-6}$ for the coefficients a and b respectively.

Equation 7.5

$$T(x, y) = 0.9136 \exp(-7.731 \times 10^{-5} c_H(x, y))$$

The 95 percent confidence bounds resulted in uncertainties of ± 0.0186 and $\pm 1.373 \times 10^{-5}$ for the coefficients a and b respectively.

The attenuation for the two materials was expected to be very similar, however, it was necessary to confirm. After curve fitting, the curves were indeed very similar, with slight deviations in uncertainty. The uncertainty primarily comes from the sensitivity of transmission at low concentrations, as well as hydride homogeneity, which was less than ideal.

The quantification has been performed with the radial profile tool provided by ImageJ. The tool integrates the pixel intensity on the same radius (solid red arc of Figure 7.4) and divides by the number of pixels in the respective radius. The average intensity is then plotted with respect to the distance from the center of the arc as seen in Figure 7.4 (b). With equation 3, the transmission is then correlated to hydrogen concentration as seen in Figure 7.4 (c). It should be noted that the values closest to the tip might include some artifacts such as edge effects. However, most of the edge effect was avoided by intentionally selecting a smaller angle of integration. The drawback is that the densely hydride crack flanks are not included in the quantification. This process indeed provides average concentration profiles, however the deviation can be large when the hydrogen distribution is not uniform around the crack tip.
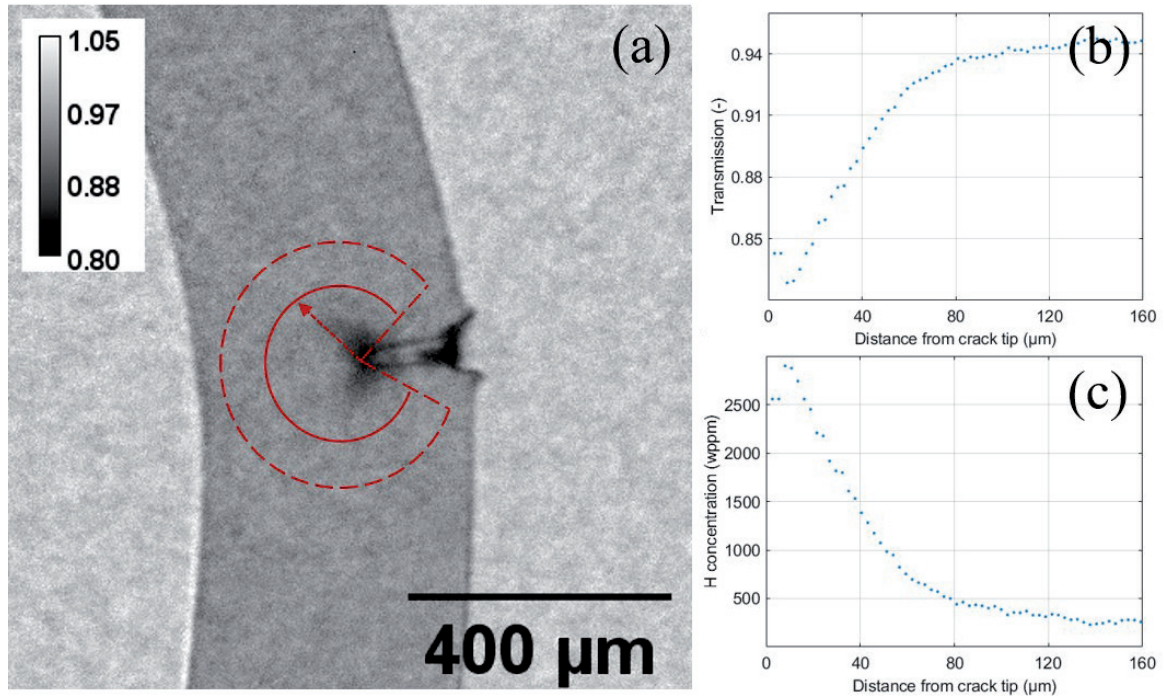
Figure 7.4: The quantification process taking a radial profile from the crack tip in (a) and plotting the average radial transmission (b). In (c) the transmission has been converted to H concentration based on the correlation. The Zircaloy-2 (LK3) sample contains 200 wppm H and was DHC-tested at 360°C.

7.6. Neutron radiography and quantification

A collection of the high-resolution neutron radiographies of all the samples are shown in the follow subchapters with respect to sample alloy, thickness, and hydrogen concentration. While the sample thickness for the DHC tests was always 4 mm, in this neutron imaging study, two sample thicknesses were imaged. One thickness was a 2.0 mm mid-section cut at the geometric middle of the 4 mm sample, i.e. the pure plane strain section, while the others were imaged as is, at 4.0 mm. The objective of the 2.0 mm sample was to image a homogenous and symmetric crack. In the following subchapters, the difficulties of selecting the proper location of the crack can be seen. Additionally the deficiencies of not cutting the sample mid-section can also be seen in concentration comparisons of the 4.0 mm samples.

It should be noted that at the interface of different indices of refraction (such as zirconium alloys and air) an edge effect can be observed [135]. The edge-effect is an artifact that makes quantification of results in the interface vicinity difficult and should not be confused with locations of high or low hydrogen concentrations. Other important observations made from radiography are features of the cracks which otherwise cannot be visualized without destructive testing. The radiograph resolution is high enough that crack tip blunting is able to be distinguished to some degree, distinction between stacks of circumferential hydrides can be made, and the liner-matrix-interface hydrides can clearly be distinguished. The primary objective of the metallography was to confirm possible hydride patterns seen in radiography as well as to observe in higher detail a selected cross section of the sample. After neutron imaging, each 4.0 mm sample was ground and polished to around one-third the specimen thickness, B, while the 2.0 mm samples where polished at the immediate surface in order to expose a cross section incorporating a pure plane strain region without destroying too much of the sample for fractography. Using the average DHC propagation length, the crack velocity was measured and can be found in chapter 5. The fractography results shown in the following subchapters display the samples which had been imaged with neutrons and polished for metallography. Therefore, the fractography represents about one-half (for the 2.0mm samples) and two-thirds (for the 4.0mm samples) of each sample as metallography is a destructive method. In Figure 7.8, the path of neutrons during neutron radiography crosses different crack zones before reaching the detector. As a result, the average transmission value is affected and can be seen when comparing to quantification results of previous neutron imaging experiments [124].

Gong et al. has shown in previous studies with the same neutron imaging setup at the POLDI beamline at SINQ that a spatial resolution based on an effective distance from the detector was calculated from images of a Siemens Star using the Fourier Ring Correlation method (FRC) [10], [136], [137]. Considering the path length through the material in front of the detector, in other words the neutron path through the 2.0/4.0 mm sample, the average, or

effective distance from the detector is 1.0/2.0 mm. From this midpoint, one can interpolate the effective spatial resolution as 8.1/9.3 μm.

7.6.1. LK3 unirradiated

7.6.1.1. Radiography and quantification of 2.0 mm LK3

Figure 7.5 qualitatively reveals the radial distribution of hydrogen around the crack tip. At each crack tip, a higher concentration of hydrogen is observed with respect to the bulk of the sample. Figure 7.6 provides the respective quantitative analysis around the crack tip from each of the samples of Figure 7.5. The trend shows that there is indeed an accumulation of hydrogen within a small radius around the crack tip, where the highest concentrations correlate to an increase in test temperatures. Additionally, the quantification shows that the hydrogen distribution converges about 120 μm away from the crack tip. In these converged regions, the measured concentration varies from about 100 to 500 wppm H. The measurements were limited by the size of radius applicable to the sample and crack position, providing margin for scatter in the region away from the crack tip.

The radiographs also show larger circumferential hydrides present in samples tested at lower temperatures while the tests at higher temperatures display an increased homogeneity in hydrogen distributions away from the crack tip.
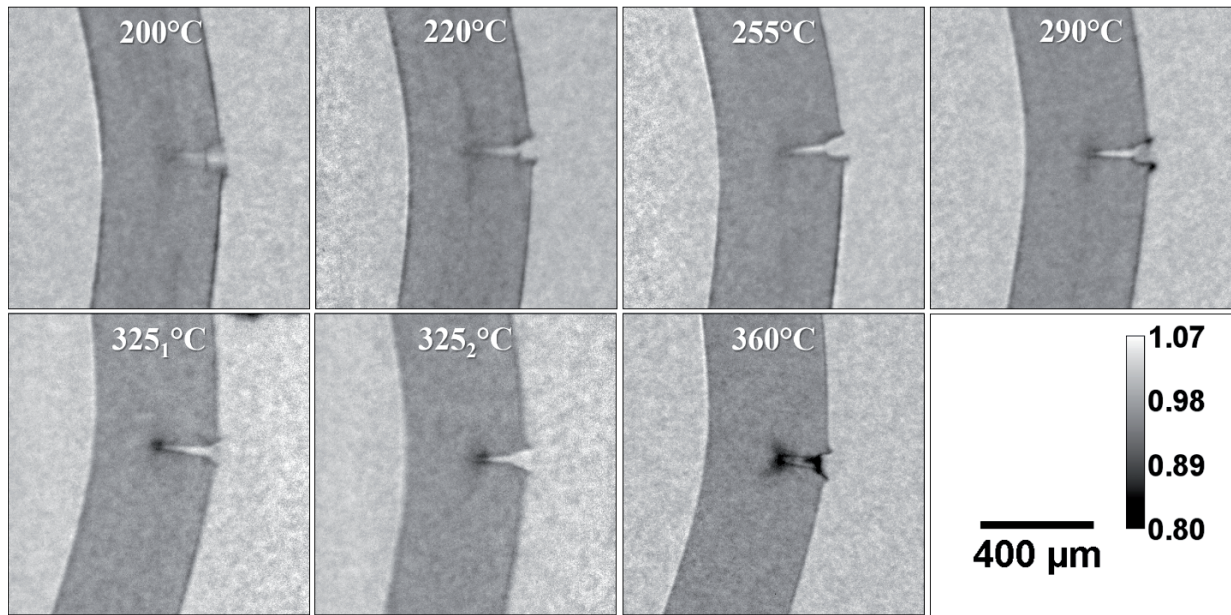
Figure 7.5: Radiographs of DHC samples at various test temperatures. The material used is Zircaloy-2 (LK3) with an integral concentration of 200 wppm H.
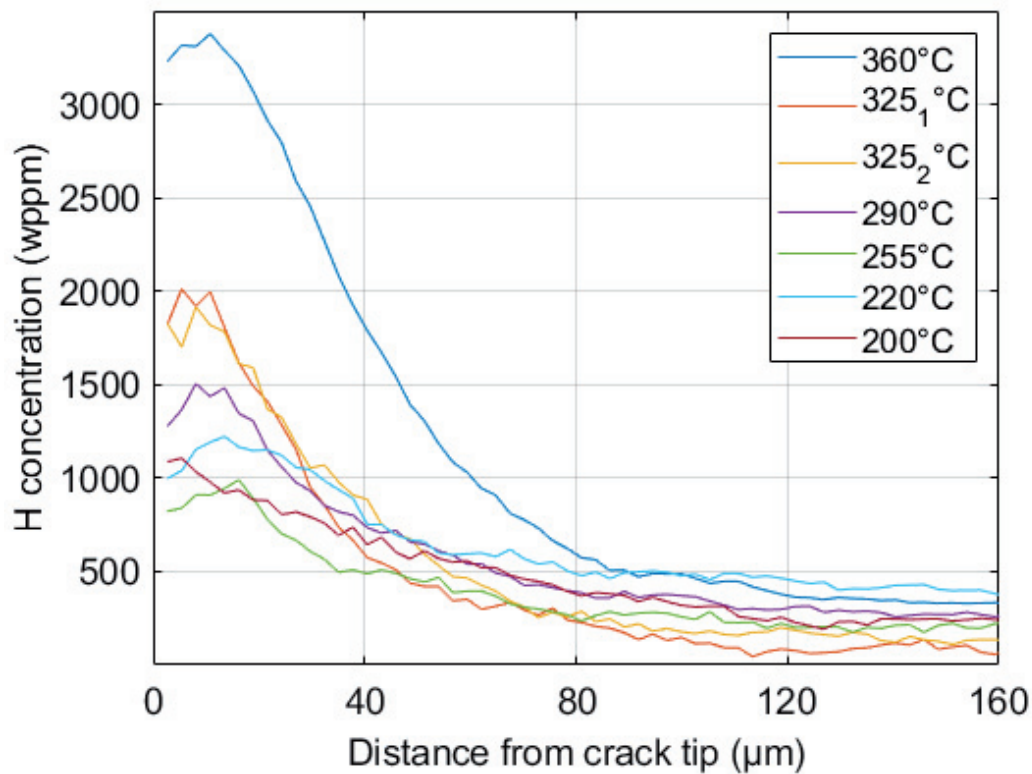
Figure 7.6: Average radial hydrogen concentration versus distance from the crack tip of LK3 samples, tested at various temperatures. The integral concentration of the samples was 200 wppm H.

7.6.1.2. Metallography and fractography of 2.0 mm LK3

After neutron radiography, the samples were polished at the immediate outer surface. Observed in Figure 7.7 are sample notches, fatigue cracks, and in some cases clear DHC regions. Fatigue regions extend immediately from the notch and are mostly hydride free at the flanks. DHC regions are characterized by the collection of hydrides at the crack flank and extend from the fatigue region to the tip of the crack. After test at higher temperatures, the large circumferential hydrides are less prominent, whereas samples at lower test temperatures have a greater concentration of large circumferential hydrides. In contrast, the finer, more uniformly distributed hydrides become more apparent after tests at higher temperatures. The finer hydrides could possibly represent reoriented hydrides caused by loading during testing, or the rapid precipitation of local hydrogen in solution at the end of the test caused by quenching. The lower test temperatures result in more circumferential hydrides due to the longer cooling time, given the same cooling rate (see Figure 7.1), until reaching the DHC test temperature and inherently lower solvus limit. Higher DHC test temperatures resulted in higher amounts of hydrogen in solution leading to a clearer temperature effect, making the hydrogen diffusion during DHC more apparent at high temperatures. The inner and outer edge of the sample is shaded as a result of significant rounding that occurred during the polishing process. The shading should not be confused with hydride build up.
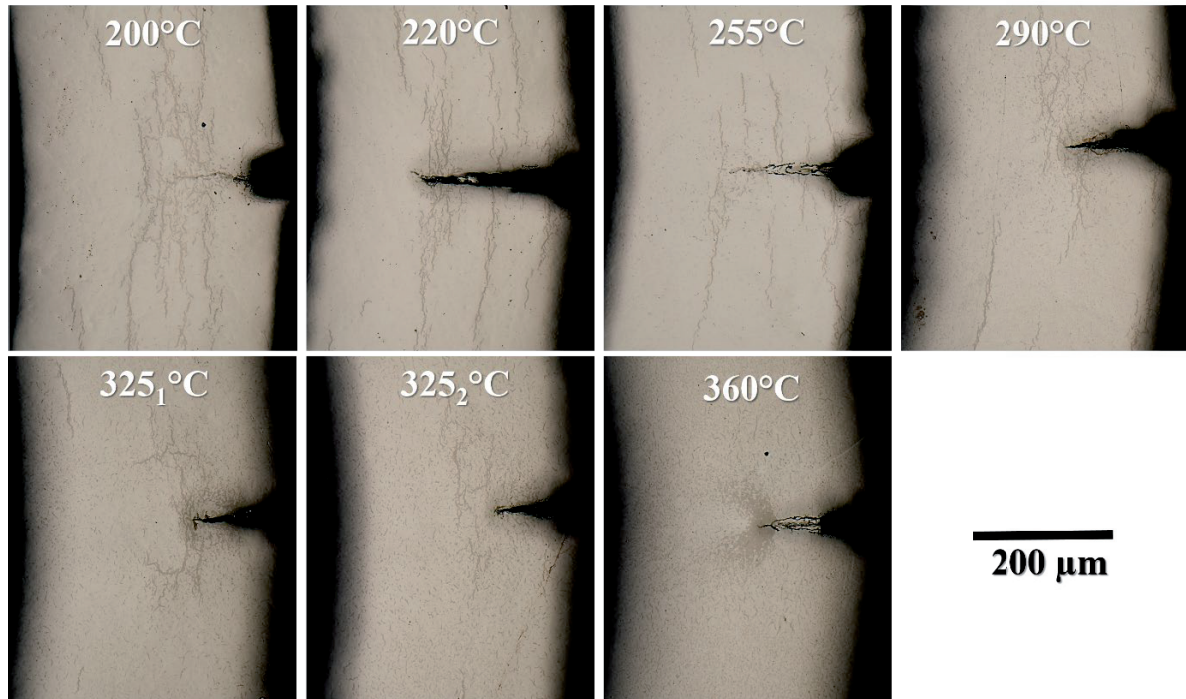
Figure 7.7: Light optical micrographs of neutron imaged LK3 samples (200 wppm H) from Figure 7.5.

After metallography was performed the samples were destructively forced apart, hinging at the DHC crack, thus revealing the crack front. The crack front imaged represents only a fraction of the total crack due to the sample width, B. The fractography shows primarily that the crack front of the section cut from the originally tested sample is not as symmetric or flat as desired. However, it can be seen in Figure 7.8 some of the samples were indeed cut in ideal locations for neutron imaging.

Further observations include the lack of pronounced DHC striations in either material which are commonly found in pressure tube samples [13], [76], [125]. Geometrical effects likely account for the fuel cladding tube samples lack of DHC striations, as the cladding wall thickness is too thin to accommodate such large striations as seen in pressure tubes[76].
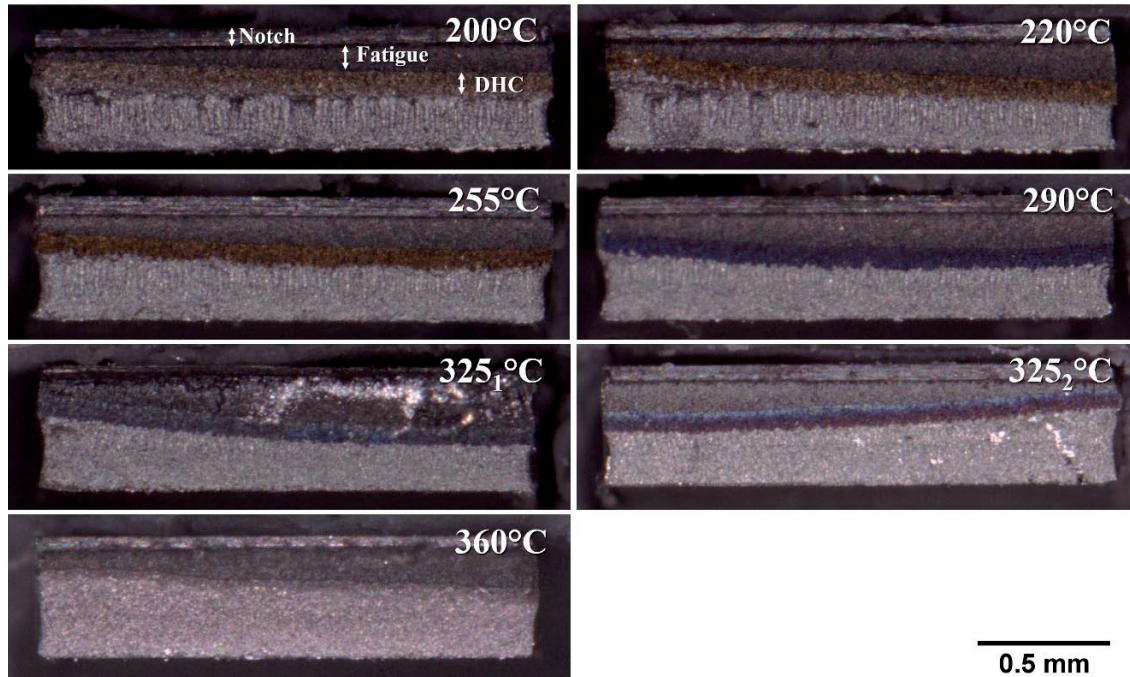
Figure 7.8: Fracture surface of the LK3 samples (200 wppm H) with respective test temperatures after metallography.

7.6.1.3. Radiography and hydrogen quantification of 4.0 mm LK3

Within the radiographs of the unirradiated LK3 samples (Figure 7.9), circumferential hydrides can be seen at 260°C and below, and hydrides along the crack flanks can be seen above 210°C where significant build up in a larger radius around the crack tip is seen at 360°C and above. Additionally, creep-induced crack tip blunting becomes obvious at temperatures of 360°C and above. Creep is also apparent when comparing the crack tip opening (CTO) versus crack length. At high test temperatures there are larger CTO's with shallower crack depths indicating that a more ductile displacement occurred during the test in order to reach the same extensometer displacement limit.

Figure 7.9: Radiographs of DHC samples at various test temperatures. The material used is Zircaloy-2 (LK3) with an integral concentration of 300 wppm H.

Figure 7.10: Overview of the hydrogen concentration around the crack tip for the LK3 (300 wppm H) samples imaged with neutrons (Figure 7.9). The integral hydrogen concentration can be found for the respective set with a dotted line. *no DHC occurred, just hydride build-up

7.6.1.4. Metallography and fractography of 4.0 mm LK3

The images of the LK3 unirradiated material in Figure 7.11 show a relatively homogeneous distribution of hydride precipitates throughout the sample given the temperature and excluding the crack tip region. At lower test temperatures it can be seen that the hydrides precipitate in a circumferential direction while nucleating upon one another. At higher test temperatures much of the hydrogen was likely still distributed in solid solution prior to post-test quenching, evident from the finer, more dispersed hydrides throughout the matrix. At the crack tip, hydride precipitation patterns correlate strongly with the test temperature as in neutron imaging. From the precipitation at the crack tips is evident at higher test temperatures, that there is more available hydrogen in solid solution which can diffuse towards the crack tip and precipitate. Conversely, at lower temperatures, the precipitation at the crack tip is minimal due to the lower amount of hydrogen in solid solution. In addition, the effect of temperature on creep and crack tip blunting can be seen. At temperatures of 360°C and above, blunting of the initial crack tip takes place, and at 410°C DHC crack growth appears to be completely inhibited. Interestingly, large amounts of hydrides still precipitate at the rounded tip increasing susceptibility for significant fracture in colder conditions. At high temperatures, the combined effect of DHC and creep shows its coupled nature.
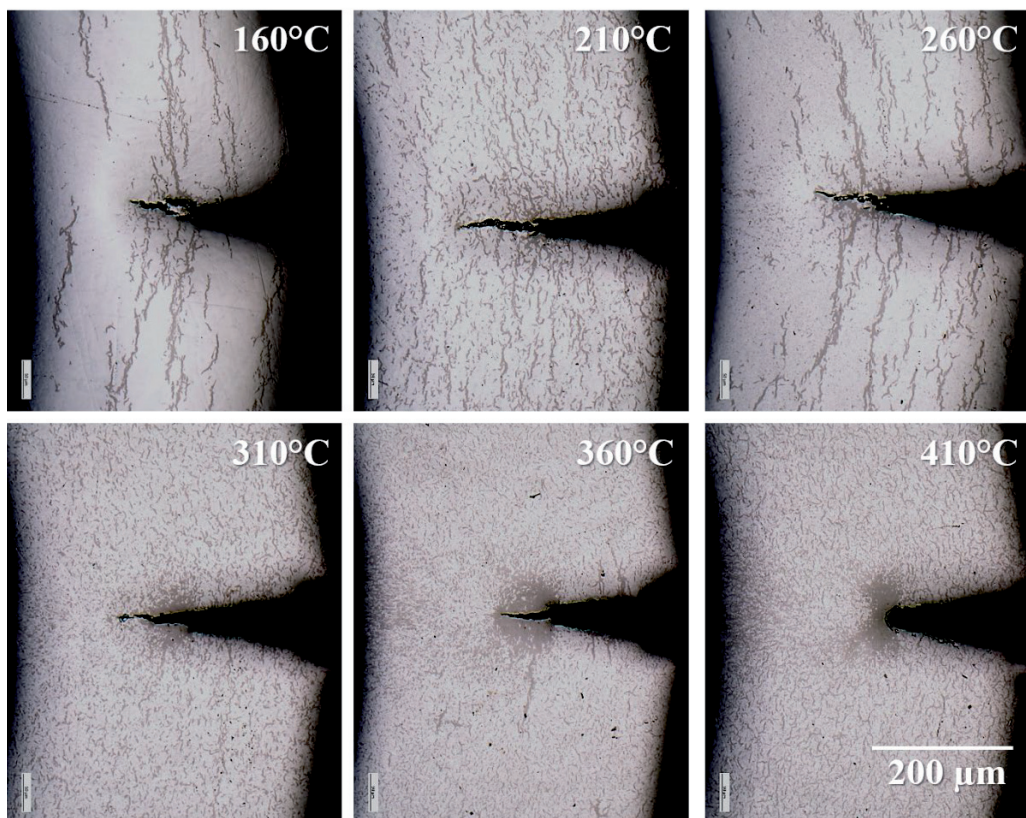
**Figure 7.11: Light optical micrographs of neutron imaged LK3 samples (200 wppm H) from Figure 7.9.**
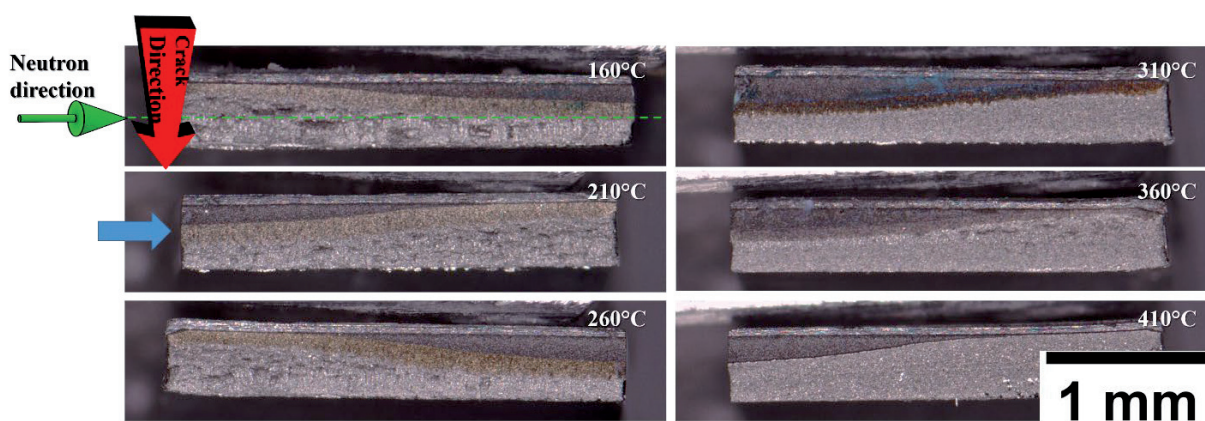
Figure 7.12: Fracture surface of the LK3 samples (320 wppm H) with respective test temperatures after metallography. The blue arrow indicates the side prepared for metallography.

7.6.2. LK3/L unirradiated and irradiated

7.6.2.1. Radiography and quantification of unirradiated 2.0 mm LK3/L

In Figure 7.13 the effect of the test temperature on the hydride build up at the liner-matrix interface is most prominent. However, unlike the radiographs in Figure 7.5, the hydrogen buildup is only apparent with the quantification, as shown in Figure 7.14. The trends show that the concentration reduces farther away from the crack tip. However, the extreme concentrations near the tip do not occur as in Figure 7.6 of the material without inner liner.
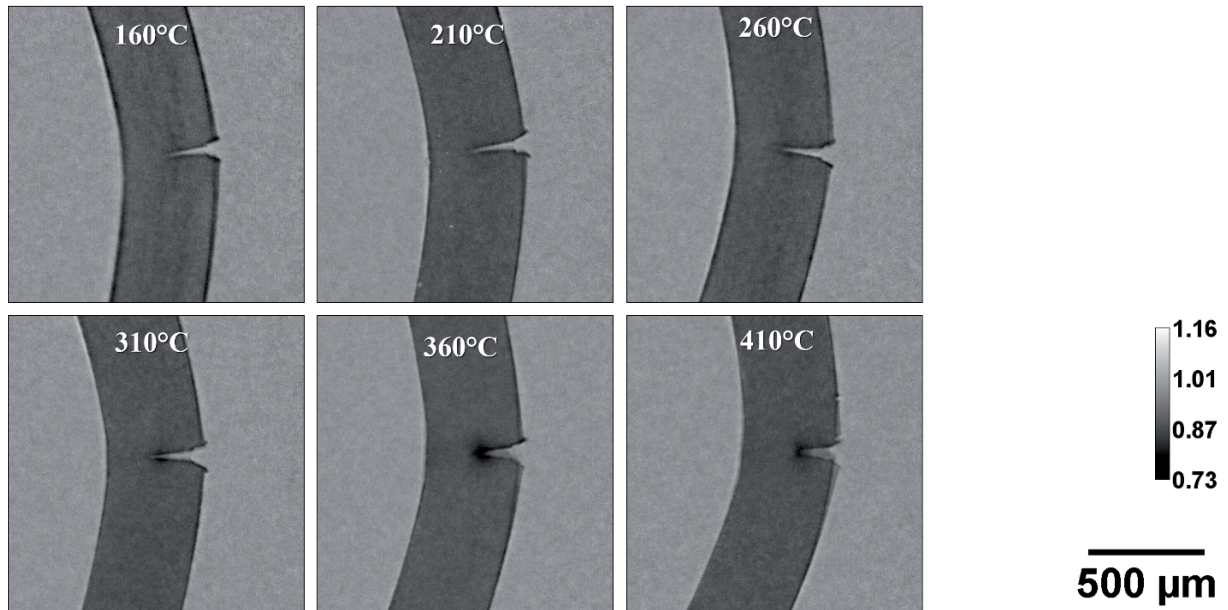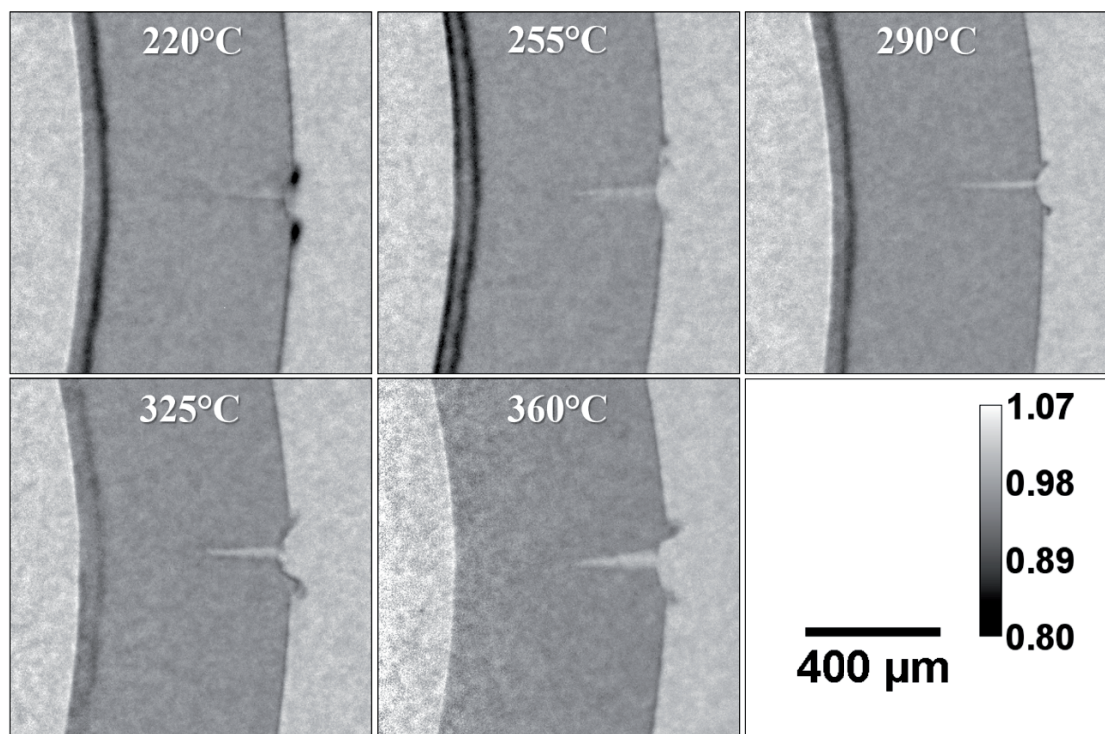

Figure 7.13: Radiographs of DHC samples at various test temperatures. The material used is Zircaloy-2 with an inner liner (LK3/L) with an integral concentration of 247 wppm H.
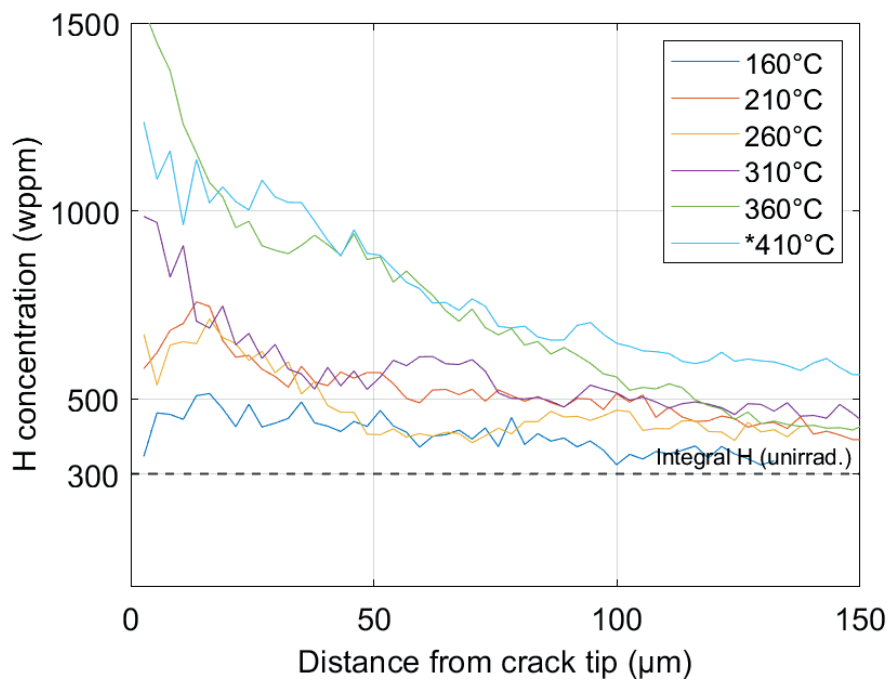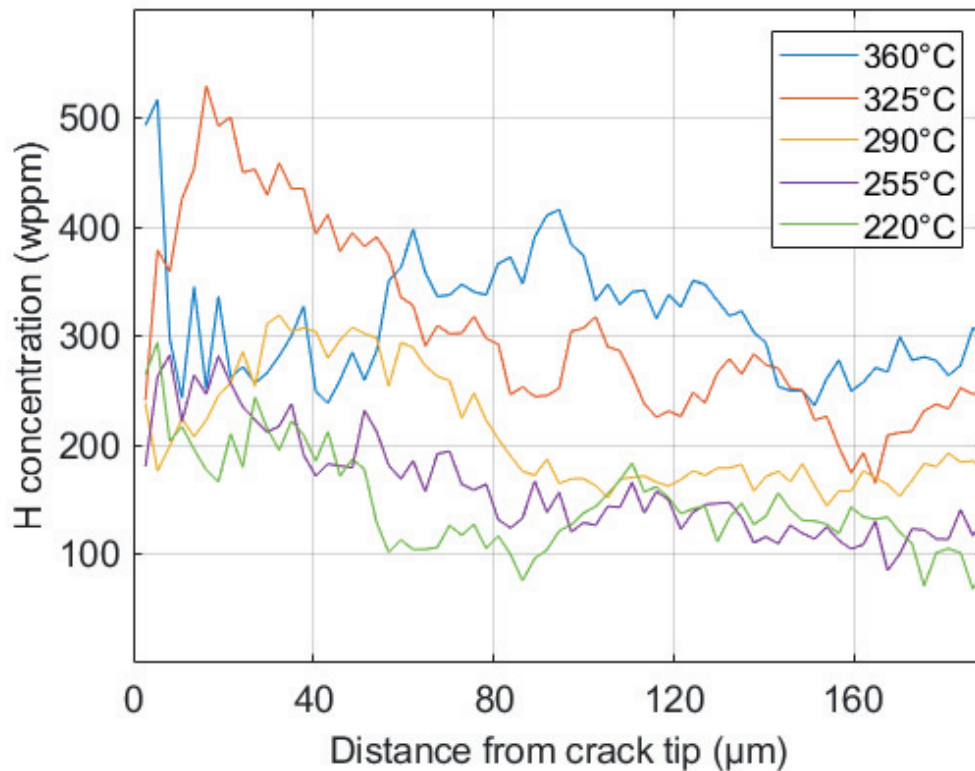
Figure 7.14: Overview of the hydrogen concentration around the crack tip for the LK3/L (247 wppm H) samples imaged with neutrons (Figure 7.12).

7.6.2.2. Metallography and fractography of unirradiated 2.0mm LK3/L

Figure 7.15 shows for the liner material that the cracks have not fully propagated at that particular cross section of the sample. Within most of these images, it is not distinguishable where the crack propagates from the notch. However, within the 290°C and 360°C samples the crack tip stretches circumferentially in a delaminating manner after fatigue precracking.
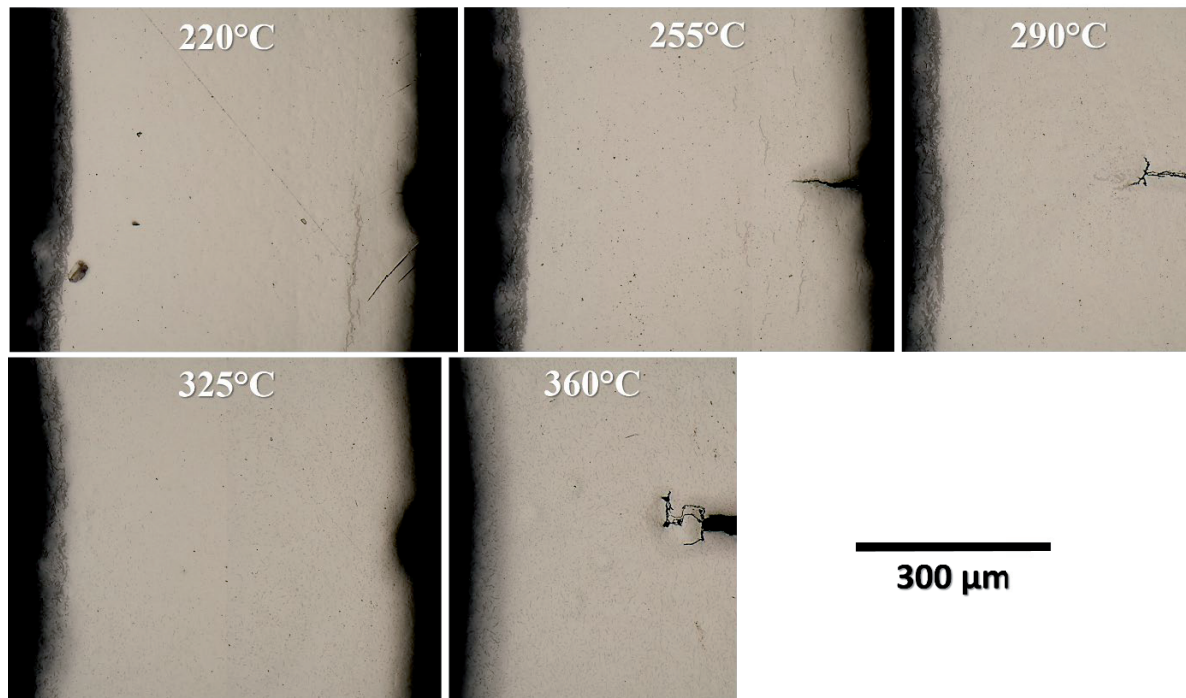
Figure 7.15: Light optical micrographs of neutron imaged LK3/L (247 wppm H) samples.

From the test data, it was known that for material with liner the DHC crack was not propagated as far as without liner. This is also evident in Figure 7.16 where the DHC region extends much less along with the unique topography of the DHC region. It appears from the topography that the DHC crack extends into the depth of the sample cross-section being imaged. When the metallography and fractography images are compared for sample at 290°C and 360°C it is evident that the cracks are indeed growing circumferentially, delaminating the cladding rather than splitting it radially. The same cavities representing such delamination can also be observed in the other liner samples even if it is not comparable with the metallography. It is notable that the same cavities are not observed in the material without liner.

Unlike the fractography of samples in Figure 7.8, the fractography of liner material in Figure 7.16 shows the crack front section used for neutron imaging is even less symmetrical than the originally uncut sample resulting in a transmission value of mixed zones.
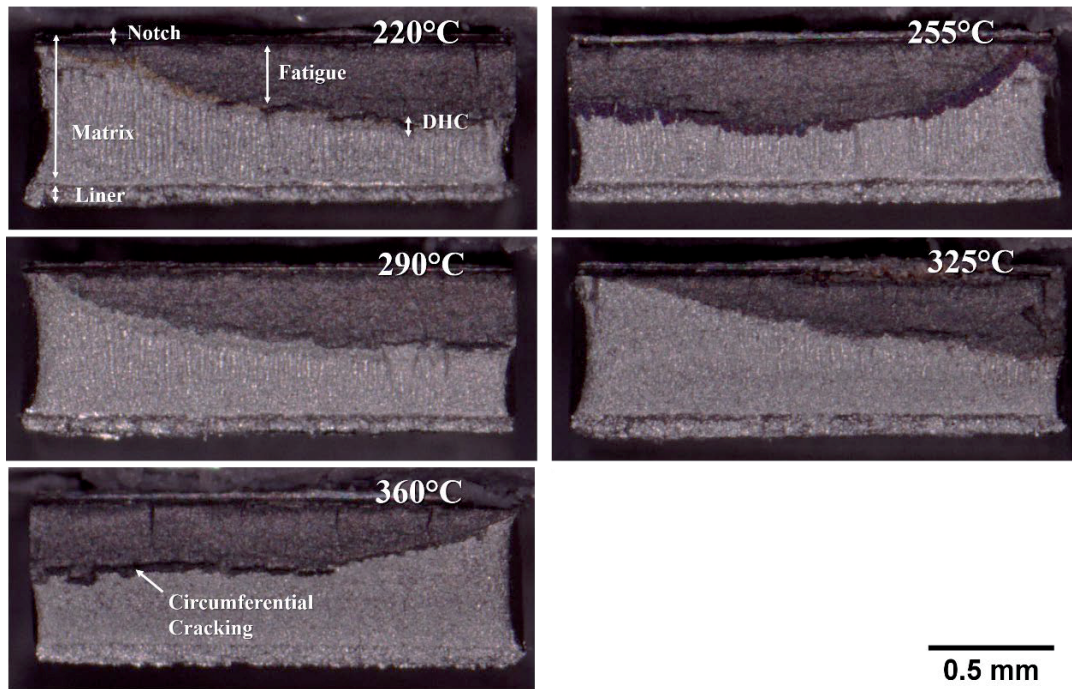
Figure 7.16: Fracture surfaces of the LK3/L (247 wppm H) samples with respective test temperature.

7.6.2.3. Radiography and quantification of unirradiated 4.0 mm LK3/L

Main observations of the unirradiated LK3/L (Figure 7.17) include the build-up of hydrides within the liner, the lack of visible circumferential hydrides, and build-up of hydrides at the crack flanks at 310°C and above. Any obvious circumferential hydrides are also lacking throughout the matrix, as seen in the LK3 material, likely due to the strong attraction of hydrogen to the liner causing a depletion in the matrix for any prominent circumferential hydride to precipitate. The liner also shows the effect of the test temperature where the precipitation in the liner decreases with an increased test temperature, most noticeably at 360°C and above. Build-up of hydrides around the crack tip appears less significant to that of the LK3 material, likely due to the prior diffusion of hydrogen into the liner where it subsequently precipitated. However, the appearance of hydride build-up around the crack flanks is still visible from temperatures of 310° and above which might simply be enhanced by the contrast to the surrounding depleted matrix.

Additionally, the hydrogen concentration in the LK3/L material at 310°C and below drops below the integral concentration of the sample. In some cases, the entire zone around the crack tip is reduced below the integral value. The low levels of hydrogen indicate that:

- The liner is significantly more attractive to hydrogen, even when the matrix experiences locally high tension loads.

- An overwhelming excess amount of hydrogen is not required to initiate the propagation of DHC or affect the crack velocity as seen in the following subchapter.
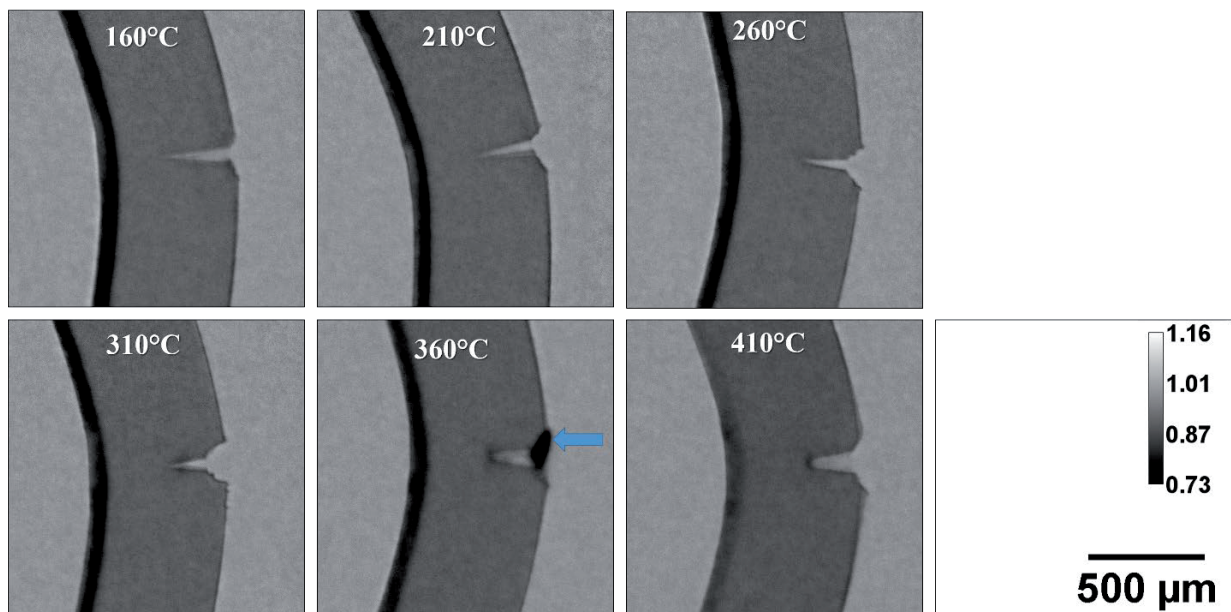
Figure 7.17: Radiographs of DHC samples at various test temperatures. The material used is Zircaloy-2 (LK3/L) with an integral concentration of 320 wppm H.
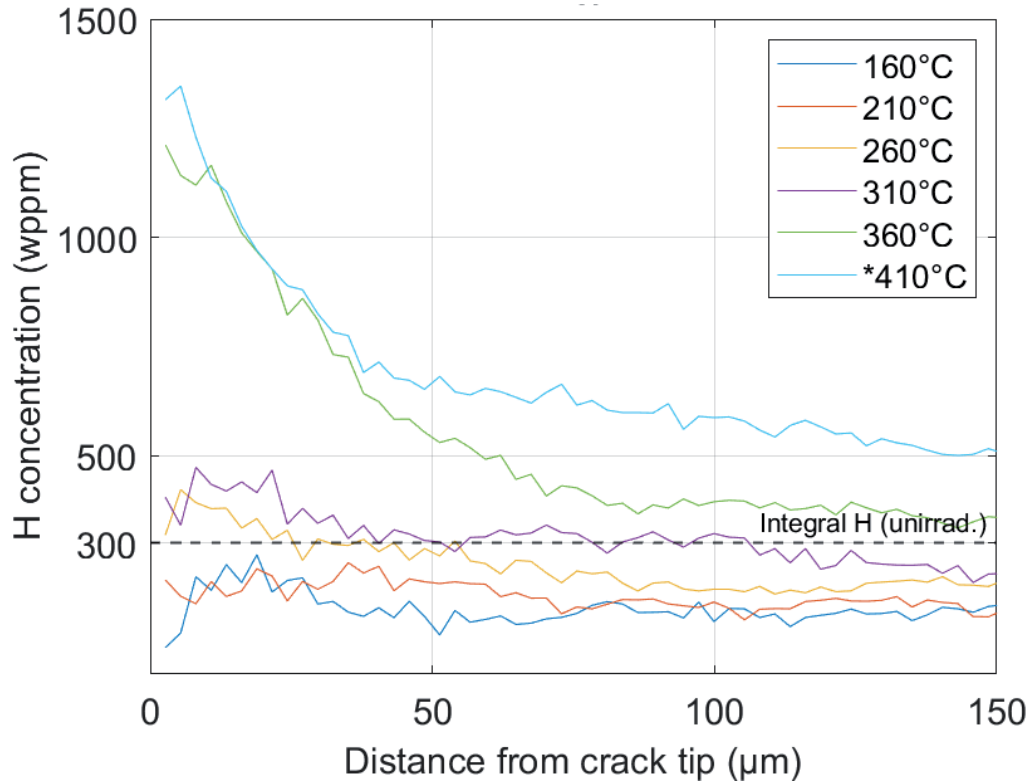
Figure 7.18: Overview of the hydrogen concentration around the crack tip for the LK3/L (320 wppm H) samples imaged with neutrons (Figure 7.17).

7.6.2.4. Metallography and fractography of unirradiated 4.0 mm LK3/L

Most obvious in the LK3/L metallography (Figure 7.19) is the accumulation of the hydrides within the liner with a preference towards the liner-matrix interface. As the chemical potential is lower in the liner material, the preferential precipitation in the liner is to be expected [10], [89]. Correspondingly, the matrix has a lower amount of precipitated hydrides. Each of the cracks are encompassed by hydrides as in the LK3 material with a similar trend, but to a lesser degree. Even though the visible magnitude of precipitation in the LK3/L material is less, hydrides are quite visible due to the contrast of the significantly less 'hydrided' surrounding matrix. Again, the crack tip blunting unveils itself at higher temperatures, especially above 360°C. Similar to the LK3 material at 410°C, significant precipitation occurs at the crack tip without any sign of DHC propagation. While it appears that the cladding is unsusceptible to

DHC at such elevated temperatures, significant hydride precipitation takes place at the stress riser. Assuming the precipitated hydrides do not dissolve again, this cladding material could also be left very susceptible to large fracture.
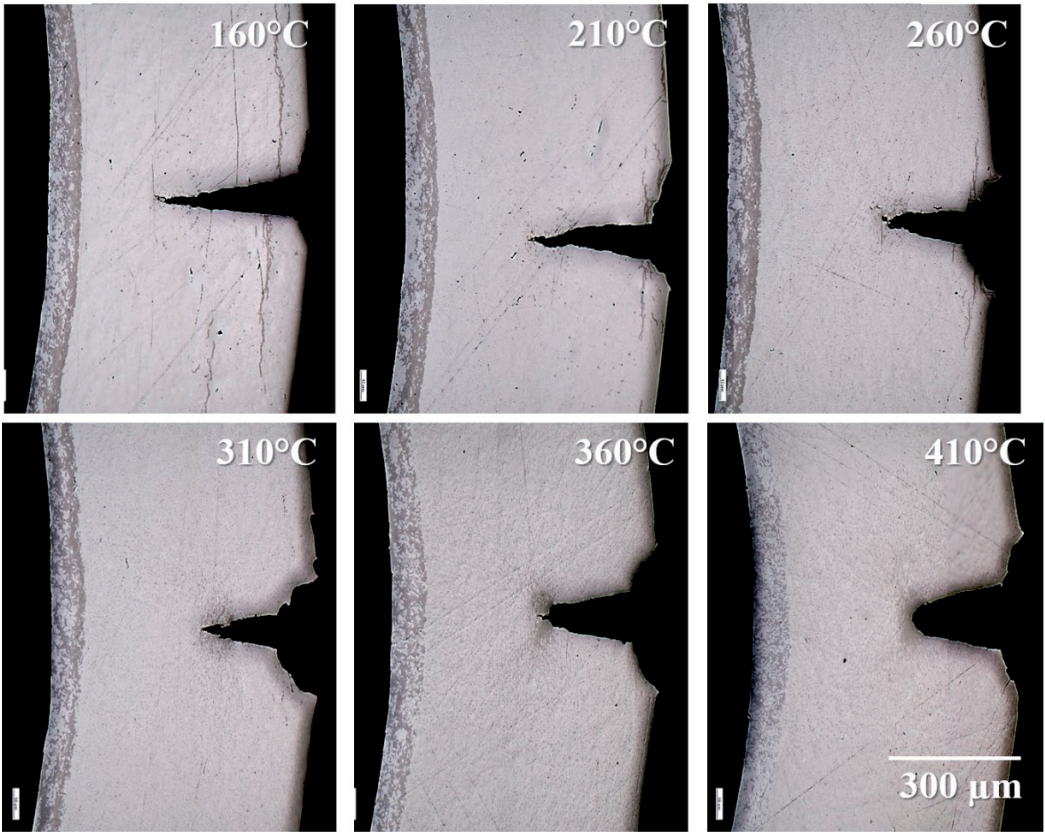
**Figure 7.19: Light optical micrographs of neutron imaged LK3/L (320 wppm H) samples.**
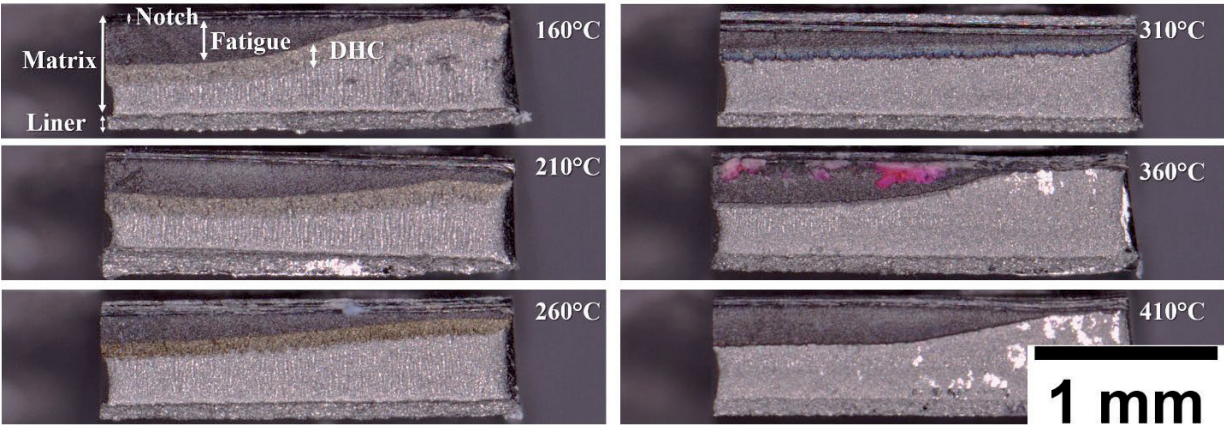
Figure 7.20: Fracture surfaces of the LK3/L (320 wppm H) samples with respective test temperature.

7.6.2.5. Radiography of irradiated 4.0 mm LK3/L

In the irradiated set of LK3/L samples (Figure 7.21) comparisons with the unirradiated materials include the number of cracks, crack depth, lack of significant hydride build-up at the crack tips, and less precipitation of hydrides at the liner-matrix interface. First, there are multitudes of cracks in the irradiated material compared to the single crack of the unirradiated material. The number of cracks was most likely due to an insufficiently cut notch as the oxide layer (~7-15 µm thick) was not able to be removed prior to notch cutting, making it challenging to assess the notch depth. The lack of a proper notch led to a reliance of crack initiation, during fatigue pre-cracking, on natural flaws in the material. Therefore, considering the material had undergone significant irradiation embrittlement and oxidation, there would have likely been many localized stress concentrator points on the outer surface susceptible to cracking [138], [139]. Considering the challenges of pre-cracking and embrittlement, the testing procedure resulted in a large variation in crack depths as seen in the radiographs. Again, neutron radiography displays the advantage of its technique by visualizing several cracks at once, which would likely be missed with destructive metallography or cost extremely high efforts to entirely capture. Unlike in the unirradiated material, there is no visually obvious hydrides at the crack tip or build-up around the tip. There is also less hydride precipitation in the liner compared to the unirradiated LK3/L, as that the hydrogen concentration was significantly lower. The trend of hydride precipitation at the liner-matrix interface with test temperature is similar to the unirradiated LK3/L material where the samples at higher test temperatures have less precipitation than those at lower test temperatures. An untested reference sample was also imaged to understand the starting conditions of the material. The reference sample indicates, from the liner-matrix interface precipitation, that the cladding was likely slowly cooled until a low temperature in order to allow for such hydride accumulation. Due to the irregularity and excess number of cracks in the irradiated LK3/L material (Figure 7.21), a quantification study was not possible.
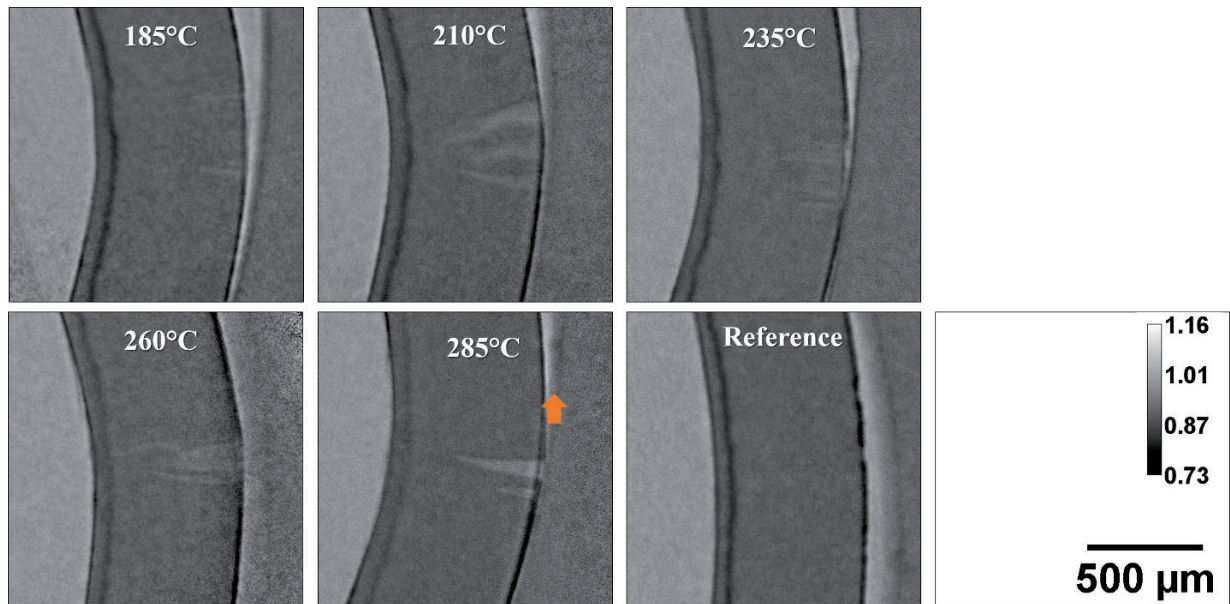
7.6.2.6. Metallography of irradiated 4.0 mm LK3/L

It should first be noted that the irradiated material was imaged using SEM with a BSE detector with the exception of the 185°C sample which was imaged with LOM (Figure 7.22). In addition, due to the challenges involved with irradiated material preparation, significant artifacts remain on the polished surface, which can be seen throughout the BSE images. Such artifacts include cloudy darker grey contrasts from smear layers and dark-bright-dark streaks caused by strong mechanical deformation from previous grinding steps.

However, there are some observations to be made regardless of artifacts. Significant hydride reorientation in the liner can be observed in the irradiated material where large compression stresses should be expected. The mid-section of the matrix shows hydrides, which have not reoriented in the radial direction, specifically the sample tested at 285°C. Diffusion of hydrogen appears not to happen as readily when under the influence of material interfaces or stress risers. More specifically, it can be seen that hydride distribution within the matrix remains relatively homogenous when compared to the unirradiated material, even near the crack flanks

and tip. The reference material shows signs that it did not undergo very high stresses during cooling and that cooling must have been relatively slow to allow the significant hydride build-up at the liner-matrix interface. More metallography investigations must be done on this material before further investigations can be performed as the surface preparation includes significant artifacts and the cross section does not incorporate the deepest part of the crack.
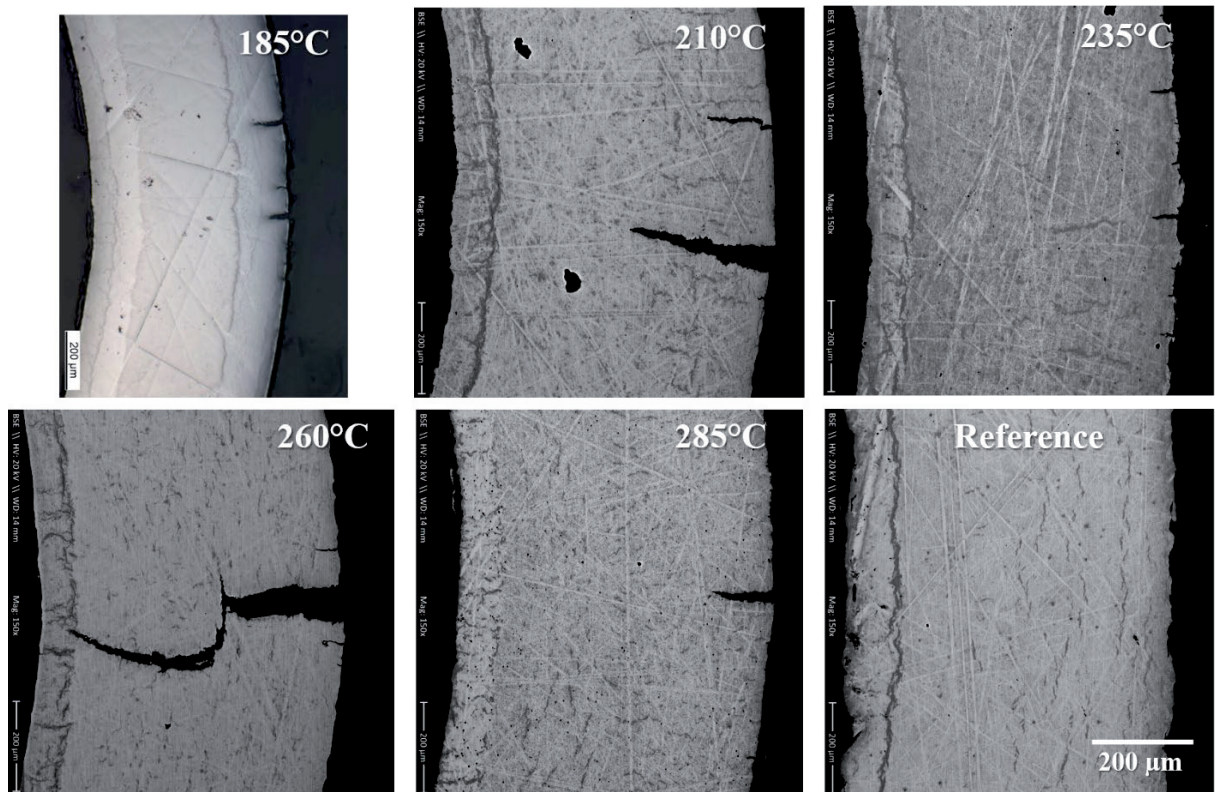
Figure 7.22: Electron back-scattered micrographs of the neutron imaged LK3/L (120 wppm H).

7.6.3. SINQ target rod unirradiated and irradiated

7.6.3.1. Radiography and quantification of 4.0 mm SINQ target rod

Similar observations can be made for the unirradiated SINQ target rod material (Figure 7.23) as for the LK3 material. Circumferential hydrides can be seen at lower temperatures, and

blunting is visible and higher hydride precipitation is visible at the higher test temperatures. However, the crack flanks show less significant hydride precipitation than in the LK3 materials. It is additionally obvious that the unirradiated SINQ target material has the highest hydrogen content due to the lower overall contrast.

In the irradiated SINQ target rod there is visually much less hydrogen in the bulk of the material compared to the unirradiated. In addition, there is no visible precipitation at or around the crack tip. However, it should be noted that the hydrogen measured from HVE in the target material likely originated from heavy water corrosion in the form of deuterium or protium from implantation. Knowing the scattering cross section of deuterium is lower, the comparison or calibration of the material to material charged with hydrogen becomes more complicated. From these results alone it cannot be determined if there was any hydrogen redistribution during the test or any significant DHC propagation. The following quantification study will allow a more detailed analysis of possible hydrogen redistribution or preferential locations of hydride precipitation.
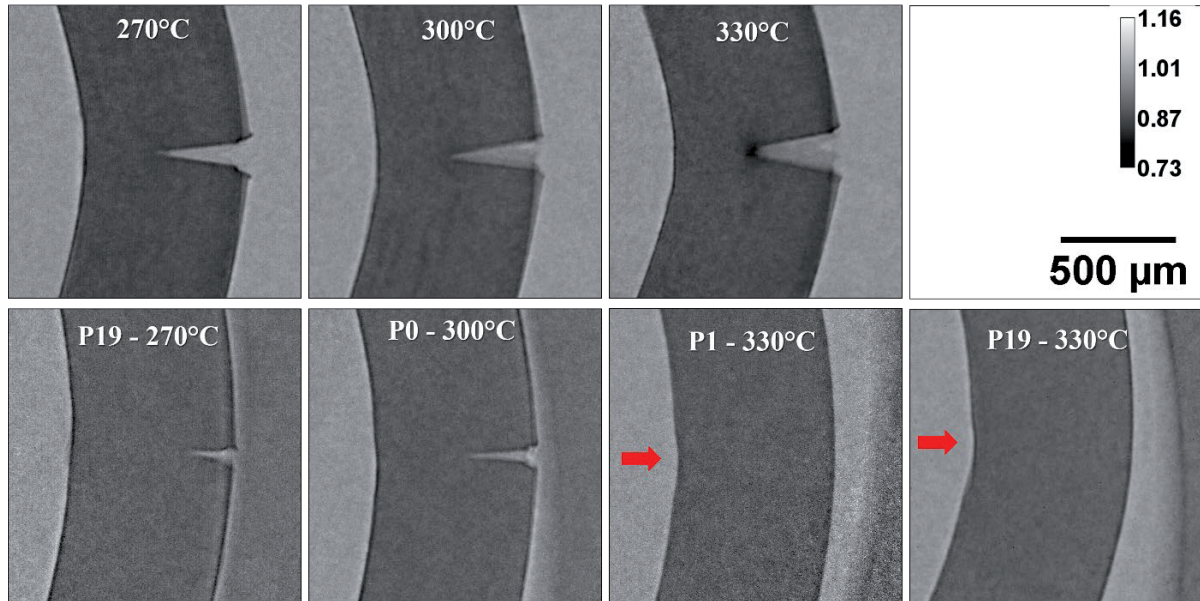
The unirradiated target material (Figure 7.24) indeed shows higher concentrations of hydrogen around the crack tip, however without the sharp peak at 270 and 300°C. At 330°C, an extreme peak can be seen which is much higher than the LK3 and LK3/L materials. In the irradiated material, radiography shows very low amounts of hydrogen in comparison to the unirradiated material. However, considering that deuterium is probably the main isotope of hydrogen in the material, calibration studies with hydrogen (protium) charged material become complicated as deuterium has a lower neutron scattering cross section. HVE measurements confirmed that the irradiated material has a lower hydrogen concentration (Table 7.1). Based on the hydrogen quantification and conformational HVE results, as well as the sharpness of the crack and respective loads, i.e. high stress concentration, it appears that the hydrogen resists diffusion towards the crack tip of the irradiated material. Even considering the non-cracked sample, there is little to no redistribution of hydrogen throughout the sample, especially at the bend point with the highest tensile stresses.
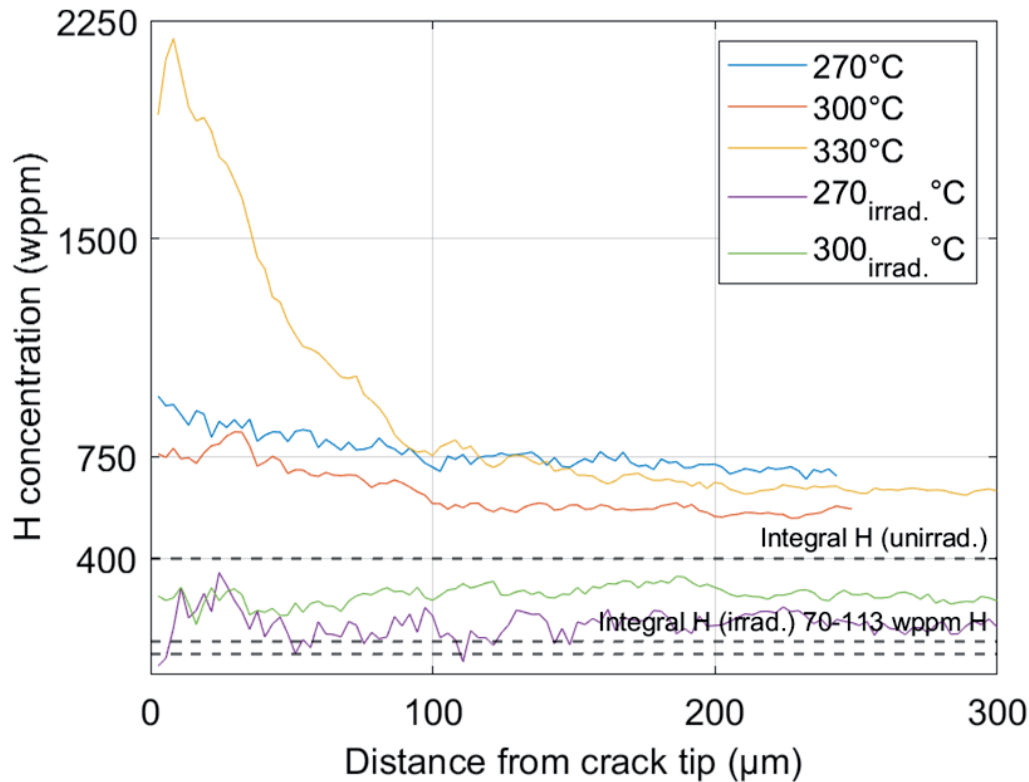
Figure 7.24: Overview of the hydrogen concentration around the crack tip for the irradiated and unirradiated SINQ target rod material of the samples imaged with neutrons (Figure 7.23).

7.6.3.2. Metallography and fractography of unirradiated 4.0 mm SINQ target rod

The most noticeable difference in the unirradiated SINQ target material (Figure 7.25) is the pattern of hydride precipitation being rather fine and distributed compared to the LK3 materials. The larger circumferential hydrides faintly seen in the radiographs are however not visible throughout the matrix in metallography, at least not at the location of the cut cross section. Hydrides at the crack tips collect in a similar trend to the LK3, but with a visually lower quantity. The crack tip at 330°C becomes blunt with a short hydride fracture, while the crack tip opening displacement (CTOD) is much larger than at other temperatures. The blunting and CTOD seen in all materials at high temperatures, is strongly indicative of creep induced displacement during the experiment.

Figure 7.25: Light optical micrographs of neutron imaged SINQ target rod material (401 wppm H) samples.
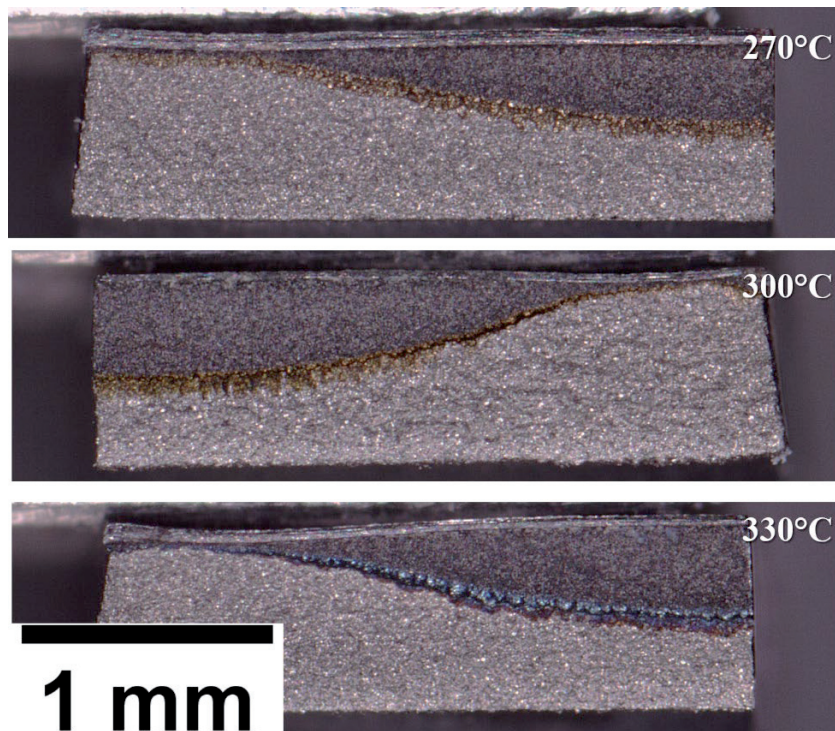
Figure 7.26: Fracture surfaces of the SINQ target rod material (401 wppm H) samples with respective test temperature.

7.6.3.3. Metallography of irradiated 4.0 mm SINQ target rod

Similarly, the irradiated SINQ material was imaged with the SEM using a BSE detector (Figure 7.27). Due to challenges in irradiated material preparation, the surface was not ideally

prepared for BSE imaging. However, significant hydride precipitates are not observed at all, even at the start of the crack tip of the samples tested at 270°C and 300°C. More metallography investigations must be done on this material before further investigations can be performed as the surface preparation includes significant artifacts and the cross section does not incorporate the deepest part of the crack.
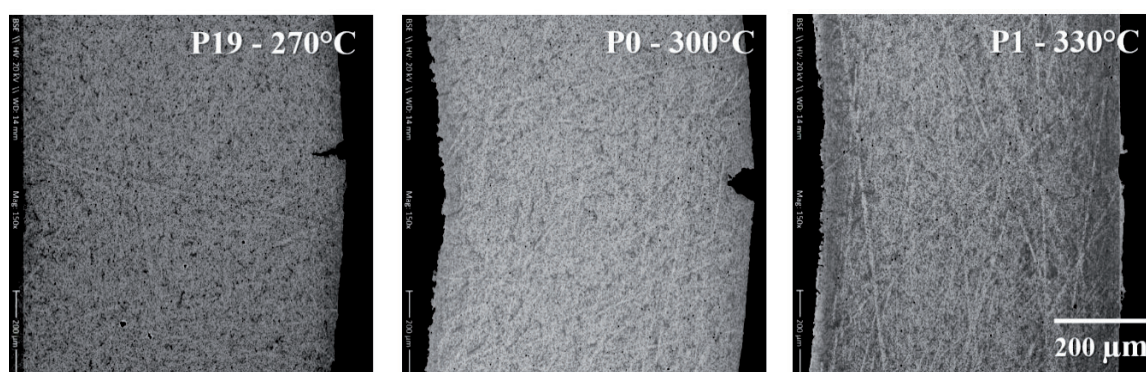
Figure 7.27: Electron back-scattered micrographs of the neutron imaged SINQ target rod material (73 - 113 wppm H).

7.7.   Discussion

The precipitation pattern in each of the LK3 samples is a result of the diffusion, which is temperature and stress dependent. At high test temperatures, more hydrogen away from the crack tip remains dispersed – and must have stayed in solid solution during testing – as can be seen by the uniform neutron transmission of the sample. At lower test temperatures, much of the hydrogen has precipitated – already prior to testing – in the form of large circumferential hydrides. In each case, the region of increased hydrogen concentration is strongly localized at the crack tip without showing signs of large hydride reorientation at the periphery. The lack of significant hydride reorientation away from the crack is likely due to the highly localized nature of the stress distribution of the 3-point bend test. The shape of the plotted hydrogen concentrations of the various graphs are very comparable to those hydride volume fractions

modeled by Xia et al. [125] giving confidence in the measurements accuracy close to the crack tip. As described by Xia et al., the maximum hydride fraction is just after the crack tip and quickly decreases with distance from the crack tip. Especially in the case of the LK3 sample at 360°C, seen both in Figure 7.5 and Figure 7.7 the precipitated hydrides visually show the correlation to hydrostatic stress. It is apparent that hydrogen quantification is highly sensitive to the section of crack selected for imaging. This was shown through accurately selecting a uniformly deep pure strain section (2.0 mm samples) where the quantification was much higher due to the lack of 'zone-mixing'. The 4.0 mm LK3 samples showed nearly half the hydrogen concentration as the transmission was a mix of the DHC and 'non-hydrided' zone.

In the LK3/L material, the precipitation is concentrated at the liner-matrix interface with the exception of the highest test temperature, which was estimated to be the terminal solid solubility for precipitation (TSSp) temperature for the given sample concentration. As the test temperature was reduced significant amounts of hydrogen diffused towards the interface reducing the available hydrogen for DHC propagation. Although the test parameters of the 2.0mm LK3/L samples resulted in a shallower DHC crack growth, there still appears to be a diffusion of hydrogen towards the crack tip, albeit much less than for the 2.0 mm LK3 samples without liner. The 4.0 mm LK3/L samples were more significantly cracked with increased loading parameters showing DHC was feasible in such material. The concentrations around the crack tip were however significantly lower when compared to the 4.0 mm LK3 samples, as the liner attracted the majority of hydrogen.

In the case of the 2.0 mm LK3/L and other cladding materials with a liner, without DHC conditions, the precipitation is significantly biased at the liner-matrix interface with a small zone depleted of hydrogen on the matrix-side of the interface [10], [89]. In this study, it was hypothesized prior to neutron imaging that there might be a similar depleted zone of hydrogen outside the hydride cluster around the crack tip for both LK3 and LK3/L material due to the significant precipitation during DHC. Such hypothesis was not entirely verifiable in this study due to the limited radial region analyzed. However, within the radius analyzed, no abrupt

depletion in hydrogen concentration is seen around the outside of the hydride cluster or near the crack tip. Possible reasons for the lack of depletion around the hydride cluster could be that the hydrogen source is much larger than the hydrogen sink. This would result in an overwhelming drive for the homogenization of hydrogen distribution, making the area of analysis too small to encompass any depleted zone. In other words, the source is the integral amount of hydrogen in solution in the entire sample, and the sink is the localized stress concentration at the fine crack tip. More specifically, any potential gradient or depletion of hydrogen in solid solution around the hydride cluster, could be quickly compensated through the larger integral source of hydrogen throughout the rest of the sample making any depletion undetectable.

Analogously, when considering the PFM, one may have expected an abrupt depletion or gradient in the hydrogen concentration near the crack flank or tip. However, such gradient near the crack tip, where PFM kinetics could unveil itself, are not observable. Additionally, it appears that the hydrides precipitate in relatively large volumes following the shear stress directions. Such directional precipitation is especially visible for the higher temperature tests without a liner. Where the stress is higher near the crack tip, the hydrogen concentration is also higher. This indicates the amount of hydrogen diffusion is respective of the stress level. Due to the shear-directional precipitation of hydrides and lack of a precipitation-induced gradient near the crack tip, it appears that the DFM better describes the mechanism for DHC.

In the end, the reason for the reduced hydrogen diffusion towards the crack tip can be twofold; first, the attraction of the hydrogen by the liner interface [10], and secondly, a change in the stress state between crack tip and liner because of a stiffening of the liner material caused by a plethora of hydrides, leading to a smaller stress intensity factor. A hint in this direction is the irregular shape of the small DHC cracks revealed by metallography. Both effects are temperature dependent, showing, (a) at lower temperatures the hydrogen is strongly attracted by the liner, (b) at mid-temperatures the hydrogen diffuses to the liner and to a smaller extent to the crack tip, but not enough to strongly promote DHC, and (c) at high temperatures enough

hydrogen would be available, however the precipitation at the crack tip is small. It is reminded that the DHC in these tests happens at constant temperature. It would be interesting to perform tests with slowly decreasing temperature, starting with a temperature that is high enough to dissolve enough hydrogen in the whole material, and to see whether the diffusion to the crack tip is over-compensated by the diffusion to the liner.

7.8.   Conclusion

DHC was investigated via three-point bend testing of irradiated and unirradiated Zircaloy-2 samples. Diffusion and precipitation patterns within a spectrum of test temperatures from 160°C to 410°C have been investigated using high-resolution neutron imaging, metallography, and fractography. The 2.0 and 4.0 mm sections of cladding encompassing the deepest location of the hydride crack resulted in an effective spatial resolution of 8.1 and 9.3 µm respectively. The influence of the DHC test temperature on hydrogen diffusion and precipitation was presented using high-resolution neutron imaging where radial concentration gradients were quantified around the tip of the arrested crack. Results show that the concentration within 10-20 µm of the crack tip can reach 1000 – 3300 wppm H depending on the test temperature for material without liner. Based on the quantification and precipitation patterns, it appears the DFM better describes DHC kinetics. The fine hydrides throughout the matrix at high temperature tests represent the hydrogen in solid solution prior to quenching, where the lower temperature tests show larger hydrides which initially formed upon cooling to test temperature. Fractography presented the regions of fatigue and DHC, which had been imaged with neutrons. Additionally, the liner material has been observed to crack circumferentially during DHC (under low loading parameters) whereas material without liner cracks radially.

The following key observations were made:

1. Hydrogen concentration increases around the DHC tip with increasing test temperature.

2. The liner depletes the matrix of hydrogen, however sufficient hydrogen diffusion occurs, enabling slower DHC crack velocities as observed in the material without liner.

3. Neutron radiography results display advantages of non-destructive testing especially through analysis of irradiated materials. Cracks can be observed and hydrogen concentrations can be analyzed where metallography is insufficient.

4. Irradiated LK3/L material shows preference of hydrogen diffusion towards and precipitation in the liner, however at less significant levels indicating that the irradiation damage has impacted the kinetics of hydrogen diffusion. Little to no hydrogen diffusion towards the crack tip occurred in the irradiated SINQ target rod material.

5. Creep begins to play a significant role after 300°C and appears to be the primary factor for deformation at 410°C. The effect of creep can be seen in the variation of velocities between load rates at 310°C where the slower load reduction leads to increased velocity due to the inclusion of creep deformation in the test time segment.

6. Neutron radiography and metallography show that hydrogen will continue to diffuse and precipitate around the crack tip regardless of crack propagation, i.e. when creep inhibits DHC. The crack velocity appears not to be strongly correlated with the amount of available hydrogen in solid solution at higher temperatures, rather amount of creep-induced crack tip blunting.

8. Micro-XRD phase mapping

The synchrotron micro-XRD experiments that took place at the micro-XAS beamline of the SLS at PSI are described in this chapter. Investigations were performed on 'cold' and 'hot' DHC cracks with the objective of identifying the hydride phases responsible for DHC. The preparation of samples via mechanical polishing and FIB milling are described in the first subchapter. In the following subchapters, beamline parameters and raw data analysis are described. Finally, X-ray diffraction phase maps, along with respective phase analysis are presented and discussed.
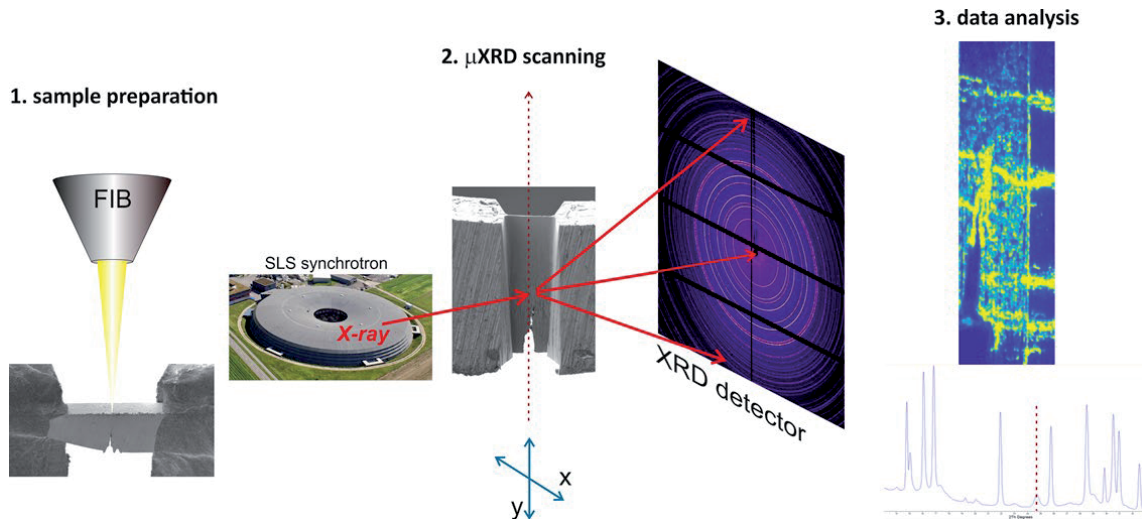
Figure 8.1: General overview of the sample preparation, XRD measurements, and data processing.

8.1.   Motivation

Several phases of zirconium hydrides are known in literature and are dependent on various factors including hydrogen concentration, temperature of precipitation, microstructure and alloying elements [46], [49], [100], [140]. Studies specifically on the phase identification of δ- and γ- hydrides have utilized transmission electron microscopy (TEM), electron energy loss spectroscopy (EELS), and XRD in reflection mode. The primary objective has been to understand better the complex hydride precipitation process. Mechanical properties have also

been reported on the variation of the two phases where the fracture toughness increases with the increase in volume fraction of γ- hydrides [39], [102], [141]. The studies have generally been focused within the context of DHC, as DHC is considered one of the most detrimental effects from hydride precipitation in zirconium alloys. To further ensure the integrity of fuel cladding, a better understanding of the precipitation process and mechanical properties of the various hydride phases is needed. Through the study of an intact DHC crack, important information about the precipitation kinetics can be obtained. Literature suggests investigations of DHC cracks with the preparation of FIB to reduce strain-induced artifacts [45].

8.2.   Sample preparation

The first preparations of the samples followed the description in chapter 3. The DHC propagation followed the steps in chapter 5, which describes velocity experiments. Subsequently, the samples were mechanically ground to a thin lamella where they were mounted on an SEM stub for further FIB polishing.

8.2.1.   Mechanical preparation

Subsequent to the DHC testing, samples were mounted to a cylindrical aluminum stub that fit inside a stainless steel tube with a pass-fit (like a piston and cylinder). With this device Figure 8.2, a controllable amount of the sample was extruded from, and fixed to the stainless steel tube. This allowed for a controllable depth of grinding and polishing during the various steps. The first step, as seen in Figure 8.3 (b), was to grind the inner diameter of the cladding flat in order to reduce the material that would need to be later be removed by FIB. Next, the sample was remounted on the side such that the crack cross section could ground and polished. The desired cross section was selected (mid-section of sample) and then ground and polished. The sample was polished on both sides to a thickness manageable for FIB polishing (less than ~100 μm).
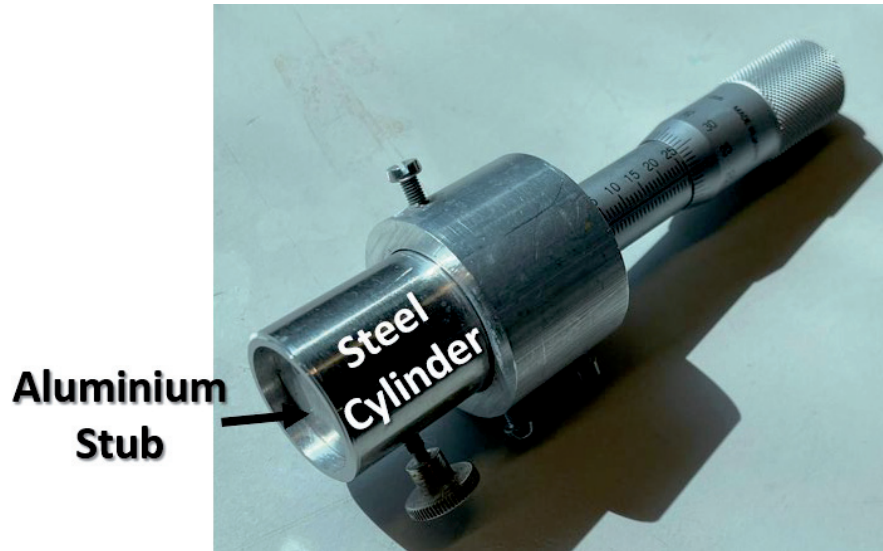
Figure 8.2: Tool designed for polishing samples to select depths.
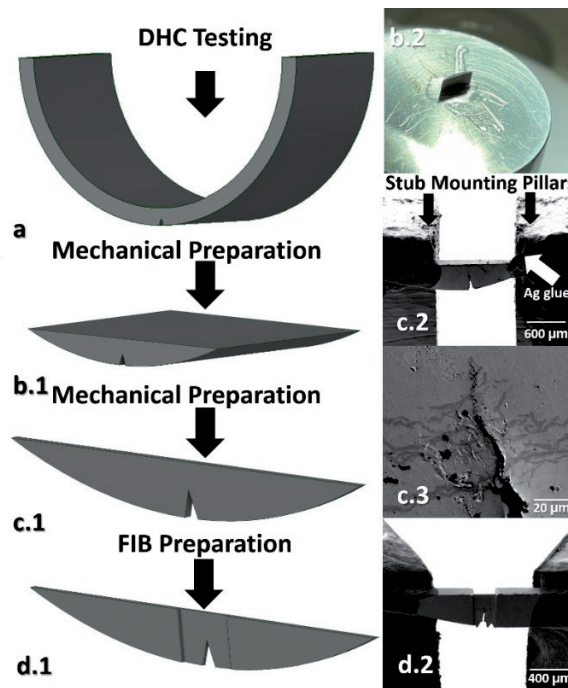
Figure 8.3: CAD models and SEM images of preparations process from DHC testing to FIB polishing. a) post DHC testing b.1) after polishing the inner cladding surface flat b.2) the flattened sample mounted for c.1 preparations c.1) CAD image of the thin section prepared for FIB milling c.2) SEM image of the mounted sample c.3) enlarged view of crack tip prior to FIB milling d.1) CAD image of the FIB milling d.2) SEM image of the FIB milling

8.2.1.1. Metallography

Prior to FIB polishing metallography was performed to understand where the crack was positioned in the sample and confirm that DHC had taken place. In Figure 8.4, the three samples used for XRD phase mapping are shown with details of the hydride precipitation throughout the matrix and along the crack flanks. Based on these images, the locations of hydrides were confirmed and used as references points for the XRD study, considering the size of the beam.
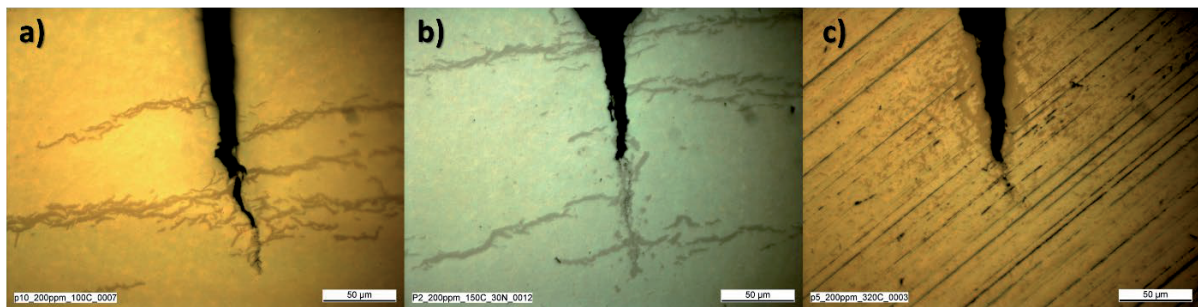
Figure 8.4: A metallographic overview of the samples just before SEM mounting and FIB polishing. a) test temperature 100°C b) test temperature 150°C c) test temperature 320°C.

8.2.2. FIB preparation

After sufficient mechanical preparation, the samples were mounted to a modified SEM stub that had two pillars for mounting the sample and allowing an X-ray beam to pass, see Figure 8.3. The samples were fixed with silver glue that is typically used in electron microscopy (Figure 8.3 (a)). Prior to FIB milling, images were recorded providing additional metallography (Figure 8.3 (b)) that could be compared to the LOM metallography (Figure 8.4 (a)).The samples were then milled with a FIB in successive, current reduction, steps. The first milling step started with a high current and ending with a low, from 45 nA to 6.5 nA at 30 keV to reduce the FIB amorphous layer while milling efficiently. The sample was oriented with the cross-sectional plane parallel to the FIB beam such that the cross section could be reduced,

as seen in the reduction of the sample in Figure 8.3. In the end, the samples were between 10 – 15 µm thick. Due to the large depth of cut, relative to FIB milling, there was likely 'skirting' of the sample. The skirting resulted in a larger thickness of deeper regions milled, which in this case, was not a problem.

8.3.   Micro-XAS set-up

The detector used in these experiments was the Dectris Eiger 4M [142], [143]. The sample was scanned by the rasterization of the sample through the beam. In other words, the stage moved the sample in xy plane normal to the beam over the selected ROI with a defined step size and acquisition time for each step. The scanning is also described in the following subchapters (Figure 8.6). Such parameters of the beam and step sizes can be found in the following table. Two samples were measured with beam energies of 17.95 keV, and one with 17.2 keV as well as a slightly different sample-detector relative position, which defines the angular range of the measured diffraction patterns. Energies and detector positions were based on the given constraints of the respective beamtime.

Table 8.1: Parameters used for imaging the three samples described in this chapter.

Sample DHC test temperature	Energy (keV)	Wavelength (Å)	Step Size (µm)	Beam Size (µm)
100°C	17.95	0.6907		
150°C			0.5	~1.0
320°C	17.2	0.7209		
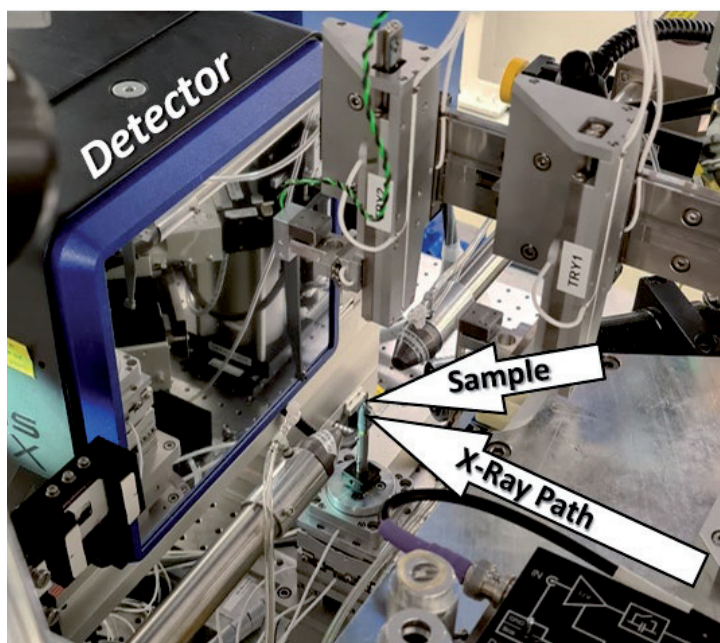
Figure 8.5: Overview of the micro-XAS setup used for micro-XRD phase mapping.

8.4. Data analysis methodology

The following subchapters describe the workflow of data analysis starting with the raw data as well as the post processing for further phase analysis.

8.4.1. Workflow

The first step in processing the raw data (images of Debye-Scherrer rings) involved applying the python fast azimuthal integration (PyFAI) using a generated calibration file in order to create the 1D diffraction pattern [144].
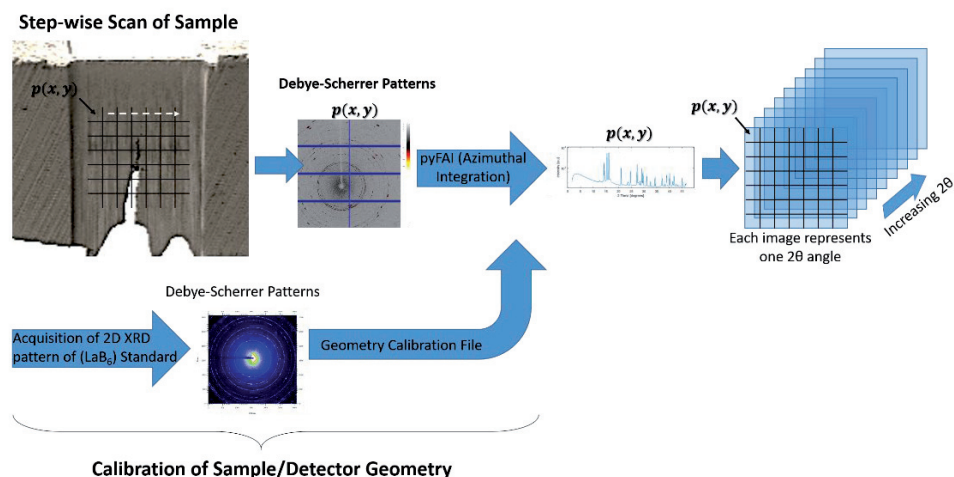
Figure 8.6: Detailed workflow from imaging to data processing.

Following the azimuthal integration, a stack of 1D XRD patterns (.tiff files) was created. The stack of 1D XRD patterns was then loaded into a Matlab script where the XRD patterns were assigned to corresponding pixels in the ROI, thus generating separate images for each diffraction angle. Each image in the obtained stack displays intensities measured for a given diffraction angle. Within the Matlab-created stack, the user could create a unique polygon shape within a single image. The objective was to encompass a region of interest with this polygon that included only, or mostly, the phase of interest. Each of the pixels, or sample position, within the user-defined polygon contained the one-dimensional diffraction pattern that were integrated into one pattern. This tool allowed the user to highlight less intense diffraction peaks of certain phases within an integral 1D diffraction pattern by excluding regions not of interest. In other words, the zirconium phase, which gives very strong diffraction signals, could be reduced by eliminating regions of mostly pure zirconium, and including only hydride. This is especially important when the hydride phase produces a low signal and makes up a small fraction of the material imaged.

8.4.2. Calibration procedure

A LaB6 standard is used for the calibration of the measurement. As the crystal structure of the standard is well known, the geometry of the setup can be defined based on the measurement

151

of its diffraction pattern. Afterwards, the calibration file with geometrical parameters is used in the algorithm for azimuthal integration of the Debye-Scherrer rings acquired for the investigated samples. This required calibration step is shown in the workflow of subchapter 8.4.1.
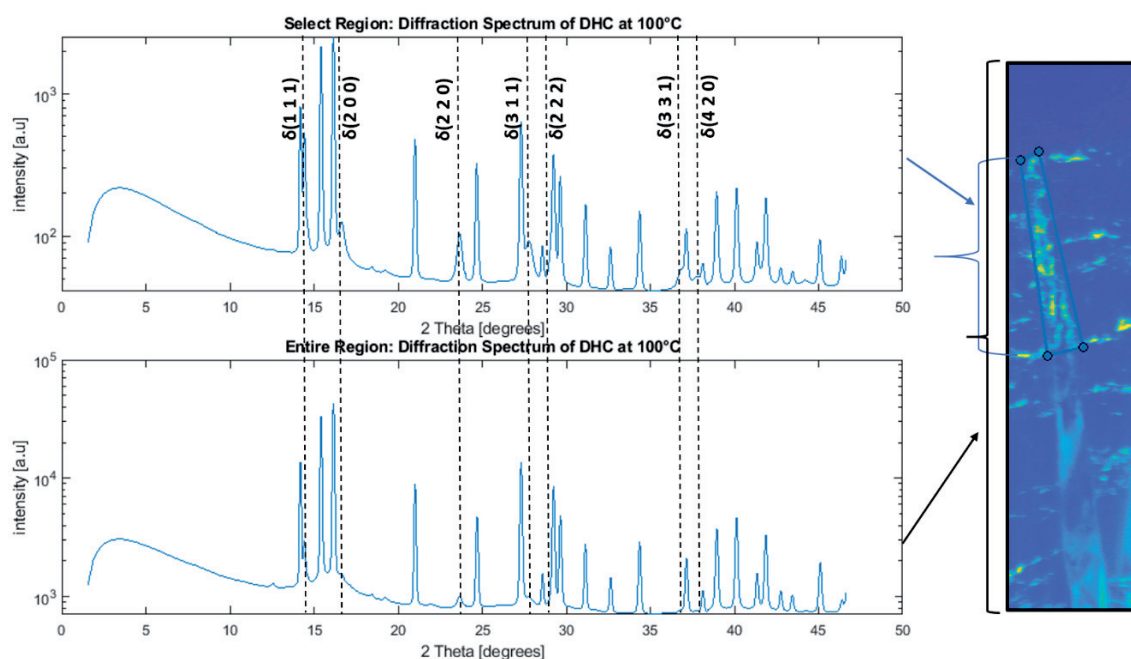
Figure 8.7: A diffraction pattern of a user selected ROI around the crack tip (top), and the integral diffraction pattern of the entire area imaged (bottom) displaying the differences in relative hydride signals.

Each peak was identified with its respective phase as seen in Figure 8.8. The figure shows that every significant peak was accounted for given the expected phases (zirconium, hydrides, oxide, and secondary phase precipitates)
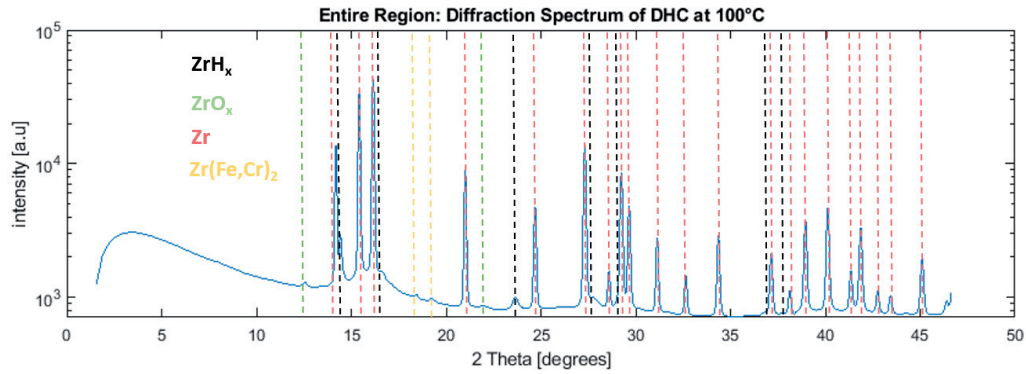
Figure 8.8: A detailed overview of the phases identified from significant peaks in the diffraction pattern.

8.5. X-ray diffraction phase maps

As previously described, a user-defined polygon was used to encompass a region that only included the hydride crack flanks and tip for the three samples studied. The resulting diffraction pattern is displayed above the images showing intensity of diffracted beam at 2θ angles corresponding to different zirconium hydride reflections (Figure 8.9 - Figure 8.11). The contrast in each of the images has been individually adjusted to highlight the peak identified, as some of the hydride peaks were more or less intense, while some were located within the skirt of a stronger peak creating a larger shoulder of the more intense peak. As a result, a weak intensity of the hydride phase was hidden by the background, while a hydride peak close to another more intense peak might have been blurred. Figures 8.9 and 8.10 present the hydride distribution obtained for the sample cracked at 100°C and 150°C, respectively.
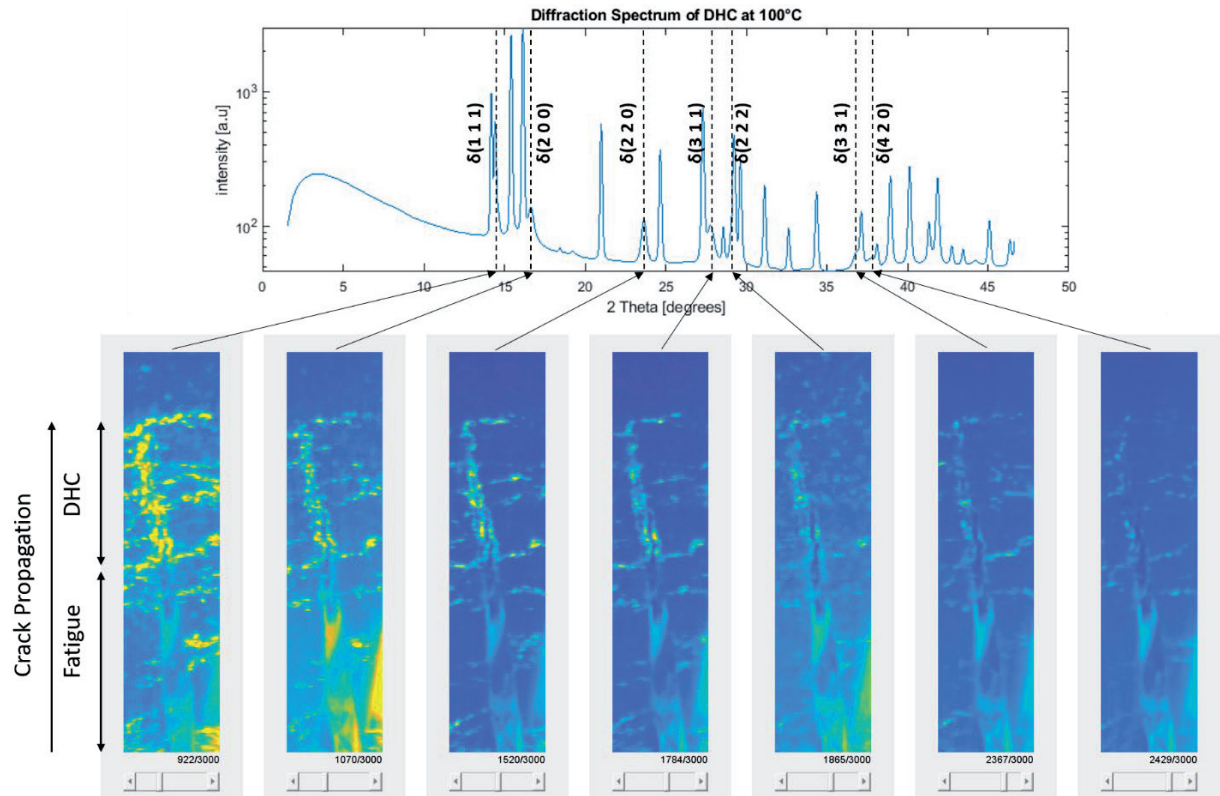
Figure 8.9: Above - the diffraction pattern of the ROI of the sample tested at 100°C. Below – the respective phase maps for each defined peak. The contrast scale had been adjusted for each map individually and should not be used to compare different planes to one another.
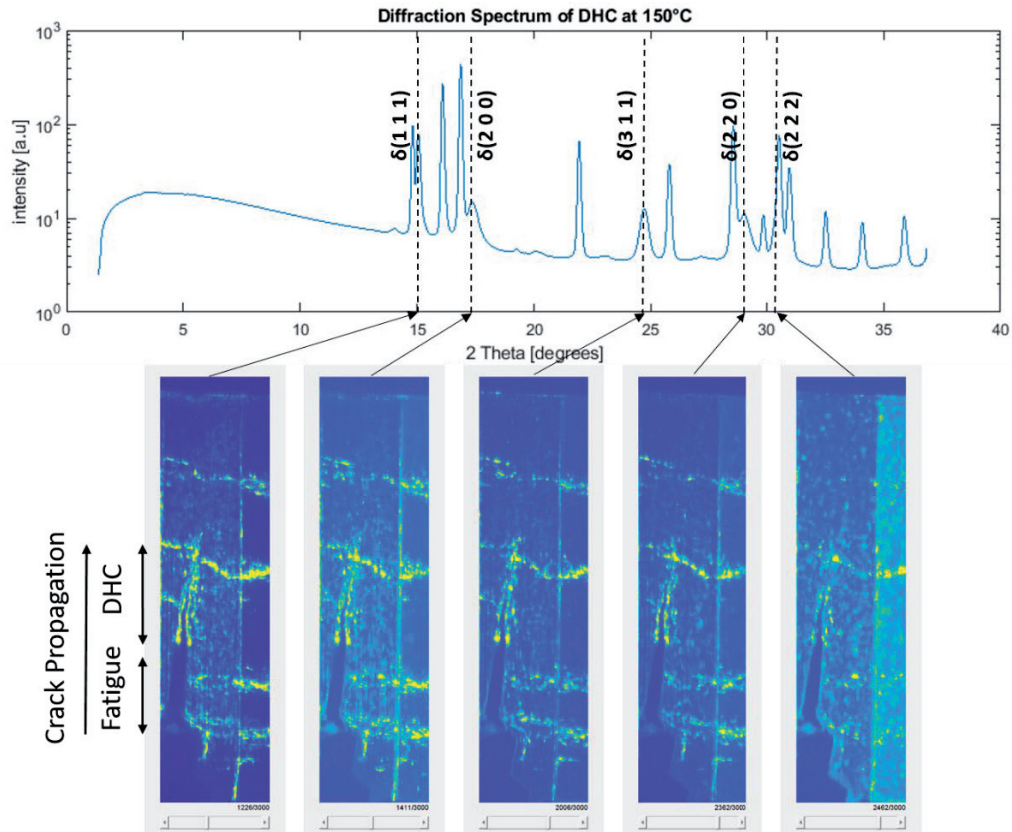
Figure 8.10: Above - the diffraction pattern of the ROI of the sample tested at 150°C. Below – the respective phase maps for each defined peak. In each image the edge of FIB polishing can be seen to the right of the crack and in the vertical position. This should not to be confused with the hydride at the crack flank. The contrast scale had been adjusted for each map individually and should not be used to compare different planes to one another.

Figure 8.11 illustrates the sample cracked at 320°C showing the hydride distribution around the crack flanks. It can be seen that hydrides have precipitated more significantly around the beginning phase of DHC compared to the tip of the crack. In addition, the hydrides precipitate in a much larger area compared to the other samples. Conversely, the 320°C sample does not show signs of circumferential hydrides in the region that has cracked.
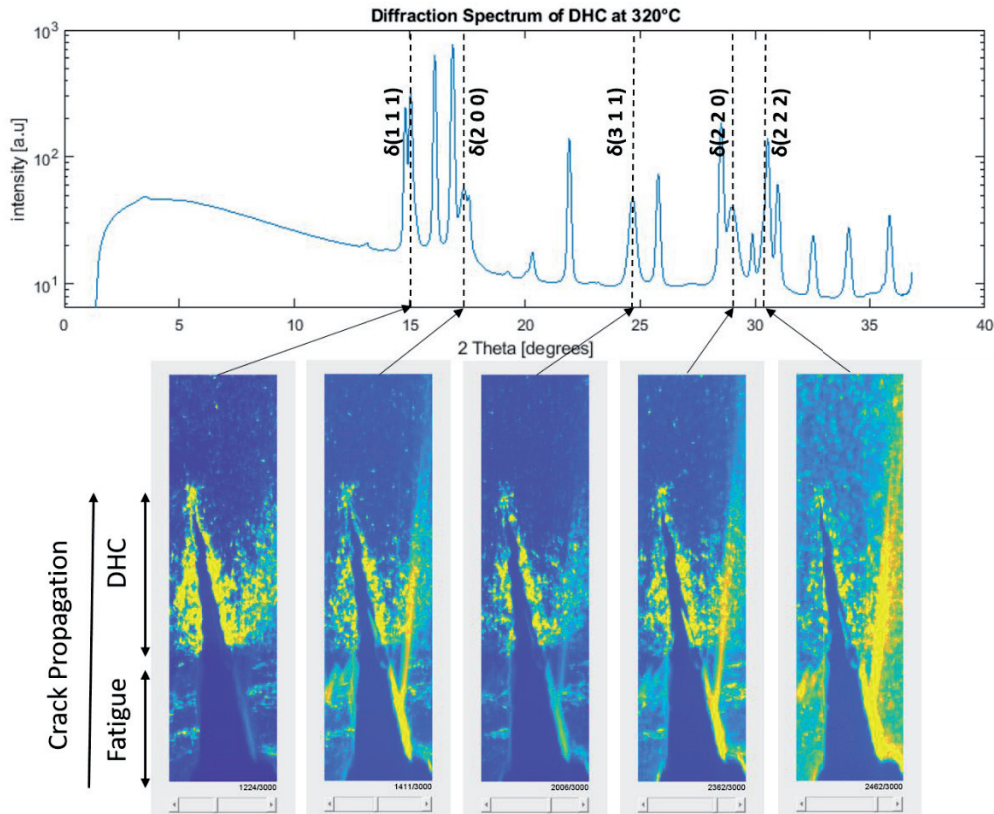
Figure 8.11: The diffraction pattern of the ROI of the sample tested at 320°C. Below – the respective phase maps for each defined peak. In each image, the edge of FIB polishing can be seen to the right of the crack and in the vertical position. This should not to be confused with the hydride at the crack flank. The contrast scale had been adjusted for each map individually and should not be used to compare different planes to one another.

8.5.1. Secondary phase precipitates

The ability to see the small (ten's of nm wide) SPP's within the diffraction pattern and diffraction intensity images highlights the resolution of the imaging, especially when the phases of interest, namely hydrides, are much larger than the SPP's.
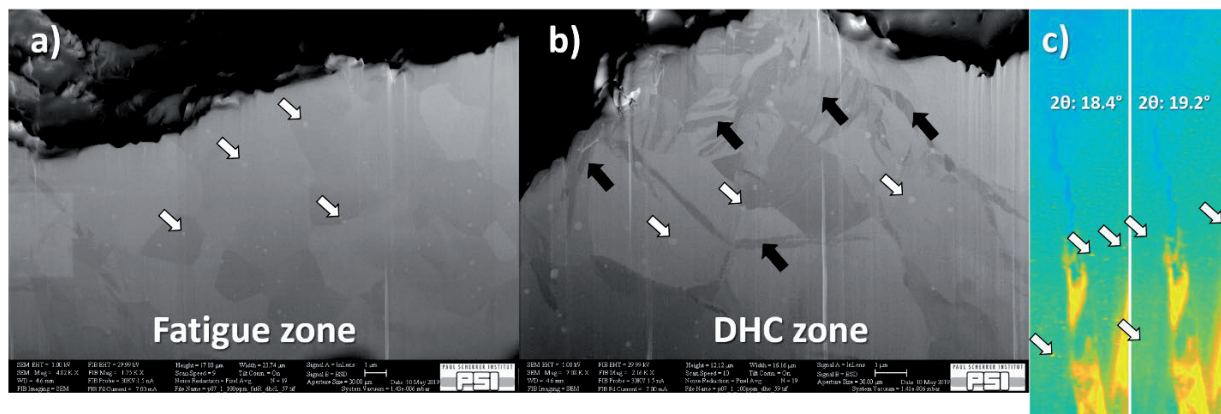
Figure 8.12: Cross-sections FIBed perpendicular to the fractured surface and parallel to the cracking direction. a) the fatigued zone. b) DHC zone. c) diffraction intensity phase maps shown in Figure 8.8 SPPs (white arrows) ranging from tens of nanometers can be seen along with precipitated DHC hydrides (black arrows).

8.5.2.   TOPAS curve fitting

The TOPAS software was utilized to fit models containing expected structures to the experimental diffraction patterns based on Rietveld refinement. The curve fitting provides various information, including the fraction of various phases based on relative intensities and allows to identify the Miller indices of a given reflection. Fitting the diffraction pattern is necessary to identify crystalline phases, especially in case of overlapping of peaks corresponding to different phases. TOPAS required the '.xy' data files containing the experimental XRD pattern, and '.cif' data files containing specific theoretical information about a given crystalline structure and the emission profile of the used X-ray beam. In the following Figure 8.13 an example of a curve fitting is shown. To be more accurate with curve fitting, a range of d-spacing was selected.
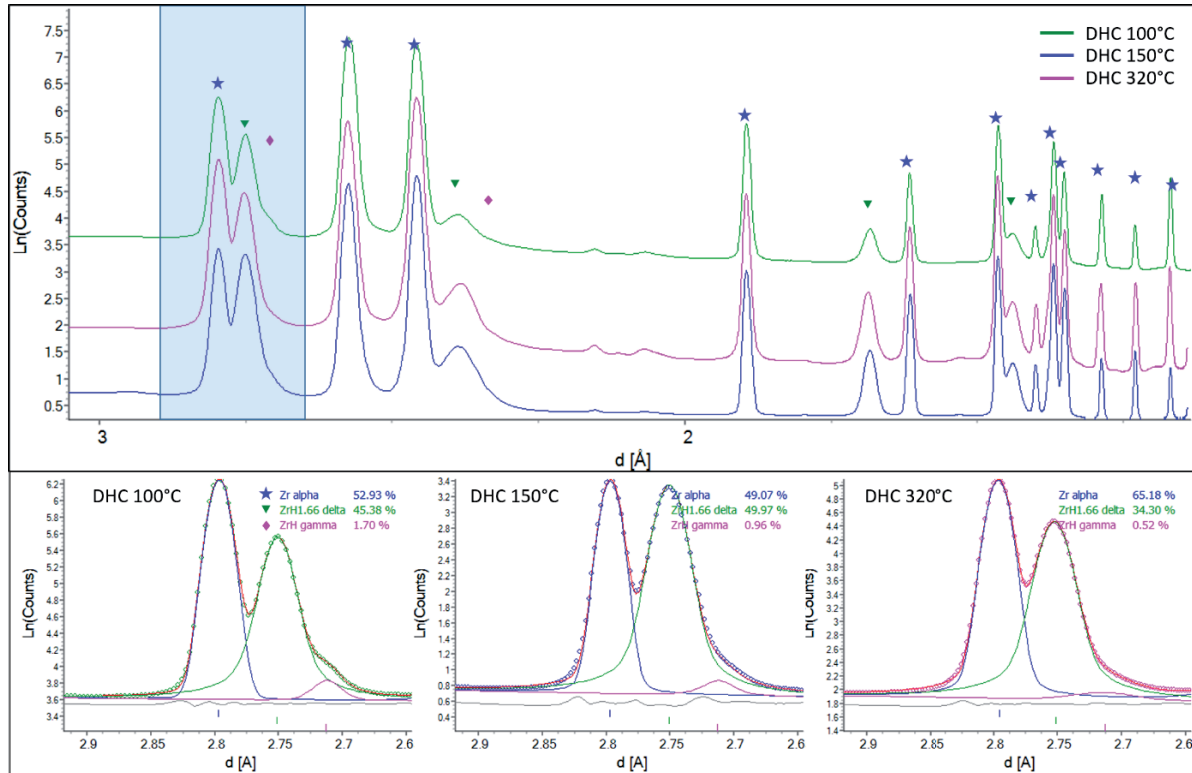
Figure 8.13: Above is the summary of the diffraction patterns of the three samples according the ROI as seen in Figure 8.7. Below are the fitted peaks of the (111) plane of the δ- and γ-hydride for a selected fitting range where dotted lines represent measured data that corresponds to the diffraction collection above.

The results of the fitting show that there are δ- and γ-hydride phases detected to different degrees in all three samples. However, it should be noted that the γ-hydride phase in the 320°C is near the undetectable range while it is clearly visible in the 100°C sample and somewhat in the 150°C sample.

8.6.   Discussion

8.6.1.   Phase identification

The diffraction pattern of each ROI was analyzed in detail such that each peak was identified. By analyzing all distinguishable signals, and fitting theoretical diffraction pattern, the certainty of identification was increased.

With a selected range of d-spacing, a more accurate curve fitting was created around the (111) plane of the γ- and δ-hydride phase. According to the curve fitting, the δ-hydride was the predominant phase around the DHC crack tip, while the γ-hydride phase did indeed become detectable, in low quantities, and at low temperatures. Considering the spatial resolution, while very high, might still be too low compared to what previous experiments have required to identify very small regions of the γ-hydrides which encapsulated δ-hydrides [45]. However, considering the comparable, but smaller, size of SPP's and the ability to locate them (Figure 8.12), one should be also able to expect high accuracy of relatively larger hydrides.

Some studies have reported dominating fractions of γ-hydrides which precipitated at lower temperatures or faster cooling rates [43]–[45], [140]. In the XRD studies, single peaks with low relative signals from relatively large X-ray beams in reflection mode have been analyzed. The EELS studies have shown in very small regions, at the atomic scale, single over-lapping peaks of gamma and delta. The work in this experiment does not support the findings of overwhelming ratios of γ-hydrides, as the volume of γ-hydrides might be so small that detection is inhibited. However, the findings do suggest that if there were γ-hydrides, they would not be in greater proportions than δ -hydrides as some literature suggests.

8.6.2.   Hydride distribution

It can be seen at the lower test temperatures (100°C and 150°C) that a very small hydride is sufficient to induce DHC showing signs of what a critically sized hydride might be at lower temperatures. Additionally, the hydrides appear to have fractured without growing excessively, as in the 320°C sample. As the speed of these two cracks were extremely slow compared to the 320°C sample, it can be inferred that the time to reach a critical sized hydride was much longer. The slow rate of propagation is likely due to the small source of hydrogen in solid solution, leading to lower hydrogen diffusion rates.

At higher temperatures (320°C), significantly higher amounts of hydrogen remain in solid solution, leading to a larger source of hydrogen for DHC. Additionally, the 320°C sample displays much larger volumes of hydride precipitation along the DHC crack flanks. From Figure 8.11, it can be seen that there is more than sufficient hydrogen diffusion towards the crack, even in excess, as the precipitation extends away from the crack flanks. The excessive precipitation hints at the rate of diffusion relative to the cracking speed. As the diffusion of hydrogen is dependent on stress in the DFM [54], it can be inferred that diffusion of hydrogen, at this temperature, is faster than cracking, in order to precipitate in excess at the onset of DHC (when cracking is slower or still within an incubation time). In other words, as crack propagation also results in a propagating stress field, stress relaxation at the preceding crack location occurs, resulting in arrest of hydrogen diffusion at the preceding location. As the speed of cracking is slightly increasing, the final hydride precipitate could be smaller than at the start when cracking was slower.

8.7.   Conclusion

The micro-XRD phase maps have very high resolution so that also SPP's can be identified and located. The γ-hydride could be detected at low testing temperatures indicating that it is a stable phase. However, the proportion of γ- to δ-hydride remained low. The technique has shown in high resolution the distribution and size of the precipitated hydrides along the crack flanks where the size of hydrides can be correlated to the temperature at which DHC occurred.

9. General discussion

In this chapter, a general discussion of the main findings is given and will be expanded to the impact on general DHC and hydride precipitation knowledge as well as will comment on the implications it has on spent fuel storage, handling and transportation.

9.1.   DHCV and neutron radiography

While literature provides numerous results for velocity measurements, there are few which have reported radial cracks in thin-walled fuel cladding. In this project the three-point bending achieves consistent radial outside-in DHC.

The results of DHCV measurements combined with the neutron radiography show the post-test hydride precipitation in relation to the velocity of the cracking. It is clear from the radiography results that the total diffusion of hydrogen, which has been interpreted from the hydride precipitation, is strongly linked to the total hydrogen concentration in solid solution regardless of a cracking. This can be seen particularly in the samples tested at 360°C and 410°C in the LK3 and LK3/L material where strong precipitation occurs regardless of limited or complete crack inhibition. It can also be seen that crack velocity at lower temperatures (below 300°C) is correlated to the rate of diffusion, following the Arrhenius law, while creep strongly inhibits the rate of cracking above 300°C despite the continuously increasing hydrogen diffusion. The combined effect of creep and DHC, which cannot be decoupled, has be named 'C-DHC'. The results of these combined effects give an insight into the behavior of SNF during storage conditions. One can imagine that stress risers in hot/fresh SNF can lead to high amounts of hydrogen diffusion and hydride precipitation without fracture. However, as the SNF cools, the cladding can be left with highly brittle locations of hydride clusters susceptible to fracture.

The comparison of the metallography, radiography, and hydrogen quantification has shown the influence of the stress field on the hydrogen diffusion pattern, which can be inferred from the precipitation patterns. The various micrographs suggest that hydrogen diffuses along the highest stress gradients as the 'butterfly' shape of the shear stress is depicted in the precipitation around the crack tip (specifically the 2.0 mm sample at 360°C). Along with the micrographs, the hydrogen quantification shows that the hydrogen concentration gradient is continuously decreasing with distance from the crack tip as expected from the diffusion first model (DFM), rather than undulated as might be expected from the precipitation first model (PFM) where a concentration gradient is the primary driving force of diffusion. These results rather support the DFM model, considering the high spatial resolution of all imaging and the hydrogen quantification.

9.2. Threshold stress intensity factor of DHC

As mentioned in the respective chapter, the K_{IH} value is likely the most important property of DHC to consider in the context of transportation and intermediate dry storage of SNF. All other variables can be considered as given when assessing the risk of triggering DHC in SNF. In other words, as soon as corrosion takes place, a sufficient amount of hydrogen will be taken up to suffice as a source for DHC. Additionally, there will always be a given heat source from the decay heat of SNF leading to increased cladding temperatures. That leaves stress as the limiting factor for DHC. As soon as the stress is sufficient in SNF, DHC will occur because sufficient heat and hydrogen are 'given' factors of DHC.

In this study, the minimum K_{IH} value for Zircaloy-2 fuel cladding without an inner liner was around 6 MPavm. When considering the range of values given for zirconium alloys in literature, 6 MPavm is nearly in the middle. The minimal value however has been shown to be dependent on the temperature and hydrogen concentration, where creep and solubility limits play a role. It was also shown that creep begins to inhibit DHC above 300°C, while at low hydrogen

concentrations the effects of the hydrogen solubility became apparent at temperatures below those at which creep starts to act. While the details of temperature and solubility help to understand the fundamental aspects of DHC, the minimum values of K_{IH} will impact the limits of tolerable defects for transportation and storage of SNF.

9.3.   γ-hydride stability

Literature has reported on many attempts to discover the stability state of the γ-hydride phase. Reported techniques have included EELS, and XRD in a lab and synchrotron setting. Synchrotron experiments have also included in-situ thermomechanical loading in an attempt to highlight how the zirconium hydride structure responds to stresses. In this study, DHC cracks are mapped with XRD using a roughly one square micron X-ray beam. First, the DHC-responsible hydrides were identified, and second, the γ-hydride phase was determined to be a stable phase at low temperatures (100°C and 150°C) of DHC propagation, while it remains undetected in high temperature (320°C) DHC cracks. The results add another piece of information to the understanding of hydride precipitation.

In addition to phase identification, the DHC cracks were mapped with high-spatial resolution showing the area of hydrides that populated the region around a crack. The low temperatures samples indicated a very small hydride cluster that has cracked, while at high temperatures, much larger clusters of hydrides precipitate during DHC. These high-resolution results provide potential information about the critically sized hydride for DHC propagation at different temperatures.

The improvement in the fundamental understanding of hydride precipitation can lead to better knowledge of how SNF should be transported and stored. Such fundamental knowledge could possibly lead to material design improvements when considering the triggers and mechanisms required for precipitation of various phases. If there is a difference in mechanical properties of

γ- and δ-hydrides, the DHC temperature needs to be considered, as the consequences for storage, handling and transportation may differ.

9.4. DHC in irradiated material

In order to understand the irradiation damage effects on DHC, the comparison between unirradiated and irradiated material is necessary. In this project, a number of irradiated and unirradiated LK3/L samples were tested. Given the irradiated material came from a rod with an average burnup of 57.5 MWd/kgU, the material was ideal for investigating the impact of irradiation damage.

While some comparisons could be made from the metallography analysis, a significant amount of the information is still missing due to the technical difficulties experienced during irradiated sample preparation. Nevertheless, a thorough comparison using neutron radiography was performed between the irradiated and unirradiated material. The most obvious difference was between the multitude of cracks seen in the irradiated samples, where each of the unirradiated samples exhibited a single crack. While the conditions for comparison are not perfectly equivalent, i.e. the lacking notch of the irradiated material, important points can be learned from the tests. The number of cracks, which initiate in the irradiated samples, shows the effect of the undulated outer surface caused by oxidation. The undulations created stress concentration points, which led to an increase in cracking initiation sites during fatigue pre-cracking. The subsequent DHC simply proceeded from each of the pre-cracks. Lastly, the direction of the cracking in the irradiated material was also less uniform indicating the path of hydride fracture could have been affected by the complex stress field, which consisted of multiple crack sites.

In most of the metallography images of the irradiated samples, the complete cracking and hydride overview was difficult to see due to preparation problems and an insufficient number of polished cross-sections. However, important observations were still made showing how and

where the hydrides in the irradiated material orient themselves in the radial direction. Specifically, the hydrides within the liner and in the outer half of the matrix have oriented themselves radially, while the inner half remains either circumferential or seemingly unaffected. Considering the knowledge of the effect of tensile and compressive stress on the hydride orientation, the orientation in the liner is extremely interesting due to the fact that it is under compressive stress, yet still forms radially oriented hydrides. It has been postulated that the liner could enhance the protection against hydride cracking as it accumulates hydrogen and subsequent hydrides in a circumferential orientation in the absence of stress. However, it is clearly observed that even under compressive stress, the hydrides in the liner are oriented radially. It can also be qualitatively seen that the liner hydrides are more significantly radially oriented than the outer tensile-stressed matrix. Such level of radial hydride orientation creates pathways that are highly susceptible to fracture. The information is important in the consideration of how helpful, if at all, the inner liner is at securing the cladding mechanical integrity in case of DHC or in case of long cracks with their tips close to the cladding liner interface.

10. Conclusions

In this chapter, each of the main experiments are briefly recapitulated, followed by the main findings and the resulting conclusions..

10.1. Three-point bending of cladding

The foundation of this project was based upon the novel experimental method created specifically for testing fuel cladding in a realistic cracking direction and orientation. The three point bending test allowed for an outside-in radial propagation with a crack oriented axially respective to the cladding tube. Additionally, the test setup allowed for practical testing of irradiated material. The following points summarize the three point bending test:

- A specifically developed notching device allowed preparing reliably exact notches also for irradiated samples under hotcell conditions.
- Consistent testing and stable crack propagation of thin-walled fuel cladding specimens was achieved with the testing fixture, setup, and parameters.
- Irradiated material testing of thin-walled fuel cladding specimens was achieved allowing for direct comparison of unirradiated and irradiated material.
- The 'fixed' rollers of the test fixture allowed for high temperature testing.

10.2. DHC velocity

With the novel three-point bending experiment, DHC velocity (DHCV) tests were performed. The first tests paved the way to defining ideal testing parameters including, heating, loading, and displacement limits. With these parameters defined, more complicated tests, such as threshold stress intensity factor testing, and irradiated material testing, could be achieved. For the DHCV property itself, experiments with three different Zicaloy-2 (LK3, LK3/L, and SINQ

target rod) materials at various hydrogen concentrations and test temperatures were performed. The following points highlight the main findings and conclusions of these tests:

- The DHCV for all alloys follows the Arrhenius law up to 300°C. Thereafter creep plays a prominent role, along with solubility limits, leading to a rapid decrease in the measured velocity in addition to a much greater scatter.

- The LK3 material shows consistent velocities at lower temperatures, while not enough data points are available for high temperature comparison.

- The LK3/L (LK3 material containing an inner more pure Zircaloy liner) material fractures consistently slower than the LK3 material at all concentrations and temperatures. The effect of the inner liner absorbing large amounts of hydrogen results in hydrogen-depletion of the matrix where DHC occurs. It is presumed that the hydrogen-depleted matrix effectively leads to a reduced source of hydrogen for diffusion during DHC causing slower crack propagation. As discussed in the following section, hydrogen quantification results from neutron radiography verify the lower amounts of hydrogen at the crack tip of the LK3/L material compared to equivalent LK3 tests.

- The DHCV of the SINQ target rod material was consistently higher than of the LK3 and LK3/L material, however at incomparably high hydrogen concentrations and temperatures.

10.3. DHC Threshold stress intensity factor

Stress is considered the most important factor for DHC onset as it can be assumed that all other factors, such as heat and hydrogen, will be more than sufficient for DHC in SNF. Again, the novel three-point bending test was employed to determine the DHC threshold stress intensity factor, K_{IH}. The material used in these tests was Zircaloy-2 (LK3) charged with two concentrations of hydrogen (155 wppm and 305 wppm H). With a slight variation in the testing

parameters, specifically the unloading rate during propagation, stable DHC cracking was arrested leading to K_{IH}. Fractography and finite element modeling (FEM) was then used to back-calculate the stress intensity factor. The main findings of these tests and calculations are the following:

- The hydrogen solubility affects the temperature at which the most ideal, or minimum K_{IH}, occurs.

- DHC at temperatures above 300°C are affected by creep, which leads to a combined cracking phenomenon that cannot be decoupled. It is newly defined in this work as creep delayed hydride cracking (C-DHC).

- FEM is able to confidently back-calculate the K_I of cracked samples that were not strongly blunted, i.e. samples tested below 300°C where creep did not blunt the crack tip. The minimum K_{IH} that was back-calculated, was around 6 MPa√m for both 155 and 305 wppm H concentrations. The minimum K_{IH} occurred at lower temperatures for the 155 wppm H sample set around 270°C, and 290°C for the 305 wppm H sample set.

10.4. Neutron radiography

Neutron radiography performed at the POLDI beamline of the SINQ was utilized to observe the DHC cracks nondestructively and quantify the hydrogen around the crack tip. A number of samples (LK3, LK3/L, and SINQ target rod material) from the DHCV velocity tests were selected for radiography because of their ideal properties like high hydrogen concentration and wide test temperature spectrum. Additionally, irradiated material was analyzed using neutron radiography due to the need of nondestructive inspection. The following conclusions were drawn from the neutron radiography experiments.

- Hydrogen concentrations increase around the DHC tip with increasing test temperature.

- The liner depletes the matrix of hydrogen, however sufficient hydrogen diffusion occurs, enabling DHC cracking to occur.

- Neutron radiography results display advantages of non-destructive testing especially through analysis of irradiated materials. Cracks can be observed and hydrogen concentrations can be analyzed where metallography is insufficient.

- Irradiated LK3/L material shows preference of hydrogen diffusion and precipitation in the liner, however at less significant levels indicating that the irradiation damage has influenced the kinetics of hydrogen diffusion. Little to no hydrogen diffusion towards the crack tip occurred in the irradiated SINQ target rod material.

- Neutron radiography combined with metallography shows that hydrogen will continue to diffuse and precipitate around the crack tip regardless of crack propagation, i.e. when creep inhibits DHC. The crack velocity appears not to be strongly correlated with the amount of available hydrogen in solid solution at higher temperatures, rather with the amount of creep-induced crack tip blunting.

10.5. Micro-XRD phase mapping

The XRD measurements at the μ-XAS beamline of the SLS were performed after the DHC test to identify the hydrides responsible for DHC at various test temperatures. The micron sized beam and sample rasterization made possible to create diffraction intensity phase maps. The main findings of the phase maps are the following:

- The δ-hydride was the most detectable phase at the tip of each arrested crap tip while the γ-hydride was detectable in the samples tested at the lower temperatures of 100°C and 150°C. The detection of the γ-phase indicates that it is a stable phase under the given temperature and stress conditions during and after cracking.

- The samples tested at 320°C showed very little signs of detectable γ-hydrides.

- The phase maps describe in high resolution the volume of hydride precipitation around the crack tip where the higher temperatures lead to increased precipitation as seen also at relatively lower resolution in the neutron radiographs.

10.6. Future work

This study open more doors than it closes due to interesting and promising results. The following points summarize which immediate tests and improvements can be made for the continuation of this work.

- Throughout the DHC velocity tests, it can be seen that the velocity of each sample set extends differently to the ends of the temperature spectrum. Additionally, the hydrogen concentrations of each set are rather similar to one another considering the range of SNF concentrations. Therefore, it is suggested that the temperature range should be extended equally to highlight the Arrhenius trend, as well as upper temperature drop off. It would also be of interest to expand the hydrogen concentration differences between sets. This should be done by reducing the minimum hydrogen concentration of the samples tested. The reduction of hydrogen will give a greater chance to highlight the effect of the solubility limits during DHC.

- Similarly, the K_{IH} experiments could be extended to lower concentrations of hydrogen. Again, this will highlight the effect of the hydrogen solubility limit on the K_{IH} as tests could be performed at temperatures well above the TSSP or TSSD while remaining below the creep limit, i.e. 300°C.

- From the fractography, crack fronts generally appear symmetrical, however at a more detailed glance, it can be seen that many samples have non-symmetric offsets of tilt with respect to the centerline of the sample. As the growth of the crack is determined by many factors, including specimen dimensions, hydrogen distribution, etc., it is proposed that the simplest factor should be explored, i.e. the sample dimensions.

Exploring the geometrical effect could be a valuable study to increase the consistency of symmetric crack propagation.

- The effect of the inner liner was explored as the LK3/L material contained an inner liner and the testing setup allowed for an outside-in crack propagation. However, there are cladding materials that contain an outer liner, such as those used in pressurized water reactors. The tests could quickly be adapted to explore the effect of such materials, even in the inside out direction.

- The irradiated material of this study was minimally analyzed due to the technical difficulties during sample polishing. Simply stated, the samples should be metallographically further analyzed.

- Neutron and X-ray radiography experiments have proven to be highly capable with high-spatial resolution. Such experiments can be immediately implemented on samples that have undergone other various thermomechanical treatments.

- Experimental results obtained create a foundation for various types of modeling such as hydrogen diffusion and precipitation. The K_{IH} and velocity tests add details for multi-physics modeling. This work should be directly applied to creating new modeling of DHC.

References

[1] G. Adrian, "Key World Energy Statistics 2013," pp. 1–82, 2021.

[2] M. William, "Nuclear Power," *Encylopedia Britanica*. 2021, [Online]. Available: https://www.britannica.com/technology/nuclear-power.

[3] Enusa, "Fabrication." https://www.enusa.es/en/fabrication/ (accessed Mar. 23, 2022).

[4] F. C. Olds, "Nuclear Fuel Cycles.," *Power Eng. (Barrington, Illinois)*, vol. 87, no. 10, pp. 42–50, 1983, doi: 10.1201/9781315373829-17.

[5] S. Kass, "Hydrogen Pickup in Various Zirconium Alloys during Corrosion Exposure in High-Temperature Water and Steam," *J. Electrochem. Soc.*, vol. 107, no. 7, p. 594, 1960, doi: 10.1149/1.2427781.

[6] International Atomic Energy Agency, "Waterside corrosion of zirconium alloys in nuclear power plants," *IAEA-TECDOC-996*, 1998, doi: IAEA-TECDOC-996.

[7] D. C. Crawford, *Introduction to fuel cycle front end: From mining through utilization*, vol. 2. Elsevier, 2021.

[8] Swiss Federal Office of Energy, "Sectoral plan for deep geological repositories: Conceptual part," Bern, 2008.

[9] A. T. Motta *et al.*, "Hydrogen in zirconium alloys: A review," *J. Nucl. Mater.*, vol. 518, pp. 440–460, 2019, doi: 10.1016/j.jnucmat.2019.02.042.

[10] W. Gong *et al.*, "Hydrogen diffusion and precipitation in duplex zirconium nuclear fuel cladding quantified by high-resolution neutron imaging," *J. Nucl. Mater.*, vol. 526, p. 151757, 2019, doi: 10.1016/j.jnucmat.2019.151757.

[11] R. Dutton, K. Nuttall, M. P. Puls, and L. A. Simpson, "Mechanisms of Hydrogen Induced Delayed Cracking in Hydride Forming Materials.," *Met. Trans A*, vol. 8 A, no. 10, pp. 1553–1562, 1977, doi: 10.1007/BF02644858.

[12] E. C. W. Perryman, "Pickering pressure tube cracking experience," *Nucl. Energy*, vol. 17, no. 2, pp. 95–105, 1978.

[13] "DELAYED HYDRIDE CRACKING OF ZIRCONIUM ALLOY FUEL CLADDING," *IAEA - TECDOC - 1649*, 2010.

[14] IAEA - International Atomic Energy Agency, "Delayed hydride cracking in zirconium alloys in pressure tube nuclear reactors IAEA-TECDOC-1410," *October*, no. October, p. 43, 2004.

[15] S. Kass, "The Development of the Zircaloys," *Corros. Zircon. Alloy.*, pp. 3-3–25, 1964, doi: 10.1520/STP47070S.

[16] C. Proff, "Microstructual aspects of the oxidation of zirconium," Universite de Grenoble, 2011.

[17] A. T. Motta, A. Couet, and R. J. Comstock, "Corrosion of Zirconium Alloys Used for Nuclear Fuel Cladding," *Annu. Rev. Mater. Res.*, vol. 45, no. 1, pp. 311–343, 2015, doi: 10.1146/annurev-matsci-070214-020951.

[18] P. M. Kelly and R. G. Blake, "The characterization of dislocation loops in neutron irradiated zirconium," *Philos. Mag.*, vol. 28, no. 2, pp. 415–426, 1973, doi: 10.1080/14786437308217463.

[19] F. A. Nichols, "Theory of the creep of zircaloy during neutron irradiation," *J. Nucl. Mater.*, vol. 30, no. 3, pp. 249–270, 1969, doi: 10.1016/0022-3115(69)90241-4.

[20] A. D. Brailsford and R. Bullough, "Irradiation creep due to the growth of interstitial loops," *Philos. Mag.*, vol. 27, no. 1, p. 49, 1973, doi: 10.1080/14786437308228913.

[21] C. Lemaignan and A. Motta, "Zirconium Alloys in Nuclear Applications, in: Materials Science and Technology: A Comprehensive Treatment," vol. 10B, 1994.

[22] M. Joyce, *Nuclear Engineering: A Conceptual Introduction to Nuclear Power*. Butterworth-Heinemann, 2018.

[23] S. N. Ahmed, *Properties and sources of radiation*. 2015.

[24] B. Ensor, A. T. Motta, A. Lucente, J. R. Seidensticker, J. Partezana, and Z. Cai, "Investigation of breakaway corrosion observed during oxide growth in pure and low alloying element content Zr exposed in water at 360°C," *J. Nucl. Mater.*, vol. 558, p. 153358, 2022, doi: 10.1016/j.jnucmat.2021.153358.

[25] B. E. Warren, V. A. Dale, and E. L. White, "Hydrogen Pickup During Aqueous Corrosion of Zirconium Alloys," *Corrosion*, vol. 17, 1961.

[26] X. Wang, M. J. Zheng, I. Szlufarska, and D. Morgan, "Continuum model for hydrogen pickup in zirconium alloys of LWR fuel cladding," *J. Appl. Phys.*, vol. 121, no. 13, 2017, doi: 10.1063/1.4979472.

[27] M. Tupin *et al.*, "Hydrogen diffusion process in the oxides formed on zirconium alloys during corrosion in pressurized water reactor conditions," *Corros. Sci.*, vol. 116, pp. 1–13, 2017, doi: 10.1016/j.corsci.2016.10.027.

[28] B. Cox and Y. M. Wong, "Hydrogen uptake micro-mechanism for Zr alloys," *J. Nucl. Mater.*, vol. 270, no. 1, pp. 134–146, 1999, doi: 10.1016/S0022-3115(98)00898-8.

[29] M. S. Veshchunov and A. V. Berdyshev, "Modelling of hydrogen absorption by zirconium alloys during high temperature oxidation in steam," *J. Nucl. Mater.*, vol. 255, no. 2–3, pp. 250–262, 1998, doi: 10.1016/S0022-3115(98)00018-X.

[30] G. M. Hood, "Point defect diffusion in α-Zr," *J. Nucl. Mater.*, vol. 159, no. C, pp. 149–175, 1988, doi: 10.1016/0022-3115(88)90091-8.

[31] E. Lacroix, A. T. Motta, and J. D. Almer, "Experimental determination of zirconium hydride precipitation and dissolution in zirconium alloy," *J. Nucl. Mater.*, vol. 509, pp. 162–167, 2018, doi: 10.1016/j.jnucmat.2018.06.038.

[32]   J. Desquines *et al.*, "Influence of temperature and hydrogen content on stress-induced radial hydride precipitation in Zircaloy-4 cladding," *J. Nucl. Mater.*, vol. 453, no. 1–3, pp. 131–150, 2014, doi: 10.1016/j.jnucmat.2014.06.049.

[33]   R. K. Sharma, A. K. Bind, G. Avinash, R. N. Singh, A. Tewari, and B. P. Kashyap, "Effect of radial hydride fraction on fracture toughness of CWSR Zr-2.5%Nb pressure tube material between ambient and 300 °C temperatures," *J. Nucl. Mater.*, vol. 508, pp. 546–555, 2018, doi: 10.1016/j.jnucmat.2018.06.003.

[34]   P. Kreyns, W. Bourgeois, C. White, P. Charpentier, B. Kammenzind, and D. Franklin, "Embrittlement of Reactor Core Materials," *Zircon. Nucl. Ind. Elev. Int. Symp.*, pp. 758-758–25, 1996, doi: 10.1520/stp16200s.

[35]   M. P. Puls, S.-Q. Shi, and J. Rabier, "Experimental studies of mechanical properties of solid zirconium hydrides," *J. Nucl. Mater.*, vol. 336, no. 1, pp. 73–80, Jan. 2005, doi: 10.1016/J.JNUCMAT.2004.08.016.

[36]   M. P. Puls, *The Effect of Hydrogen and Hydrides on the Integrity of Zirconium Alloy Components: Delayed Hydride Cracking*. Springer, 2012.

[37]   C. E. Coleman and D. Hardie, "The hydrogen embrittlement of zirconium in slow-bend tests," *J. Nucl. Mater.*, vol. 19, no. 1, pp. 1–8, 1966, doi: 10.1016/0022-3115(66)90123-1.

[38]   D. Hardie, "The influence of the matrix on the hydrogen embrittlement of zirconium in bend tests," *J. Nucl. Mater.*, vol. 42, no. 3, pp. 317–324, 1972, doi: 10.1016/0022-3115(72)90082-7.

[39]   K. G. Barraclough and C. J. Beevers, "Some observations on the deformation characteristics of bulk polycrystalline zirconium hydrides - Part 1 The deformation and fracture of hydrides based on the δ-phase," *J. Mater. Sci.*, vol. 4, no. 6, pp. 518–525, 1969, doi: 10.1007/BF00550212.

[40]   S. S. SIDHU, N. S. S. MURTHY, F. P. CAMPOS, and D. D. ZAUBERIS, "Neutron and X-Ray Diffraction Studies of Nonstoichiometric Metal Hydrides," pp. 87–98, 1963, doi: 10.1021/ba-1964-0039.ch008.

[41]   Z. Zhao *et al.*, "Characterization of zirconium hydrides and phase field approach to a mesoscopic-scale modeling of their precipitation," *J. ASTM Int.*, vol. 5, no. 3, 2008, doi: 10.1520/JAI101161.

[42]   Z. Wang *et al.*, "Observations of temperature stability of γ-zirconium hydride by high-resolution neutron powder diffraction," *J. Alloys Compd.*, vol. 661, pp. 55–61, 2016, doi: 10.1016/j.jallcom.2015.11.187.

[43]   E. Tulk, M. Kerr, and M. R. Daymond, "Study on the effects of matrix yield strength on hydride phase stability in Zircaloy-2 and Zr 2.5 wt% Nb," *J. Nucl. Mater.*, vol. 425, no. 1–3, pp. 93–104, 2012, doi: 10.1016/j.jnucmat.2011.10.051.

[44]   C. E. Coleman, G. A. McRae, A. Buyers, and S. Hanlon, "Gamma-zirconium hydride on DHC fracture surfaces is a legitimate stable phase, not a metastable phase," *J. Nucl.*

Mater., vol. 548, pp. 1–5, 2021, doi: 10.1016/j.jnucmat.2021.152839.

[45]   A. T. W. Barrow, A. Korinek, and M. R. Daymond, "Evaluating zirconium-zirconium hydride interfacial strains by nano-beam electron diffraction," *J. Nucl. Mater.*, vol. 432, no. 1–3, pp. 366–370, 2013, doi: 10.1016/j.jnucmat.2012.08.003.

[46]   L. Lanzani and M. Ruch, "Comments on the stability of zirconium hydride phases in Zircaloy," *J. Nucl. Mater.*, vol. 324, no. 2–3, pp. 165–176, Jan. 2004, doi: 10.1016/J.JNUCMAT.2003.09.013.

[47]   J. H. Root, W. M. Small, D. Khatamian, and O. T. Woo, "Kinetics of the δ to γ zirconium hydride transformation in Zr-2.5Nb," *Acta Mater.*, vol. 51, no. 7, pp. 2041–2053, 2003, doi: 10.1016/S1359-6454(03)00004-1.

[48]   M. A. Vicente Alvarez, J. R. Santisteban, G. Domizzi, and J. Almer, "Phase and texture analysis of a hydride blister in a Zr-2.5%Nb tube by synchrotron X-ray diffraction," *Acta Mater.*, vol. 59, no. 5, pp. 2210–2220, 2011, doi: 10.1016/j.actamat.2010.12.024.

[49]   D. O. Northwood, "Gamma and delta hydrides in zirconium alloys," *J. Less-Common Met.*, vol. 48, no. 1, pp. 173–175, 1976, doi: 10.1016/0022-5088(76)90243-5.

[50]   M. S. Blackmur *et al.*, "Zirconium hydride precipitation kinetics in Zircaloy-4 observed with synchrotron X-ray diffraction," *J. Nucl. Mater.*, vol. 464, pp. 160–169, 2015, doi: 10.1016/j.jnucmat.2015.04.025.

[51]   M. S. Blackmur *et al.*, "Strain evolution during hydride precipitation in Zircaloy-4 observed with synchrotron X-ray diffraction," *J. Nucl. Mater.*, vol. 474, pp. 45–61, 2016, doi: 10.1016/j.jnucmat.2016.01.039.

[52]   D. O. Northwood and U. Kosasih, "Hydrides and delayed hydrogen cracking in zirconium and its alloys," *Int. Met. Rev.*, vol. 28, no. 1, pp. 92–121, 1983, doi: 10.1179/imtr.1983.28.1.92.

[53]   C. J. Simpson and C.E.Ells, "Delayed Hydrogen Embrittlement in Zr-2.5 wt % Nb," *J. Nucl. Mater.*, vol. 52, pp. 289–295, 1974.

[54]   G. A. McRae, C. E. Coleman, and B. W. Leitch, "The first step for delayed hydride cracking in zirconium alloys," *J. Nucl. Mater.*, vol. 396, no. 1, pp. 130–143, 2010, doi: 10.1016/j.jnucmat.2009.08.019.

[55]   Y. S. Kim, "Driving force for delayed hydride cracking of zirconium alloys," *Met. Mater. Int.*, vol. 11, no. 1, pp. 29–38, 2005, doi: 10.1007/BF03027481.

[56]   M. P. Puls, "Review of the thermodynamic basis for models of delayed hydride cracking rate in zirconium alloys," *J. Nucl. Mater.*, vol. 393, no. 2, pp. 350–367, 2009, doi: 10.1016/j.jnucmat.2009.06.022.

[57]   L. A. Simpson and M. P. Puls, "The effects of stress, temperature and hydrogen content on hydride-induced crack growth in Zr-2.5 Pct Nb," *Metall. Trans. A*, vol. 10, no. 8, pp. 1093–1105, 1979, doi: 10.1007/BF02811655.

[58]   Y. S. Kim, "Comments on the Dutton-Puls model: Temperature and yield stress

dependences of crack growth rate in zirconium alloys," *Mater. Sci. Eng. A*, vol. 527, no. 29–30, pp. 7480–7483, 2010, doi: 10.1016/j.msea.2010.07.100.

[59]   Y. S. Kim, S. J. Kim, and K. S. Im, "Delayed hydride cracking in Zr-2.5Nb tube with the cooling rate and the notch tip shape," *J. Nucl. Mater.*, vol. 335, no. 3, pp. 387–396, 2004, doi: 10.1016/j.jnucmat.2004.07.046.

[60]   Y. S. Kim, K. S. Kim, and Y. M. Cheong, "Delayed hydride crack velocity of zirconium alloys with the direction of an approach to temperature," *J. Nucl. Sci. Technol.*, vol. 43, no. 9, pp. 1120–1127, 2006, doi: 10.1080/18811248.2006.9711203.

[61]   Y. S. Kim and S. S. Park, "Stage I and II behaviors of delayed hydride cracking velocity in zirconium alloys," *J. Alloys Compd.*, vol. 453, no. 1–2, pp. 210–214, 2008, doi: 10.1016/j.jallcom.2006.11.197.

[62]   Y. S. Kim, "Temperature dependency of delayed hydride cracking velocity in Zr–2.5 Nb tubes," *Mater. Sci. Eng. A*, vol. 468, pp. 281–287, 2007, doi: 10.1016/j.msea.2006.09.123.

[63]   Y. S. Kim, S. B. Ahn, and Y. M. Cheong, "Precipitation of crack tip hydrides in zirconium alloys," *J. Alloys Compd.*, vol. 429, no. 1–2, pp. 221–226, 2007, doi: 10.1016/j.jallcom.2006.09.034.

[64]   Y. S. Kim, "Hydride reorientation and delayed hydride cracking of spent fuel rods in dry storage," *Metall. Mater. Trans. A Phys. Metall. Mater. Sci.*, vol. 40, no. 12, pp. 2867–2875, 2008, doi: 10.1007/s11661-009-0044-6.

[65]   Y. S. Kim and A. Grybenas, "Effect of load ratio and hydrogen concentration on the crack growth rate in Zr-2.5Nb tubes," *Mater. Sci. Eng. A*, vol. 520, no. 1–2, pp. 147–152, 2009, doi: 10.1016/j.msea.2009.05.054.

[66]   A. M. Alvarez Holston and J. Stjärnsäter, "On the effect of temperature on the threshold stress intensity factor of delayed hydride cracking in light water reactor fuel cladding," *Nucl. Eng. Technol.*, vol. 49, no. 4, pp. 663–667, 2017, doi: 10.1016/j.net.2017.04.002.

[67]   T. Kubo, Y. Kobayashi, and H. Uchikoshi, "Measurements of delayed hydride cracking propagation rate in the radial direction of Zircaloy-2 cladding tubes," *J. Nucl. Mater.*, vol. 427, no. 1–3, pp. 18–29, 2012, doi: 10.1016/j.jnucmat.2012.04.012.

[68]   S. Sunil, A. Gopalan, A. K. Bind, R. K. Sharma, T. N. Murty, and R. N. Singh, "Effect of radial hydride on delayed hydride cracking behaviour of Zr-2.5Nb pressure tube material," *J. Nucl. Mater.*, vol. 542, p. 152457, 2020, doi: 10.1016/j.jnucmat.2020.152457.

[69]   J. D. Hong, M. Park, A. M. A. Holston, J. Stjärnsäter, and D. Kook, "Threshold stress intensity factor of delayed hydride cracking in irradiated and unirradiated zircaloy-4 cladding," *J. Nucl. Mater.*, vol. 543, p. 152596, 2021, doi: 10.1016/j.jnucmat.2020.152596.

[70]   E. Lacroix, P.-C. A. Simon, A. T. Motta, and J. D. Almer, "Zirconium Hydride Precipitation and Dissolution Kinetics in Zirconium Alloys," *Zircon. Nucl. Ind. 19th Int.*

Symp., pp. 67–91, 2021, doi: 10.1520/stp162220190035.

[71]   F. Passelaigue, P. C. A. Simon, and A. T. Motta, "Predicting the hydride rim by improving the solubility limits in the Hydride Nucleation-Growth-Dissolution (HNGD) model.," *J. Nucl. Mater.*, vol. 558, p. 153363, 2022, doi: 10.1016/j.jnucmat.2021.153363.

[72]   A. Grybenas, V. Makarevicius, and G. Dundulis, "Effect of test temperature and load ratio on hydride cracking rate of Zr-2.5Nb alloy," *Mechanika*, vol. 63, no. 1, pp. 21–26, 2007.

[73]   Y. Gou, Y. Li, Y. Liu, H. Chen, and S. Ying, "Evaluation of a delayed hydride cracking in Zr-2.5Nb CANDU and RBMK pressure tubes," *Mater. Des.*, vol. 30, no. 4, pp. 1231–1235, 2009, doi: 10.1016/j.matdes.2008.06.011.

[74]   S. Sunil, A. K. Bind, H. K. Khandelwal, R. N. Singh, and J. K. Chakravartty, "Delayed hydride cracking behavior of Zr-2.5Nb alloy pressure tubes for PHWR700," *J. Nucl. Mater.*, vol. 466, pp. 208–219, 2015, doi: 10.1016/j.jnucmat.2015.08.002.

[75]   P. K. Shah *et al.*, "Delayed hydride crack growth study on irradiated Zr-2.5Nb pressure tube," *J. Nucl. Mater.*, vol. 460, pp. 1–4, 2015, doi: 10.1016/j.jnucmat.2015.01.046.

[76]   S. Sunil, A. K. Bind, H. K. Khandelwal, R. N. Singh, and J. K. Chakravartty, "Effect of specimen thickness on DHC velocity for Zr-2.5Nb alloy pressure tube material," *J. Nucl. Mater.*, vol. 467, pp. 373–382, 2015, doi: 10.1016/j.jnucmat.2015.10.003.

[77]   S. Shimada, E. Etoh, H. Hayashi, and Y. Tukuta, "A metallographic and fractographic study of outside-in cracking caused by power ramp tests," *J. Nucl. Mater.*, vol. 327, no. 2–3, pp. 97–113, 2004, doi: 10.1016/j.jnucmat.2004.01.022.

[78]   S. Kim, "The texture dependence of KIH in Zr–2.5%Nb pressure tube materials," *J. Nucl. Mater.*, vol. 341, no. 1, pp. 83–85, 2006, doi: 10.1016/j.jnucmat.2005.09.027.

[79]   J. I. Mieza, E. De Las Heras, M. I. Arias, and G. Domizzi, "Effect of specimen pre-cracking method on delayed hydride cracking rate," *J. Nucl. Mater.*, vol. 420, no. 1–3, pp. 273–277, 2012, doi: 10.1016/j.jnucmat.2011.10.007.

[80]   ASTM E399-17, "Standard Test Method for Linear-Elastic Plane-Strain Fracture Toughness KIC of Metallic Materials," *Annu. B. ASTM Stand.*, pp. 1–33, 2011, doi: 10.6161/jgs.2013.71.02.

[81]   ASTM E1820, "Standard Test Method for Measurement of Fracture Toughness," *ASTM B. Stand.*, no. January, pp. 1–54, 2013, doi: 10.1520/E1820-13.Copyright.

[82]   ASTM 5045, "Standard Test Methods for Plane-Strain Fracture Toughness and Strain Energy Release Rate of Plastic Materials," *Annu. B. ASTM Stand.*, vol. 99, no. Reapproved, pp. 1–9, 1996, doi: 10.1520/D5045-99R07E01.2.

[83]   ASTM C1151-18, "Standard Test Method for Flexural Strength of Advanced Ceramics at Ambient," *Order A J. Theory Ordered Sets Its Appl.*, vol. 03, 2003, doi: 10.1520/C1161-18.1.

[84]   N. Perez, *Fracture Mechanics*, Second Edi. Springer, 2017.

[85]   G. R. Irwin, "Basic Aspects of Crack Growth and Fracture," *NRL Rep. 6598*, 1967.

[86]   G. R. Irwin and D. C. Washington, "G. R. Irwin, 'Analysis of stresses and strains near the end of a crack traversing a plate'. J. Applied Mechanics, 24,(1957) 361–364." pp. 361–364, 1957.

[87]   G. R. Irwin, "Crack-extension force for a part-through crack in a plate," *J. Appl. Mech. Trans. ASME*, vol. 29, no. 3, pp. 651–654, 1962, doi: 10.1115/1.3636591.

[88]   M. Dahlbäck *et al.*, "The effect of liner component iron content on cladding corrosion, hydriding, and PCI resistance," *ASTM Spec. Tech. Publ.*, no. 1467, pp. 873–895, 2005, doi: 10.1520/stp37539s.

[89]   L. I. Duarte, F. Fagnoni, R. Zubler, W. Gong, P. Trtik, and J. Bertsch, "Effect of the inner liner on the hydrogen distribution of zircaloy-2 nuclear fuel claddings," *J. Nucl. Mater.*, vol. 557, p. 153284, 2021, doi: 10.1016/j.jnucmat.2021.153284.

[90]   S. Jollet, R. Sobbia, and W. M., "TM-85-17-27: Numerical simulation of the SINQ target," 2017.

[91]   Y. Dai *et al.*, "Post-irradiation examinations of sinq target-11," *Mater. Sci. Forum*, vol. 1024 MSF, pp. 41–52, 2021, doi: 10.4028/www.scientific.net/MSF.1024.41.

[92]   Y. Dai, "The results of post-irradiation examinations of SINQ Taget-11," Villigen, 2017. [Online]. Available: TM-46-17-06.

[93]   J. Bertsch, "Characterization, Preparation and Metallography of Cladding Segments for PROMETRA Tests at CEA, Saclay," Villigen, 2009. doi: TM-43-07-27.

[94]   D. Aulet, Y. Dai, R. M. Bergmann, and M. Wohlmuther, "Radiation damage assessment of the sixth SINQ target irradiation program based on MCNPX simulation," *Nucl. Instruments Methods Phys. Res. Sect. A Accel. Spectrometers, Detect. Assoc. Equip.*, vol. 922, no. September 2018, pp. 310–321, 2019, doi: 10.1016/j.nima.2018.12.013.

[95]   G. Domizzi, L. Lanzani, P. Coronel, and P. Bruzzoni, "Supercharging of zircaloy-4," *J. Nucl. Mater.*, vol. 246, no. 2–3, pp. 247–251, 1997, doi: 10.1016/S0022-3115(97)00147-5.

[96]   J. J. Kearns, "Dissolution kinetics of hydride platelets in zircaloy-4," *J. Nucl. Mater.*, vol. 27, no. 1, pp. 64–72, 1968, doi: 10.1016/0022-3115(68)90008-1.

[97]   ASTM E647−13, "Standard Test Method for Measurement of Fatigue Crack Growth Rates," *Am. Soc. Test. Mater.*, vol. 03, no. July, pp. 1–50, 2014, doi: 10.1520/E0647-15E01.2.

[98]   R. JANSSEN, M., ZUIDEMA, J., WANHILL, *Fracture Mechanics*. 2004.

[99]   M. Grosse, J. Stuckert, M. Steinbrück, and A. Kaestner, "Secondary hydriding during LOCA - Results from the QUENCH-L0 test," *J. Nucl. Mater.*, vol. 420, no. 1–3, pp. 575–582, 2012, doi: 10.1016/j.jnucmat.2011.11.045.

[100] N. L. Buitrago *et al.*, "Determination of very low concentrations of hydrogen in zirconium alloys by neutron imaging," *J. Nucl. Mater.*, vol. 503, pp. 98–109, 2018, doi: 10.1016/j.jnucmat.2018.02.048.

[101] W. Gong, P. Trtik, S. Valance, and J. Bertsch, "Hydrogen diffusion under stress in Zircaloy: High-resolution neutron radiography and finite element modeling," *J. Nucl. Mater.*, vol. 508, pp. 459–464, 2018, doi: 10.1016/j.jnucmat.2018.05.079.

[102] C. J. Beevers and D. V. Edmonds, "On the room temperature fracture of zirconium/hydrogen alloys," *J. Nucl. Mater.*, vol. 33, no. 1, pp. 107–113, 1969, doi: 10.1016/0022-3115(69)90014-2.

[103] C. J. Beevers and K. G. Barraclough, "Some observations on the Deformation of Bulk Zirconium hydrides - Part 2 The Deformation of ε-hydrides," *J. Mater. Sci.*, vol. 4, no. 1, pp. 802–808, 1969, doi: https://doi.org/10.1007/BF00551076.

[104] A. Steuwer, J. R. Santisteban, M. Preuss, M. J. Peel, T. Buslaps, and M. Harada, "Evidence of stress-induced hydrogen ordering in zirconium hydrides," *Acta Mater.*, vol. 57, no. 1, pp. 145–152, 2009, doi: 10.1016/j.actamat.2008.08.061.

[105] M. Chollet *et al.*, "Synchrotron X-ray diffraction investigations on strains in the oxide layer of an irradiated Zircaloy fuel cladding," *J. Nucl. Mater.*, vol. 488, pp. 181–190, 2017, doi: 10.1016/j.jnucmat.2017.03.010.

[106] D. D. Le Pevelen, "X-ray crystallography of small molecules: Theory and workflow," *Encycl. Spectrosc. Spectrom.*, pp. 624–639, 2016, doi: 10.1016/B978-0-12-409547-2.05260-4.

[107] P. Debye, "Zerstreuung von Röntgenstrahlen," *Annale*, 1915, doi: https://doi.org/10.1002/andp.19153510606.

[108] J. A. Bearden, "X-ray Wavelength," *Rev. Mod. Phys.*, vol. 39, no. 1, pp. 78–124, 1967, doi: 10.1088/0031-9120/5/2/001.

[109] IAEA - International Atomic Energy Agency, "Evaluation of Conditions for Hydrogen Induced Degradation of Zirconium Alloys during Fuel Operation and Storage," *IAEA - TECDOC - 1781*, no. 1731, pp. 2016–2021, 2015, [Online]. Available: http://www-pub.iaea.org/MTCD/Publications/PDF/TE-1781_web.pdf%5Cnhttp://www-pub.iaea.org/books/IAEABooks/10980/Evaluation-of-Conditions-for-Hydrogen-Induced-Degradation-of-Zirconium-Alloys-during-Fuel-Operation-and-Storage.

[110] J. Desquines, D. A. Koss, A. T. Motta, B. Cazalis, and M. Petit, "The issue of stress state during mechanical tests to assess cladding performance during a reactivity-initiated accident (RIA)," *J. Nucl. Mater.*, vol. 412, no. 2, pp. 250–267, 2011, doi: 10.1016/j.jnucmat.2011.03.015.

[111] E. Kozsda-Barsy *et al.*, "Post-test examinations on Zr-1%Nb claddings after ballooning and burst, high-temperature oxidation and secondary hydriding," *J. Nucl. Mater.*, vol. 508, pp. 423–433, 2018, doi: 10.1016/j.jnucmat.2018.05.072.

[112] C. T. Sun and Z.-H. Jin, *Crack Tip Plasticity*. Elsevier Inc., 2012.

[113] G. R. Irwin, "Plastic Zone Near Crack Tip and Fracture Toughness," in *Sagamore Ordnance Material Conference*, 1960, pp. IV63-1V78.

[114] P. A. Raynaud, D. A. Koss, and A. T. Motta, "Crack growth in the through-thickness direction of hydrided thin-wall Zircaloy sheet," *J. Nucl. Mater.*, vol. 420, no. 1–3, pp. 69–82, 2012, doi: 10.1016/j.jnucmat.2011.09.005.

[115] H. H. Johnson, "Calibrating the Electric Potential Method for Studying Slow Crack Growth," 1965.

[116] F. H. Huang and W. J. Mills, "Delayed hydride cracking behavior for ZIRCALOY-2 tubing," *Metall. Trans. A*, vol. 22, no. 9, pp. 2049–2060, 1991, doi: 10.1007/BF02669872.

[117] J. S. Kim, J. D. Hong, Y. S. Yang, and D. H. Kook, "Rod internal pressure of spent nuclear fuel and its effects on cladding degradation during dry storage," *J. Nucl. Mater.*, vol. 492, pp. 253–259, 2017, doi: 10.1016/j.jnucmat.2017.05.047.

[118] E. Tenckhoff, "Deformation Mechanisms, Texture and Anisotropy in," *Zircon. Zircaloy*, vol. STP 966, 1988.

[119] EPRI, "Fracture Toughness Data for Zirconium Alloys: Application to Spent Fuel Cladding in Dry Storage," Palo Alto, California, 2001.

[120] ASTM D5054-14, "Standard Test Methods for Plane-Strain Fracture Toughness and Strain Energy Release Rate of Plastic Materials," *Annu. B. ASTM Stand.*, vol. 99, no. Reapproved, pp. 1–9, 1996, doi: 10.1520/D5045-99R07E01.2.

[121] A. F. Bower, *Applied Mechanics of Solids*. CRC Press, 2010.

[122] D. S. Dugdale, "Yielding of steel sheets containing slits," *J. Mech. Phys. Solids*, vol. 8, no. 2, pp. 100–104, May 1960, doi: 10.1016/0022-5096(60)90013-2.

[123] K. Une *et al.*, "The terminal solid solubility of hydrogen in irradiated Zircaloy-2 and microscopic modeling of hydride behavior," *J. Nucl. Mater.*, vol. 389, no. 1, pp. 127–136, 2009, doi: 10.1016/j.jnucmat.2009.01.017.

[124] A. W. Colldeweih, F. Fagnoni, P. Trtik, R. Zubler, M. A. Pouchon, and J. Bertsch, "Delayed hydride cracking in Zircaloy-2 with and without liner at various temperatures investigated by high-resolution neutron radiography," *J. Nucl. Mater.*, vol. 561, p. 153549, 2022, doi: 10.1016/j.jnucmat.2022.153549.

[125] Z. Xia, J. Zhang, Q. Tong, and S. Ding, "Multi-physics modeling of delayed hydride cracking in zirconium alloys," *J. Mech. Phys. Solids*, vol. 132, 2019, doi: 10.1016/j.jmps.2019.07.020.

[126] U. Stuhr, M. Grosse, and W. Wagner, "The TOF-strain scanner POLDI with multiple frame overlap-concept and performance," *Mater. Sci. Eng. A*, vol. 437, no. 1, pp. 134–138, 2006, doi: 10.1016/j.msea.2006.04.069.

[127] P. Trtik and E. H. Lehmann, "Progress in High-resolution Neutron Imaging at the Paul Scherrer Institut-The Neutron Microscope Project," *J. Phys. Conf. Ser.*, vol. 746, no. 1,

pp. 0–6, 2016, doi: 10.1088/1742-6596/746/1/012004.

[128] J. Crha, J. Vila-Comamala, E. Lehmann, C. David, and P. Trtik, "Light Yield Enhancement of 157-Gadolinium Oxysulfide Scintillator Screens for the High-Resolution Neutron Imaging," *MethodsX*, vol. 6, pp. 107–114, 2019, doi: 10.1016/j.mex.2018.12.005.

[129] P. Trtik and E. H. Lehmann, "Isotopically-enriched gadolinium-157 oxysulfide scintillator screens for the high-resolution neutron imaging," *Nucl. Instruments Methods Phys. Res. Sect. A Accel. Spectrometers, Detect. Assoc. Equip.*, vol. 788, pp. 67–70, 2015, doi: 10.1016/j.nima.2015.03.076.

[130] P. Boillat *et al.*, "Chasing quantitative biases in neutron imaging with scintillator-camera detectors: a practical method with black body grids," *Opt. Express*, vol. 26, no. 12, p. 15769, 2018, doi: 10.1364/oe.26.015769.

[131] C. Carminati *et al.*, "Implementation and assessment of the black body bias correction in quantitative neutron imaging," *PLoS One*, vol. 14, no. 1, pp. 1–12, 2019, doi: 10.1371/journal.pone.0210300.

[132] O. Yetik, L. I. Duarte, F. Fagnoni, A. Colldeweih, R. Zubler, and J. Bertsch, "Influence of scattering correction on quantitative hydrogen analysis of fuel claddings using high resolution neutron radiography," *TopFuel*, pp. 1–10, 2021.

[133] P. Trtik, R. Zubler, W. Gong, R. Grabherr, J. Bertsch, and L. I. Duarte, "Sample container for high-resolution neutron imaging of spent nuclear fuel cladding sections," *Rev. Sci. Instrum.*, vol. 91, no. 5, 2020, doi: 10.1063/1.5143226.

[134] C. Carminati, M. Strobl, and A. Kaestner, "KipTool, a general purpose processing tool for neutron imaging data," *SoftwareX*, vol. 10, p. 100279, 2019, doi: 10.1016/j.softx.2019.100279.

[135] M. Strobl, N. Kardjilov, A. Hilger, G. Kühne, G. Frei, and I. Manke, "High-resolution investigations of edge effects in neutron imaging," *Nucl. Instruments Methods Phys. Res. Sect. A Accel. Spectrometers, Detect. Assoc. Equip.*, vol. 604, no. 3, pp. 640–645, 2009, doi: 10.1016/j.nima.2009.03.020.

[136] N. Kardjilov, I. Manke, A. Hilger, M. Strobl, and J. Banhart, "Neutron imaging in materials science," *Mater. Today*, vol. 14, no. 6, pp. 248–256, 2011, doi: 10.1016/S1369-7021(11)70139-0.

[137] N. Banterle, K. H. Bui, E. A. Lemke, and M. Beck, "Fourier ring correlation as a resolution criterion for super-resolution microscopy," *J. Struct. Biol.*, vol. 183, no. 3, pp. 363–367, 2013, doi: 10.1016/j.jsb.2013.05.004.

[138] A. W. Colldeweih, A. Baris, P. Spätig, and S. Abolhassani, "Evaluation of mechanical properties of irradiated zirconium alloys in the vicinity of the metal-oxide interface," *Mater. Sci. Eng. A*, vol. 742, no. September 2018, pp. 842–850, 2019, doi: 10.1016/j.msea.2018.09.107.

[139] C. Proff, S. Abolhassani, M. M. Dadras, and C. Lemaignan, "In situ oxidation of

zirconium binary alloys by environmental SEM and analysis by AFM, FIB, and TEM," *J. Nucl. Mater.*, vol. 404, no. 2, pp. 97–108, 2010, doi: 10.1016/j.jnucmat.2010.05.012.

[140] O. T. Woo and G. J. C. Carpenter, "Identification of zirconium hydrides by electron energy loss spectroscopy," *Scr. Metall.*, vol. 20, no. 3, pp. 423–426, 1986, doi: 10.1016/0036-9748(86)90172-9.

[141] M. P. Puls, S. Q. Shi, and J. Rabier, "Experimental studies of mechanical properties of solid zirconium hydrides," *J. Nucl. Mater.*, vol. 336, no. 1, pp. 73–80, 2005, doi: 10.1016/j.jnucmat.2004.08.016.

[142] A. Forster, "EIGER detectors in biological crystallography," vol. 1, no. May, pp. 5–10, 2016.

[143] I. Johnson *et al.*, "Eiger: A single-photon counting x-ray detector," *J. Instrum.*, vol. 9, no. 5, 2014, doi: 10.1088/1748-0221/9/05/C05032.

[144] J. Kieffer and D. Karkoulis, "PyFAI, a versatile library for azimuthal regrouping," *J. Phys. Conf. Ser.*, vol. 425, no. PART 20, 2013, doi: 10.1088/1742-6596/425/20/202012.

Curriculum Vitae

Aaron Colldeweih

Address	**Contact Information**
Müllermattstrasse 9A	+41 076 248 30 80
Brugg, AG 5200	e-mail:aaron.colldeweih@psi.ch
Switzerland	

Education and Certificates

08/2018- Present	**École Polytechnique Fédérale de Lausanne (EPFL)** Lausanne, CH PhD: Physics, Expected Completion: 06/2022
09/2015- 08/2017	**Eidgenössiche Technische Hochschule Zürich (ETHZ)** Zürich, CH Master of Science: Nuclear Engineering
04/2013	**EIT Certified,** California, USA California State Fundamentals of Engineering Exam (EIT)
01/2009- 03/2013	**University of California, Davis (UCD)** Davis, USA Bachelor of Science: Mechanical Engineering

---

Work and Research Experience

08/2018- 06/2022	**Paul Scherrer Institut (PSI),** Villigen, CH Doctoral Student - Laboratory for Nuclear Materials (LNM)

Thesis Title: Characterization of Delayed Hydride Cracking in Irradiated and Unirradiated Zircaloy-2 Cladding
- Mechanical testing on irradiated and unirradiated nuclear fuel cladding material
- Extensive hands-on experience with remote operation in a Hot Lab

- Neutron radiography and synchrotron-XRD phase mapping of DHC hydrides
- Design and construction of notching device for irradiated cladding material
- Supervised intern students on XRD phase map processing

03/2018- **Nagra,** Wettingen, CH

07/2018 Nuclear Engineer – Inventory Logistics (IL)

- Dose rate calculations for various radioactive waste packages with MCNP and MicroShield
- Activated concrete volume calculations of Swiss reactors

11/2017- **Paul Scherrer Institut (PSI),** Villigen, CH

12/2017 Research Assistant – Laboratory for Nuclear Materials (LNM)

- Wrote and submitted an article based on the results of the master project: "*Investigation of the mechanical properties of Zircaloy-2*", to Material Science and Engineering A
- Fabricated micropillars and performed nano-indentation experiments to estimate the material properties on irradiated Zircaloy-2 material

09/2015- **Paul Scherrer Institut (PSI),** Villigen, CH

08/2017 Masters Student - Laboratory for Nuclear Materials (LNM)

Thesis Topic: Micropillar fabrication and nano-indentation on irradiated Zircaloy-2 cladding

- Optimized micropillar fabrication by FIB and performed nano-indentation experiments
- Estimated material properties at the M/O interface of Zircaloy-2 based on compression test data
- Produced FEM models of micro-compression tests with implemented material properties obtained from experiments for validation

07/2016- **Axpo Power AG**, Kernkraftwerk Beznau(KKB), Döttingen, CH

10/2016 Intern – KBR-A, Reactor and Safety

- Verified new RELAP5 input with previous safety analyses
- Produced reports for RELAP5 results and verifications

09/2014- **Paul Scherrer Institut (PSI),** Villigen, CH

05/2015 Research Assistant – Laboratory for Thermal-Hydraulics (LTH)

- Post-processed and analyzed data from two-phase flow wire mesh sensor experiments
- Optimized MATLAB image analysis and produced 3D images of bubbles from wire mesh sensor data

04/2014- **DMG Mori Seiki,** Davis, USA

07/2014   Machinist Intern – Machining Factory

- Operated and maintained DMG Mori Seiki CNC Machines
- Quality Control on the production of machined parts

01/2014- **Davis High School FIRST Robotics Club**, Davis, USA

04/2014   Mentor – Davis High School

- Led students in robot design and construction

Publications

Colldeweih, A. W., Bertsch, J., "Effect of Temperature and Hydrogen Concentration on the Threshold Stress Intensity Factor of Radial Delayed Hydride Cracking in Fuel Cladding." J. Nucl. Mater. 565, (2022) 153737, doi: 10.1016/j.jnucmat.2022.153737

Colldeweih, A. W., Fagnoni, F., Yetik, O., Trtik, P., Zubler, R., Pouchon, M. A., Anghel, C., Dai, Y., Duarte, L. I., Bertsch, J., "Radial Delayed Hydride Cracking in Irradiated Zircaloy-2 Cladding: Advanced Characterization Techniques," Zirconium in the Nuclear Industry: 20th International Symposium (STP: Accepted).

Colldeweih, A. W., Fagnoni, F., Trtik, P., Zubler, R., Pouchon, M. A., Bertsch, J., "Delayed hydride cracking in Zircaloy-2 with and without liner at various temperatures investigated by high-resolution neutron radiography." J. Nucl. Mater. 561, (2022) 153549, doi: 10.1016/j.jnucmat.2022.153549

Colldeweih, A. W., Fagnoni, F., Trtik, P., Zubler, R., Pouchon, M. A., Bertsch, J., "Effect of the Inner Liner on Radial Delayed Hydride Cracking," Proceedings to the Top Fuel Conference in Santander, 2021

Abolhassani, S., Baris, A., Vanta, R., Hawes, J., Grabherr, R., **Colldeweih, A. W.**, Restani, R., Hermann, A., Bertsch, J., Chollet, M., Kuri, G., Martin, M., Portier, S., Wiese, H., Schweikert, H., Bart, G., Ammon, K., Ledergerber, G., "Towards an Improved Understanding

of the Mechanisms Involved in the Increased Hydrogen Uptake and Corrosion at High Burnups in Zirconium-based Claddings," Zirconium in the Nuclear Industry: 19th International Symposium (2021). doi:10.1520/stp162220190052.

Gong, W., Trtik, P., **Colldeweih, A. W.**, Duarte, L. I., Grosse, M., Lehmann, E., Bertsch, J., "Hydrogen diffusion and precipitation in duplex zirconium nuclear fuel cladding quantified by high-resolution neutron imaging," J. Nucl. Mater. vol. 526, (2019) 151757, doi: 10.1016/j.jnucmat.2019.151757

Colldeweih, A. W., Trtik, P., Zubler, R., Gong, W., Bertsch, J., "Influence of Cracking Direction on Fracture Mechanics During DHC of Zircaloy-2 Cladding," Proceedings to the Top Fuel Conference in Seattle, 2019

Colldeweih, A. W., Baris, A., Spätig, P., Abolhassani, S., "Evaluation of Mechanical Properties of Irradiated Zirconium Alloys in the Vicinity of the Metal-Oxide Interface." Materials Science and Engineering: A, vol. 742, (2018) pp. 842-850, doi: 10.1016/j.msea.2018.09.107

Conference Presentations

Colldeweih, A. W., Makowska, M., Trtik, P., Bertsch, J., "Radial Delayed Hydride Cracking in Liner Cladding: Advanced Characterization Techniques," MiNES in Pittsburgh, 2021

Colldeweih, A. W., Fagnoni, F., Trtik, P., Zubler, R., Pouchon, M. A., Bertsch, J., "Effect of the Inner Liner on Radial Delayed Hydride Cracking," Top Fuel in Santander, 2021

Colldeweih, A. W., Trtik, P., Bertsch, J., "Radial delayed hydride cracking in hydrogen rich Zircaloy-2 cladding" NuMat in Ghent (Virtual), 2020

Colldeweih, A. W., Trtik, P., Zubler, R., Gong, W., Bertsch, J., "Influence of Cracking Direction on Fracture Mechanics During DHC of Zircaloy-2 Cladding," Top Fuel in Seattle, 2019

Skills

- Computer: ANSYS Workbench, RELAP5, MCNP, Matlab, C++, Visual Basic
- Machine: SEM/FIB, Neutron Radiography, Synchrotron XRD, Nano-Indenter, Lathe, End Mill, Welding

- Language: English (Mother Tongue), German (Professional Proficiency), Swiss-German (Fluent)

Hobbies

Cycling, Skiing, Hiking, Fishing, Baking, Gardening